UNIVERSITÀ DEGLI STUDI DI PADOVA

Dipartimento di Fisica e Astronomia "Galileo Galilei"

Master Degree in AstroPhysics and Cosmology

Final Dissertation

Thermal Emission from short GRB jets breaking out of binary neutron star merger environments:

Relativistic hydrodynamic simulations with M1 radiation transport

Thesis supervisor

Prof. Roberto Turolla

Thesis co-supervisor

Dr. Riccardo Ciolfi

Candidate

Tomasina Edoardo

Academic Year 2021/2022

Abstract

In August 2017, the combined detection of the gravitational wave signal GW170817 and its electromagnetic (EM) counterparts, including in particular the high-energy burst GRB 170817A, confirmed the canonical scenario according to which short-hard gamma-ray bursts (SGRBs) are produced as a consequence of the merger of two neutron stars in a binary system.

This also proved that the remnant object formed in a binary neutron star (BNS) merger is able to launch a powerful relativistic jet, which is a necessary ingredient to produce a SGRB. Moreover, this event was observed from a viewing angle between about 15 and 30 degrees away from the main jet propagation (or remnant spin) axis, resulting in the very first observation of a SGRB signal along a direction outside the narrow cone of the jet core. At such viewing angles, the so-called prompt SGRB emission is likely dominated by the flash of radiation that accompanies the shock breakout induced by the incipient jet piercing through the surrounding BNS merger material. A proper modelling of shock breakout signals in such context, which is still missing, represents then a key ingredient for the interpretation of the August 2017 event.

This Thesis presents a theoretical study of SGRB jets breaking out of the environment surrounding a BNS merger and the corresponding burst of radiation as observed at generic viewing angles. The work, based on the open-source numerical code PLUTO, combines for the first time special relativistic hydrodynamic simulations of SGRB jets emerging from a realistic BNS merger environment with a recently developed two-moment scheme for treating photon radiation transport. The scope of the Thesis is to demonstrate the approach and provide a first set of results based on a fiducial SGRB jet model. The emerging shock-breakout signals obtained here implicitly assume that radiation is essentially thermal, which represents a very first step towards a more detailed investigation where non-thermal radiation processes are also consistently included.

Acknowledgements

This Thesis is the result of almost an year of efforts and dedication, therefore many people should be thanked. Dr. Riccardo Ciolfi, to begin with, is the main architect behind the Thesis work. I've really enjoyed working with him as he is incredibly available and helpful. I feel like I owe a lot to him who has treated me like part of its group from the very beginning and has never stopped to look after and help me in the times of need, always displaying a tremendous amount of patience and appreciation. Along with Dr. Ciolfi I'd like to thanks the members of its group, J.V.Kalinani and especially A.Pavan that, without hesitations, dedicated lots of their time to help me during the whole work. Furthermore I'd like to thanks all the researchers and professors that were always very available and friendly in supporting me both with bureaucratic tasks or with the Thesis drafting.

The latter were quite rough years which have challenged the majority of the people. During this peculiar period many of them have left but also many others have gotten closer. I'd like to thanks all my friends that have sticked together with me and that helped me in overcoming the harshest moments, without your presence I could hardly imagine how I would be able to complete this journey any time soon.

I'm tremendously grateful to all my family and especially to the little kernel formed by my parents and my (not-so-little-anymore) brother. Their support was never lacking but instead it's guiding and inspiring me from a very long time. I really hope to be able to repay your love back, one day, by seeing you very proud of me.

Finally I want to dedicate a brief, special thanks to the one person who was always there for me during this year. As I am completely aware that life is a journey and there is no scientific effort really able to predict where we are going to be tomorrow, I'll always remember the time we are spending together. Thank you for all your support and love Nebbia.

Contents

List of Figures

List of Tables

Chapter 1

Introduction: binary neutron star mergers

Neutron stars (NSs) represent, on average, about 0.1% of the stars in a galaxy. They are among the densest objects we know in the Universe, concentrating a mass in the range $[1.3M_\odot - 2.5M_\odot]$ inside a radius of only $\sim$10 km. Even if NS are surpassed in compactness by the denser black holes (BHs), they are the most extreme compact objects we can directly observe through electromagnetic (EM) signals. The very first discovered binary neutron star (BNS) was PSR B1913+16. It was found in 1975 by Hulse and Taylor as a system composed by a radio pulsar in a decaying orbit around another NS. This discovery led to the first, indirect, evidence of the existence of a gravitational radiation, previously predicted by Einstein in his theory of General Relativity. Hulse and Taylor won a Nobel prize in 1993 thanks to the measurement of the system' shrinking separation.

Nowadays, in the rise of the Multi-Messanger era, BNS have grown a tremendous importance in many astrophysical contexts. The main constraints on BNS properties come from pulsar's radio signals observations, however other peculiar EM signals observed at cosmic distances were attributed to BNS systems. This is the case of the short-hard gamma-ray burst (SGRB) and the kilonova transients. Even though, for a long time, there were no direct proof of such correlation, intensive studies in both theoretical and observational fields were made in favour of this connection. Furthermore, neutrino cooling is known to be one of the main sources of energy loss of the massive NS formed as result of a BNS merger (as for newly born NSs in general). Therefore, a strong neutrino emission from BNS mergers is expected, even though neutrino detection still presents many technological difficulties. An actual turn-over on the observational investigation of BNS has been the beginning of gravitational wave (GW) detections via the first two GW interferometers: LIGO and VIRGO. The new astronomic channel of GWs, allows for the tightening of the constraints on the BNS properties and, above all, for the direct proof of the connection between BNS mergers, SGRB emission and kilonova transient, providing insights on the production of heavy elements.

This Chapter is going to review the formation and evolution of BNS systems up to the merging and beyond. Section 1.1 will start by studying the characteristics of the progenitors and the different formation channels, focusing on those which may lead to a merger. Section 1.2 will discuss the merger stages and the resulting compact remnant. Finally, highlighting the diversity of the outcomes with respect to the different channels of evolution, Section 1.3 will present some of the magnetic properties of the remnants, while Section 1.4 will discuss the possible emission of more or less collimated outflows and their connection with kilonova transients.

1.1 BNS system formation

Binary stars are pairs of stars which are mutually affected by the gravitational pull of the companion and orbit around a common center of mass with variable initial separation. The binary system components may have different composition and undergo different stages of evolution. In particular, when a massive star (in the mass range 8–50 $M_{\odot}$) reaches the end of its evolution, it explodes as a Core-Collapse Supernova (CCSN) usually leaving a compact object as a remnant: if the exploding star has a mass in the lower part of the range then it will likely become a NS, while more massive progenitors will directly collapse into a BH [1]. Once both the components have undergone a CCSN explosion, if the energy of the explosions did not disrupt the system, the remaining pair is what we refer to as a binary compact object (CO). The intensity of the resulting kicks decides the fate of the system. As NS binaries are lighter than BHs it's easier for them to be disrupted, however if the system undergoes some binary process (like a common envelope event) which is able to shrink the stars orbits and to remove the stellar envelope, then the consequent SN kick will be lower allowing for the production of a BNS system [2].

Mass transfer events may occur before or after the trigger of CCSNe, in the latter case, if only one star (the primary) is exploded as a SN producing a compact object, then it can start accreting matter from the secondary. This process is however usually limited by the Eddington mass accretion limit. Depending on a variety of factors, such as the lightness of the companion, the tidal interactions and the possible occurrence of wind mass loss phenomena, the binary CO formed could either be a BH-BH (BBH) system or a BH-NS (BHNS) system [3, 4].

Formation of CO binary systems takes place in two very different environments, either in a Galactic, stellar field, following from the evolution of an isolated binary of massive stars, or in the denser region of a globular cluster, where they usually form at high rates thanks to the frequent dynamical interactions [5]. The different properties of these regions end up strongly influencing the nature of the COs and their evolution and, as we will see in later chapters, also some of the properties of the SGRBs produced.

1.1.1 Dynamical evolution

The central regions of a stellar cluster, globular ones in particular, are characterized by a very high density. In this environment many bodies interaction and even close encounters are very frequent, making it a very dynamically active place. Here any kind of binary CO may be produced, however usually its components may be produced at individual times and then be exchanged in the binary through some dynamical process. Moreover, in clusters binaries may interact between each other as well: the higher the mass, the higher the probability a system will undergo some interactions. The vast majority of these involve low mass main sequence stars (since they are without any doubt the dominating species in a stellar cluster), being exchanged between binaries. At some point, due to its strongest gravitational attraction, a BH may be exchanged in a binary system, then, through some other encounters, such system may evolve into a BH-BH binary. This represent the final stage of a dynamic binary, since any other interactions with the double BH system, i.e. fly-by events, will only end up strengthening the system by tightening its orbit [6].

The production of binaries BHs seems to be favoured. NS-NS systems, in fact, turn out to be inhibited by various factors. First of all, they are a lighter configurations with respect to binary BHs, hence less involved in dynamical interactions and more prone to be exchanged out of the binary. Moreover, at their birth NS could receive a large natal kick which could end up in either disrupting the binary or ejecting it out of the cluster. All considered, population syntheses simulations suggest that globular clusters contribute only up to 20% of the cosmic BNS merger rate [6].

1.1.2 Isolated evolution

In the vastly wider galactic stellar fields, the star densities are so low that dynamical interactions can be safely neglected. In this environment binary systems of massive stars can evolve unaffected by external agents, in an isolated fashion, ending up forming a couple of compact objects together. BH-BH systems are easier to originate as they can be formed without any binary interaction (or just trough stable mass transfer episodes), whereas BNS requires instead some process which shrinks their orbit in order to survive the SN explosion. As a result, BNS systems will have in general a tighter orbit with respect to other compact binaries, this will more likely lead to a merger event.

The aim of this work is the study of short GRB associated to BNS mergers, hence from now on we are going to focus only on these systems, evolved in isolation inside a stellar population field.

1.1.3 Formation channels

Systems of BNS which are going to merge within a Hubble time are all produced in a similar way, typically inside a stellar field population. However, two stars in a binary may interact in a variety of ways and this involves a very large parameter space. In order to predict the fate of a binary system, population syntheses codes are employed. Their outcome is usually dependent on the input physics provided. This led to the production of many different models which, given a slight difference on the initial conditions, may lead to quite different formation channels. Even if this problem have been tackled for many years now, most constraints are still wide and uncertain. Among them there are: the mass transfer processes, in particular the CE phase efficiency; the maximum mass allowed for a NS before collapsing into a BH; many of the details of SN explosions, which are still quite uncertain and strongly related to the chosen equation of state (EoS); the stellar winds efficiency and their relation with the metallicity; the supernova kick which could unbound the system [7, 8, 9].

Mass Transfer:

The evolution of a binary is driven by the mass transfer processes. At any stage one of the two stars may fill out its Roche lobe, overcoming the inner Lagrangian point of the system and triggering a Roche Lobe Overflow (RLO) mechanism which induces a mass transfer toward the other star.

In general the mass transfer can be in the form of:

- Non-conservative, stable mass transfer: Part of the donor star's material is accreted by its companion while the rest is lost away from the system. As the donor loses mass its radius starts shrinking so that the transfer stops when both the stellar radii are smaller again than the Roche lobe. This phase may happen if either at least one of the star in the binary is a MS transferring to a companion in any other evolutionary stage, or a giant transferring to a non giant. Also it has to be fulfilled the *stability criterion for the mass transfer* [5]:

$$M_{don} \leq cM_{acc} \tag{1.1}$$

  where c is a numerical constant which depends on the evolutionary stage of the donor [10]. We can compute the orbital separation change, after an mass transfer episode as [5]:

$$\frac{a_{final}}{a_{initial}} = \frac{M_1^f + M_1^f}{M_1^i + M_2^i} \left(\frac{M_{don}^f}{M_{don}^i}\right)^{c_1} \left(\frac{M_2^f}{M_2^i}\right)^{c_2} \tag{1.2}$$

Where subscripts 1 and 2 indicate donor and companion respectively, a is the orbital separation and c_1 and c_2 are constants which depend on the amount of lost mass. The general behaviour is the following, at the beginning of the mass transfer the orbit decreases until the accretor gains enough mass to become the most massive component. At this point the trend is reversed and the semimajor axis increases. During a stable mass transfer a giant could eventually loose all its envelope, in this case its core is exposed and it becomes a naked He-star. Usually these stars suffer from a strong wind-driven mass loss [11, 12].

- Standard Common Envelope: If the criterion (1.1) is not satisfied after a mass transfer process has been triggered, then this will become dynamically unstable: during the overflow the orbital separation shrinks, so if the donor star isn't able to keep up fast enough than the mass transfer continues, even accelerates, causing the orbit to shrinks even further in a run-away fashion. In this scenario the accretor may be not able to acquire all the material coming from the donor, this would cause the latter's envelope to be lifted up, engulfing the entire system. The orbital motion of the stars inside the common envelope will eventually suffer from the effect of the drag force exerted by the gas, this will draw orbital energy from the system and causing a spiral-in. The new orbital separation can then be computed by comparing the initial binding energy of the envelope [4]:

$$E_{bind} = -\frac{G}{\lambda}\left(\frac{M_1 M_{env}}{r_1} + \frac{M_2 M_{env}}{r_2}\right) \tag{1.3}$$

and the orbital energy of the cores

$$E_{orb} = \frac{1}{2}\frac{G, M_{c,1} M_{c,2}}{a} \tag{1.4}$$

with the orbital energy needed to unbind the envelope:

$$E_{bind} = \Delta E_{orb} = \alpha(E_{orb,final} - E_{orb,initial}) \tag{1.5}$$

Where G is the gravitational constant, a is the orbital separation, and λ and α are a geometrical factor (describing the central concentration of the giant) and the drag's removal energy efficiency, respectively. In general both λ and α are taken as free parameters [13, 14]. If the resulting orbital separation is smaller than the sum of the core radii: $a \leq (r_{c,1} + r_{c,2})$, the stars have spiraled-in too close and merged. Instead, if the orbital separation is still greater than the core sizes, than the drag absorption of energy from the gas end up increasing its temperature causing it to expand and eventually leave the system. As a result, the naked donor and the companion, after the CE phase, orbit in a closer and strengthen orbit. Let's notice that if the companion is a MS or a WD, then the the common envelope will be lifted by the giant companion only ('single' CE) and the amount of matter accreted in the CE phase is negligible.

- CE with hypercritical accretion: During the spiral-in phase in a CE event, if the companion is a compact object such as a NS, it can accrete some of the donor's material. In the usually used spherical or Bondi-Hoyle approximations the rate of matter accretion is countered by the radiation pressure generated which sets up the Eddington limit as cap for the accretion rate. However during the spiral-in the NS falls into a very dense environment and it has been showed [15] that if the mass accretion rate reaches $\dot{M} > 10^4 M_{edd}$ than a hypercritical accretion event is triggered on and the photons are carried in as well, following the adiabatic inflow [16]. In a typical NS-red giant binary evolution $\dot{M}$ reaches $\approx 10^8 M_{edd}$ enough to ignite an hypercritical accretion during which about 0.2 $M_\odot$ is gained by the compact object [17]. This may have a deep impact on the probability of different BNS formation channels, indeed if a NS is allowed to accrete too much material it will collapse into a BH generating a different kind of BCO.

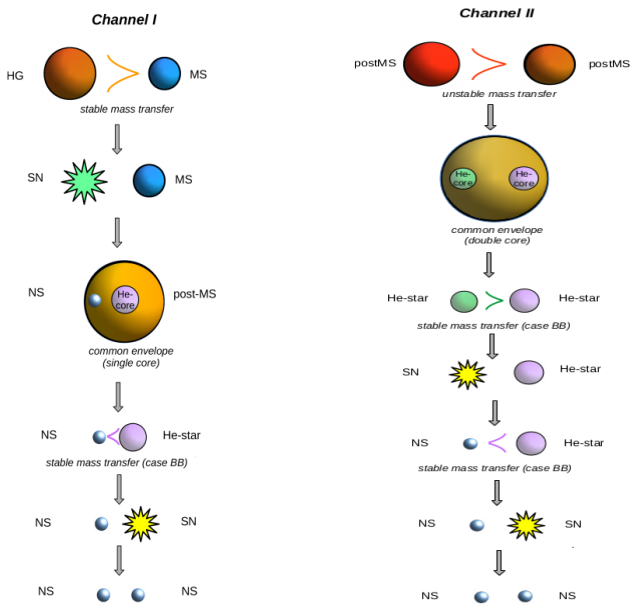

(a) Standard model (b) Alternative model

Figure 1.1: *Left*: widely accepted standard path formation of BNS systems (from top to bottom). *Right*: example of an alternative formation channel (see text). Figure adapted from [18].

Formation paths:

Having fixed all the input ingredients such as the initial masses distribution, winds prescriptions and the hydrodinamical models for SN collapse and mass transfer event, one can predict the evolutionary outcome of an isolated population of progenitors. There still isn't a general agreement on the the results of a binary interaction as it strongly depends on the model adopted and on the physical description of the initial conditions like the natal kick distribution, the initial star masses (known as ZAMS, 'Zero-Age Main Sequence'), the metallicity, the mass transfer and so on. Hence many 'standard models' have been proposed to describe the possible BNS formation paths [2, 7, 18, 19, 20, 21].

In order to obtain a binary Neutron star the initial system should be rather high massive,the mass range of the progenitors is still quite debated. According to literature a reasonable range of masses could lie within 8-30 $M_{\odot}$, with a lower limit for the ZAMS stars placed at 6 $M_{\odot}$ [9]. This ensures the trigger of a CCSN event, whereas less massive system would end up producing NS-WD pairs.

Figure 1.1 summarizes a couple of the generally accepted standard BNS formation paths. In order for them to occur, the initial mass distribution of the system must present some degree of asymmetry, with one MS star being more massive than the other (hence a small mass ratio $\frac{M_2}{M_1}$ with M_1 being the donor). The initial asymmetric mass distribution ensures that the most massive star evolves faster than the companion entering the giant phase at early times (this takes the hydrogen's nuclear timescale to happen $\approx 10^7 years$). As the primary evolves, its radius inflates and eventually overcome the Roche radius starting a stable, non-conservative mass transfer event. Usually this happens at the time between the hydrogen exhaustion and the ignition of the helium in the core, in literature it's known as 'Case B' mass transfer [20] and it seems to be the more common case in the context of BNS formation. Once the mass transfer stops the companion has accreted some of the hydrogen-rich material of the primary's envelope while the rest has been ejected away; at this point the initial giant is usually left with its naked helium core entirely exposed (especially for high metallicities) even if, in some low Z cases, a

considerable amount of hydrogen envelope can still be preserved, favouring the trigger of new mass transfer events.

After the SN event, the system receives a large kick which imparts a velocity to the center of mass (in average of order ≈ 100 km/s) and which induces a large orbital eccentricity. If the binaries has not been disrupted by the kick, it will take about $\approx 10^8$ years to circularize again its orbit trough tidal effects [21].

This time allows the lighter companion to evolve further and engage a mass transfer event with the primary NS. Usually at this point the mass ratio is so small that the overflow is dynamically unstable and a CE is formed, the spiraling-in of the NS will in the end deposit enough energy to lift away the envelope leaving a NS-HE star system.

Further evolution of the He star (especially if it's in a convective regime) will trigger another case B (which is referred to as case BB) mass transfer event which will deposit some mass in the old NS, which is then recycled as a pulsar, and eventually will end up with the core-collapse of the companion. Finally, if the original NS survives the mass accretion and the second kick does not disrupt the binary again, a pair of tightly bounded, mass-asymmetric NSs is generated.

While the standard formation channel is generally accepted and can explain the observation of most of the millisecond pulsars [20], it suffers from being quite old and neglect many results lately obtained trough more modern population syntheses and hydrodinamical calculations, especially for what concerns the accretion rates during mass transfer [15, 16]. For example, in the CE phase of the standard channel, the possibility of an hypercritical accretion for the primary NS is not considered, this led to the underestimate of the NS's final mass, thus the underestimate of the BH-NS formation rate.

Up to date tenth of slightly different formation channels have been proposed/discovered, in particular the inclusion of the hypercritical accretion rate has led to an update on the final masses of NS in the binaries and on their separation, in general finding more tight systems with shorter merger times with respect to past predictions [5].

There were also proposed alternative scenarios (for example [22]), in Figure 1.1b it's shown a formation paths involving two initial star with similar masses (within 5% of difference) [16, 21]. In this scenario the stars exit MS before each of the two has the time to undergo SN, hence the mass transfer process triggers a double CE event (DCE) in which the two HE-cores orbit around each other inside the vast gaseous combination of the hydrogen envelopes. Once the latter is ejected the cores will eventually explode as SN even if, in general, not simultaneously. Then if the kicks don't disrupt the system, a BNS is generated. In this case, depending on whether an accretion processes have taken place, one or both NS may be observed as pulsars. However the scenario in which neither of them has been recycled is also possible, in this case the system is considered 'silent' and it is only briefly detectable in the radio band (even if it could still lead to GRBs emission) [5].

1.2 Stages of a BNS merger

Once a BNS is formed, if no exotic event happens, its evolution is entirely dependent on gravitational effects. While the NSs orbit each other, their masses are so large that they are able to produce and radiate non-negligible gravitational GWs. GWs are perturbations of the space-time, generated by a time-varying quadrupolar mass distribution and they propagate at the speed of light. The existence of GWs was first proposed in Einstein's General Relativity (GR) as perturbed solutions of Einstein field equations in the weak limit approximation [23, 24].

Tight binaries get closer and closer as they loose energy through gravitational emission, and in the end they will be close enough to plunge and merge into a compact remnant. This process is divided in three different phases: Inspiral, Merger, Ringdown. Each phase evolves with very different timescales and is associated to a different waveform type as seen in Fig 1.2. Due to

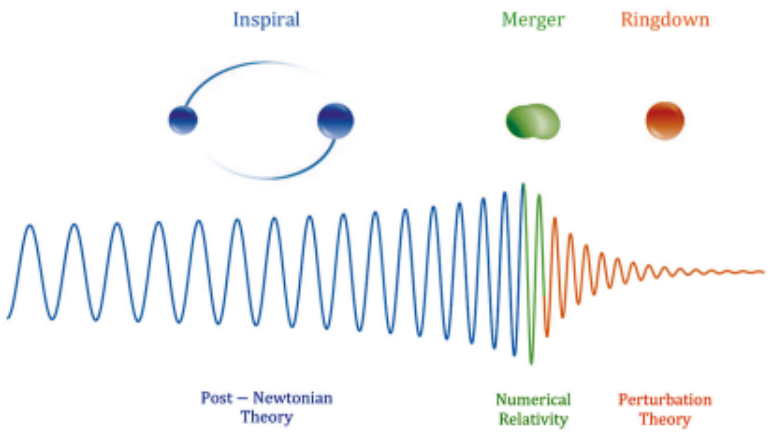

Figure 1.2: Cartoon representing the coalescence of a CO, each phase is associated with a different gravitational waveform. Images taken from [23].

the quite extreme physical processes in the game, the treatment should always involve GR at some level: while the inspiral and the ringdown phases may be described analytically within Post-Newtonian or Perturbative approximations of the Einstein equations, the merger phase is instead a too complex, highly non-linear system which requires expensive numerical computations [7].

1.2.1 Inspiral

In order to actually merge within a Hubble time, a binary should be born with initial separation $\leq 5R_{\odot}$ [3]. Initially the orbital evolution is slow and GW frequency is quite small. As the energy is emitted the neutron stars get closer and closer, as a consequence the frequency of the signal increases releasing more and more energy which in turn speeds up the inspiraling process in a runaway fashion. The emitted GW waveform is a sinusoidal which increases in frequency and amplitude called *chirp signal*.

The inspiral phase can be treated in the 2.5 Post-Newtonian approximation [7] assuming the NSs as point masses. In the approximation of a circular orbit we can estimate an orbital decay rate timescale

$$\tau_{GW} = \frac{5}{64}\frac{a^4}{q(1+q)M_1^3} = 2.2\times 10^{-8} q^{-1}(1+q)^{-1}\left(\frac{a}{R_{\odot}}\right)^4\left(\frac{M_1}{1.4M_{\odot}}\right)^3 yr \tag{1.6}$$

where natural units are used (G=c=1), a is the orbital separation, M_1 is the mass of the primary (more massive) NS and $q = \frac{M_2}{M_1}$ is the mass ratio. The computation for an elliptical orbit is a little more complicated but it can be shown that eccentricity is dampen out as GWs naturally tend to circularize the orbit.

The time before the merger corresponds to $\tau_{GW}/4$, for a typical BNS this corresponds to about 50 Myr. The luminosity of the emitted radiation is

$$L_{GW} = \frac{32}{5}\frac{M_1^2 M_2^2 (M_1+M_2)}{a^5} \tag{1.7}$$

This is strongly dependent to the inverse of the distance between the stars. For a canonical system at the initial separation of $\sim 1R_{\odot}$, $L_{GW} \approx O(10^{32})$ erg/s, while at the last orbits, right before the merger, the separation is so small that the energy emitted reaches $O(10^{53})$ erg/s, comparable with the luminosity of all the visible matter of the Universe.

Finally, the characteristic frequency is typically twice the frequency of the orbit (being a

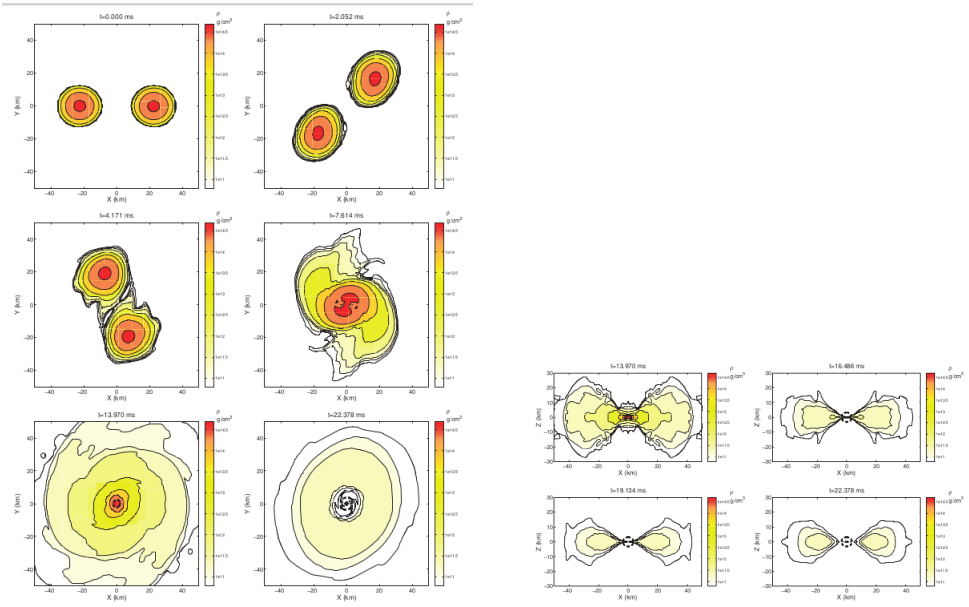

(a) Equal mass BNS merging

(b) Accretion torus evolution

Figure 1.3: Scheme representing the isodensity contours in a x-y plane for the evolution of a high mass binary in which the components have equal initial masses. Image taken from [25], reprinted from [27]

quadropole emission) and is given by:

$$f_{GW} = \frac{1}{\pi}\sqrt{\frac{M_1 + M_2}{a^3}} = 194\left(\frac{M_{tot}}{2.8M_\odot}\right)^{1/2}\left(\frac{a}{100km}\right)^{3/2}\text{Hz} \tag{1.8}$$

1.2.2 Merger

In the very last moments of the inspiral phase the binary separation becomes no larger than a few times the NS radii. The evolution is still driven by the gravitation radiation timescale, but now it becomes really short, lasting only a few seconds or less.

According to the literature the total mass of known binaries lie in the range [2.65-2.85] $M_\odot$ and it seems that, for most of them, star masses are very similar [25]. The details of the merger are strongly mass and also EoS dependent, however the general picture suggests that the amount of mass loss during the inspiral is very small, only about $10^{-4}\,M_\odot$ [26]. Hence the mass of the remnant object roughly corresponds to the sum of the two initial NS masses. This is usually heavy enough to collapse into a BH, either promptly or after some delay.

As we said before, in order to provide an accurate description of the merger phase, heavy numerical GR-MHD simulation are required. The detailed description of the numerical formalism implemented is beyond the scope of this work, however here we briefly summarize the outcome of a few simulations carried by [27] and well discussed in [25].

Dynamics of equal mass binaries

The most studied case, and with the most likely occurrence in nature, is the scenario in which the two components of the BNS have nearly equal masses. For the simulation [27] chose a high-mass binary with initial component's mass of $1.5M_\odot$, hence total gravitational mass of $3M_\odot$. The system is modelled with a 'hot' (ideal fluid) EoS. Although this may be a simplistic approximation, it has the property of being non-isentropic thus it allows heat exchanges hence the development of internal shocks affecting the fluid's dynamics.

The simulation starts with the stars placed at about 45 km of distance, still in the slow inspiral phase which is progressively speeding up (panel 1 of Fig 1.3a). After three or four orbits the NSs approach each other and the formation of some tidal waves, due to the gravitational interaction (with an amplitude directly proportional to the NSs masses) is observable in the surface. These perturbations eventually lead to the formation of the rest-mass density oscillations in the central regions of the system, together with larger and larger ejection of matter, stripped from the surfaces in the form of winds (panel 2 and 3).

At the merger (panel 4) finally the stars collide with an impact parameter relatively large. This reduces the strength of the pre-existent shocks but, at the same time, it produces a great amount of shear which in turn will lead to the formation of dynamical instabilities such as the Kelvin-Helmotz (K-H) instabilities. At this point the final remnant of the merger has been generated, however the two stellar cores are going to break up again producing a bar-deformed structure which rotates for several periods before disappearing, during this process the remnant loses angular momentum and increases its compactness while emitting GW in a run-away fashion. This process will finally end when the remnant is sufficiently compact to collapse into a rotating BH (or a stable NS, see next section) and an event horizon is formed (panels 5-6).

During the merger the system has left outside the horizon a vast amount of material in which a large angular momentum has been deposited. Eventually this material will inflow again toward the compact remnant forming an accretion torus with average density of $10^{12} - 10^{13}\,\mathrm{g/cm^3}$, a vertical size of $\approx 20\,\mathrm{km}$ and a larger horizontal size of $\approx 60\,\mathrm{km}$ (Fig 1.3b). The torus originally presents some axisymmetry but it's also far from equilibrium and it's subjected to large oscillations due to the compensation between the BH gravity and the excess of angular momentum. This is incremented by GW emissions since in this phase the torus still have a large quadrupolar momentum. As a result of the combination of these effects, torus material is drifted towards the BH and starts the accretion process, quickly reducing its mass from $\approx 0.6\,M_\odot$ up to $O(0.01)\,M_\odot$.

Although the (nearly) equal mass case is the more probable scenario to be found in nature, we should also expect some degree of asymmetry in the initial mass distribution, hence it is interesting the study of the case with significant deviations from mass ratio of 1. We will follow the discussion from [25, 26].

Dynamics of unequal mass binaries

Let's consider again a massive BNS system with total gravitational mass $M_{\mathrm{tot}} = 0.7\,M_\odot$ and modelled with an ideal-fluid EoS. This time the component's mass are unequal, yielding a mass ratio of $q = \frac{M_2}{M_1} = 0.7$.

The differences between this and the previous case are evident already at the beginning of the simulation: in the unequal case inspiral phase the less massive companion is disrupted by the tidal pull of the heavier primary NS and starts to be accreted onto this one (panels 1-3, Fig 1.4a). During this process a large fraction of the lighter NS's angular momentum is deposited onto the primary which, as a result, is going to feel a strong torque which ends up generating an extended tidal tail (panels 4-5). Such tail will soon become a spiral arm which is quite efficient in carrying outwards the excess of angular momentum through matter ejection.

At the end of the process the matter in the spiral arm which is still gravitationally bound to the central remnant will infall in the form of an accretion torus, which turns out to be quite more massive than the torus generated in the equal masses case. Finally, due to the high mass of the original system, the remnant quickly collapses into a BH as in the previous case but now with the difference of the presence of a kick (< 100 km/s) due to the asymmetric gravitational radiation emitted in the last moments before the merger.

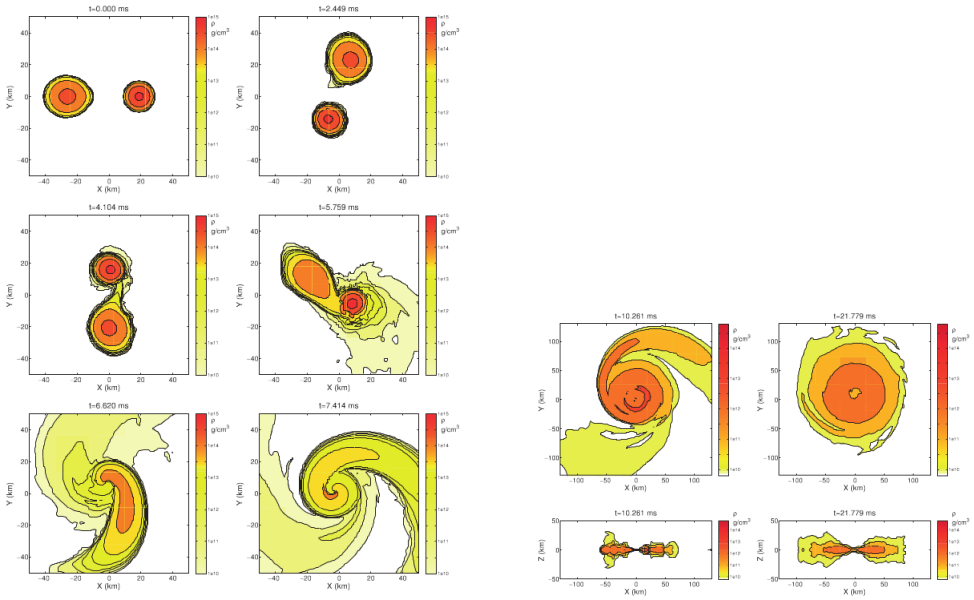

(a) Unequal mass BNS merging (b) Accretion torus evolution

Figure 1.4: Scheme representing the isodensity contours in a x-y plane for the evolution of a high mass binary in which the components have a mass ratio q=0.7. Image taken from Rezzolla, 2013 (reprinted from Rezzolla et al 2010)

Fig 1.4b shows the rest of the evolution but focusing on the accretion torus, which is quite different with respect to the one generated in the equal masses case (Fig 1.3b).

Indeed the torus in the asymmetric scenario has a more irregular geometry (panel 1, Fig 1.4b) with the presence of the large spiral arm not yet accreted in the central regions. Moreover it turns out to be about a factor ≈ 3 larger in size and a factor ≈ 200 more massive than the symmetric case.

Let's now focus on later times, when the BH is formed and the torus starts to feel a strong gravitational pull from the central regions, which will trigger radial oscillations. In the equal masses case the potential well is axisymmetric, this means that the torus can be well approximated by a relativistic disk oscillating from its equilibrium configuration with evidences of harmonic relations between the oscillation frequencies [28].

In the unequal-mass binary, instead, the amplitude and the periodicity of the oscillations are way more irregular and the dynamics turns out to be a lot more complicated, at least until the torus is able to regain some axisymmetry trough accretion. In this last case the spatial variations are very strong especially at the beginning of its evolution. This allows the torus to rapidly expand and eventually eject the unbound part of the large spiral arm, covering in the process several hundreds of km from the central BH (where in the equal mass case, the torus doesn't reach more than $\sim 30\,\mathrm{km}$).

Higher densities seem to be reached, near the BH, by the wider torus. In fact, since during the merging a large fraction of the outer layers of the less massive star are swept away, the produced torus has a larger angular momentum thus it can sustain comparatively more density.

In turn, the feeding mechanism of the BH on the torus seems to be extremely dependent on the asymmetries, while in the equal masses scenario the total mass of the system drops immediately after the BH formation, in the unequal case more mass is preserved in the disk.

The last important difference concerns the amount of lost material. For the equal mass binary the torus is less expanded and all the matter is bound, while for the unequal case, in the

outermost, low-density regions, some matter is able to leave the system through an out-flowing wind likely produced by the high temperatures of those regions.

At the end of the day, the general result suggests that the mass of the torus increases inversely with the mass ratio however this scaling is not monotonically since it does depend also on the total initial mass of the binary.

1.2.3 After Merger and Ringdown

After the dynamically complex merger phase, the system will try to reach a new stable configuration, during which GWs are emitted with new 'Ringdown' waveform profile. The Ringdown phase is driven by the balance between the mass and the rotational profile of the remnant, in particular its initial mass will determine in which metastable phase the system will end up. This is summarized in Fig 1.5 and here below.

There exists a maximum value for the mass ($M_{\rm max}$) an isolated, non-rotating star should have to avoid the collapse into a BH, this is usually strongly dependent on the choice of the EoS which determines the nuclear matter contribution which opposes to gravity. Thus, the ratio of the remnant mass over $M_{\rm max}$ will determine its final fate [3, 25].

$\mathbf{M < M_{max}}$: In the least massive possibility the merger would form an indefinitely stable, non rotating NS. From this point on, the only changes the object will undergo are driven by Neutrino and photon cooling. This scenario is included in the last panel of Fig 1.5 (without the SMNS phase).

$\mathbf{1 < M/M_{max} < 1.5}$: About $1.5\,M_{\rm max}$ corresponds to the limit for having a uniformly rotating NS, it's slightly dependent on the EoS ([7] and references therein). A system which ends up in such mass range will quickly evolve into a *supramassive* NS (SMNS). They are hot and axisymmetric systems, stable against the gravitational collapse as long as they are able to maintain a uniform rotation. Should a dissipative or a radiative process (like a combination of viscosity, pulse emission or magnetic coupling to the outer disk) drain out its angular momentum, they will eventually collapse back into a BH.

$\mathbf{1.5 < M/M_{max} < 2}$: Higher mass remnant, which overcomes the limit for uniform rotation stability, enter the *hypermassive* (HMNS) regime. A HMNS can sustain very large masses whose gravitational pull is counter-balanced by a rapid differential rotation. This allows them to survive quite longer than the dynamical timescale, from some millisecond up to a few seconds. HMNS come with a triaxial configuration which allows GW emission and probably also matter ejection into the outer accretion disk. Again, once dissipative and radiative effects take place dampening the differential rotation, the HMNS will collapse into a spinning BH. The energy released in this process could in principle power GRB emission, the life prior to the collapse could contribute to the observed delay between GW and GRB.

$\mathbf{M/M_{\mathit{max}} > 2}$ For the heaviest of the possible remnants the inevitable fate is a promptly collapse into a rotating BH.

Finally let's notice that in every case a geometrically thick, low-density and gravitationally bound torus will surround the remnant, no matter the outcome [7]. This tori are expected to eventually fall into the central compact object and accrete material on timescales which depend on the most efficient dissipative (or radiative) process. During the accretion the disks are expected to heat up and possibly emit EM radiation. Moreover its coupling with the internal material will favour dissipative processes hence the loss of angular momentum and the collapse into a BH.

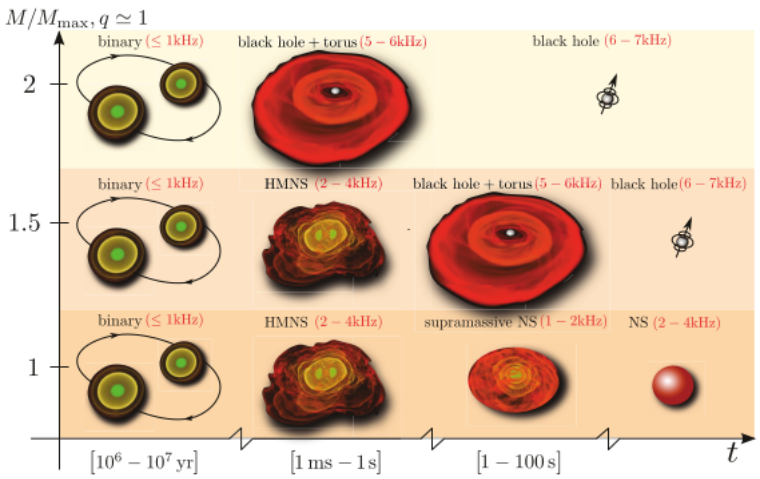

Figure 1.5: The possible fates for the merger's remnants. The outcome depends strongly on the mass of the remnant (see discussion in text). This diagram also indicates the typical timescales of the processes (black) and the characteristic ringdown frequencies (red). The cartoon was drawn by Rezzolla and Kaelher ([25]) using fully GR-MHD simulation for an equal mass binary scenario

1.3 Role of Magnetic fields

BNS mergers are very complicated dynamical processes which involve many different aspect of physics. Among others, the presence and the evolution of magnetic fields involved in the process may clarify some of the details characterizing both the merger and the post-merger remnant, providing along the way some constrains on the characteristics of the phenomena to be matched with the observational features (such as kilonova transient and SGRB production). The appropriate way to tackle this topic, within theoretical framework, is to implement and run full GR-MHD simulations, which is quite numerically expensive and up to date only up to $\approx 250ms$ from the time of the merging have been covered by full 3D simulations in presence of magnetic fields. [29, 30, 31, 32, 33].

1.3.1 Small scale amplification

The energies associated to magnetic fields in the components of a BNS are usually rather high. Typical values of their strength are in the range $[10^{11} - 10^{15}]\,\mathrm{G}$ ($\approx 10^{45} - 10^{48}\,\mathrm{erg}$), where the upper interval of $[10^{14} - 10^{15}]\,\mathrm{G}$ is the 'magnetar' range [32]. Nevertheless, during the merging the magnetic energy gets strongly amplified up to very high values such as $[10^{50} - 10^{51}\,\mathrm{erg}]$ (hence a field stronger than $\geq 10^{16}\,\mathrm{G}$). Such amplification is mostly due to the rise of the Kelvin-Helmotz instabilities (KH), the Magneto-rotational Instabilities (MRI) and of the magnetic winding [34].

Kelvin-Helmotz instabilities are the main sources for the amplification of the magnetic fields involved during the merging. When the two NSs plunge and finally get in contact, a vortex sheet (i.e a shear interface) is developed [25]. This configuration is unstable and may lead to the formation of a series of vortexes in the contact region [35, 36]. Even if this is a purely hydrodynamic phenomenon, it becomes extremely important when the NSs are embedded inside strong magnetic fields. In fact, KH instabilities will twist the poloidal magnetic field lines reconfiguring the central regions of the merger's remnant into a growing strong toroidal component up to the point it gets comparable with the poloidal field. Finally, the energy equipartition rises up the overall magnetic field.

KH instabilities are extremely important in the very initial phases of a BNS merging since they are able to rise the magnetic energy up to values $\geq 10^{50}\,\mathrm{erg}$, corresponding to a field strength

$\geq 10^{16}$ G. KH instabilities act at very small wavelengths, with the small-scale vortexes growing faster than the larger-scale ones, this makes practically impossible to fully resolve them even with the the most expensive simulations [34], hence sub-grid modelling is often required to account for their contributions.

When, after few milliseconds, the remnant finally stabilizes (if direct collapse has been avoided) into a metastable massive NS surrounded by the ejected material, KH instabilities slowly wear off and get substituted by the magnetic winding and the MRI. While both of these mechanisms are driven by the differential rotation of the remnant, the magnetic winding results in a linear amplification of the toroidal field in the equatorial region, whereas the MRI are associated with stronger, non-linear, modes which cause the magnetic field to increase exponentially [37]. Let's notice that, in order to work, the MRI requires a negative gradient for the angular velocity Ω toward the outward, radially direction. This is usually satisfied in the outer regions of the HMNS, whereas in the central ones, say for radii ≤ 10 km, this is not true and the instability cannot take place. The fastest growing MRI mode has a scale which increases with the magnetic field intensity: $\lambda_{MRI} \approx \frac{2\pi B}{\Omega\sqrt{4\pi\rho}}$. Hence they are easily resolved at strong enough values for the magnetic field, this happens already after about 40 ms from the merger [38].

The magnetic energy usually reaches its maximum value around 10^{51} erg, after which, simulations show that the magnetic fields are saturated and are going to remain more or less constant during all the later stages [30].

1.3.2 Remnant's magnetic configuration

The merger phase is fundamental in determining the final configuration for the remnant's magnetic field. In general, starting from the poloidal dominated structure of the two initial NSs, a toroidal component is always generated in the equatorial regions [38]. Then, after only few milliseconds, the MHD turbulence amplifies the magnetic energy building up comparable magnitudes for the two components.

If the promptly collapse has been avoided and a HMNS takes form, the rapid differential rotation of the bulk, which sustains it against the gravitational infall, provide a twist to to the poloidal field lines along the spin axis, this may lead to the formation of an axisymmetric helical structure (20 ms case of Fig 1.6) which in principle can accelerate the ejection of a collimated outflow [30].

From this point on the final magnetic configuration is channel dependent, indeed a longer lived metastable remnant would present differences in the field line composition with respect to one which has rapidly collapsed.

Collapse to a BH

After some time (in the range [0-100] ms) the hyper massive remnant could eventually collapse into a BH. During the process, the material which is located in the closer regions gets swallowed up, as a result about the 80% of the magnetic energy promptly disappears [39]. However, the remaining matter in the vicinity (up to ~ 200 km) will feel the newly born gravitational potential, hence it'll end being pulled toward the BH and forming an accretion disk [31]. During the process, a funnel of lower density is opened up to an half-opening angle of $\sim 30°$ [33, 38].

The disk is composed by a mixing of poloidal and toroidal field lines with the latter ones dominating the contribution. The differential rotation favours the growth of MHD instabilities which will in turn amplify the magnetic field and account for the energy lost during the collapse. Inside the polar, low-density, region the field lines are stretched toward the radial direction, while at the interface between the disk and the funnel the magnetic field gets twisted and entangled, favouring the helical structure build-up around the spin axis [33].

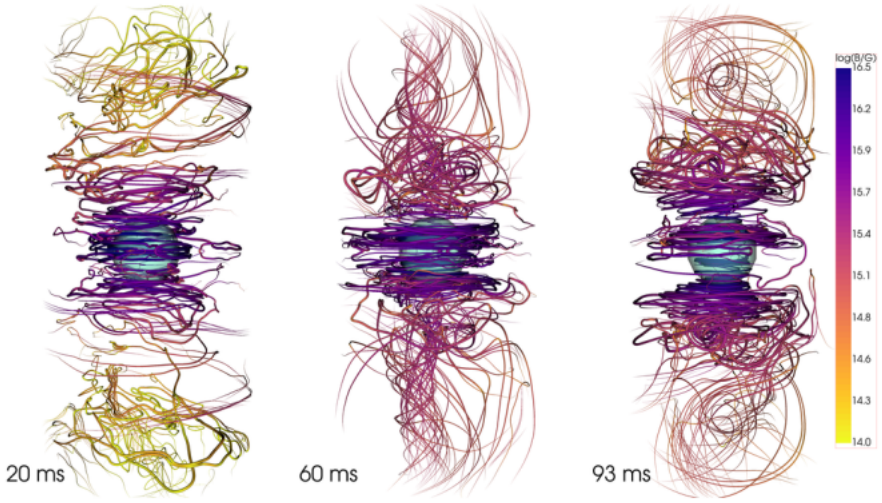

Figure 1.6: The image represents the magnetic field lines configuration at 20 ms, 60 ms and 93 ms from the time of the merger (assuming no collapse until such times). The cyan sphere has radius of 10 km and represents the internal regions of the remnant. The color of field lines summarizes the strength of the magnetic field. The image is taken by [39]

If the initial field is strong enough, the magnetic pressure could in principle exploit the low-density inside the funnel to stop the inflow converting it into a collimated outflow, maybe even a relativistic jet.

Magnetized Neutron star

In some cases the remnant may avoid the collapse, stabilizing forever into a strongly magnetized NS.

The initial massive remnant is composed by a deformed central object embedded into a torus-like envelope. The rapid differential rotation supports it from the collapse and it's partitioned in a structured profile: in the central region a slowly spinning bulk is surrounded by faster rotating outer layers up to a maximum of $\sim 15\,\mathrm{km}$, after that the velocity profile steadily decreases [40].

After few milliseconds the shear viscosity in the core will eventually transport angular momentum inward, dampening out the maximum angular velocity, in the end establishing a uniform rotation. In the outer layers instead a differential rotation following a keplerian profile persists.

In order to compensate for the angular momentum redistribution, some of the kinetic energy is turned into heat and as a result the remnant core expands. At the same time the strong enhancement of the magnetic fields will favour the development of turbulence which will in turn increase the overall pressure, causing the ejection of material from the outer layers into the surrounding. The combination of these effect favours the dampening of the differential rotation and causes a slightly reduction of the remnant compactness [25].

Notice that if the star is not able to retrieve an equilibrium configuration it will eventually collapse, instead if it manages to survive, the overall structure tends to restore some isotropicity. In fact, at later times the magnetic fields get more disordered, this will cause a more uniform ejection of magnetically-driven outflow and in turn the surrounding torus will inflate toward a spherical symmetry.

At $\sim 100\,\mathrm{ms}$ from the merger (last case in Fig 1.6) the magnetic field is highly irregular, toroidal field lines are dominant and the helical structure is no longer visible; at large scale (O(100) km) the magnetic field loops around suggest the formation of a global, magnetar-like structure.

However, longer simulations (up to $\sim$ 250 ms) [30] show that in certain cases, provided a

strong initial magnetization, at later times and at large scales a helical configuration is eventually produced, allowing for the ejection of a collimated outflow.

1.4 Merger ejecta and post-merger winds

A BNS merger event usually introduces in the surrounding environment a huge quantity of neutron-rich material. In general, between the merger and the post-merger phases up to $\sim 0.1\, M_\odot$ [41] of mass are ejected from the system, and this may happen in a variety of ways: either through dynamical processes which take place during the collision, or via barionic winds expelled by the remnant. The quantity of expelled mass and its properties, such as compositions and velocities, depend on the mechanism which caused the ejection.

1.4.1 Dynamical ejecta

The material expelled from the system during the merging, on dynamical timescales, is called *dynamical ejecta*. Usually the mass lost trough dynamical ejecta amount to $[10^{-4} - 10^{-2}]\, M_\odot$, with an escaping velocity of $\sim 0.3\, c$ [42] and it's only weakly dependent on the magnetic fields.

There are two main mechanisms which can trigger a dynamical expulsion of material: the tidal ejection and the shock-driven ejection. Both contributions on the system mass loss rate depend on the final remnant channel (in other words, on the delay time before the collapse) and on the asymmetry on the initial mass distribution.

During the merger the contact interface between the two NSs get squeezed out by the hydrodynamical pressures of the stars, as a consequence quasi-radial oscillations kick in, ejecting the shock-heated material at many different angles [41].

The other mechanism involves the the tidal tails formed in the last moments of the inspiral phase. During the merger, the spiral arms increase their angular momentum and expand, eventually causing some mass to unbound and leave the system. As we discussed in the previous Section, the tidal tails formation is more relevant as the the difference between the initial masses is larger, hence for lower mass ratio q the tidal ejecta is favoured with respect to the shock-driven process. If the merger leads to a promptly collapse then the shock-driven ejecta contribution becomes negligible since all the material at the contact interface would get immediately sucked up beyond the horizon, tidally ejecta thus dominate and the bound material falls back forming an accretion disk surrounding the equatorial region of the BH. In the case of a HMNS remnant, the presence of a hard surface changes the shape of both the shocked and the tidal ejecta. The material outflows will be slower and more massive, dominating in the polar regions where the densities are lower. The in-falling matter from the spiral arm will embed the entire surface of the HMNS, rather than only the equatorial region as in the collapse scenario. The overall effect is an increment of the material at the poles [3].

1.4.2 Baryon Wind ejecta

After the more violent merging phase, the remnant is still able to lose mass through more or less collimated outflows. While hydrodynamical processes were more important in determining the dynamical ejection, now neutrino cooling and the magnetic field configuration start becoming relevant.

These kind of ejecta take place in the form of winds, their properties usually depend on the life of the remnant. Winds can originate either from the central, core, region of the merger product or from the hot accretion disk surrounding the (eventually) collapsed remnant.

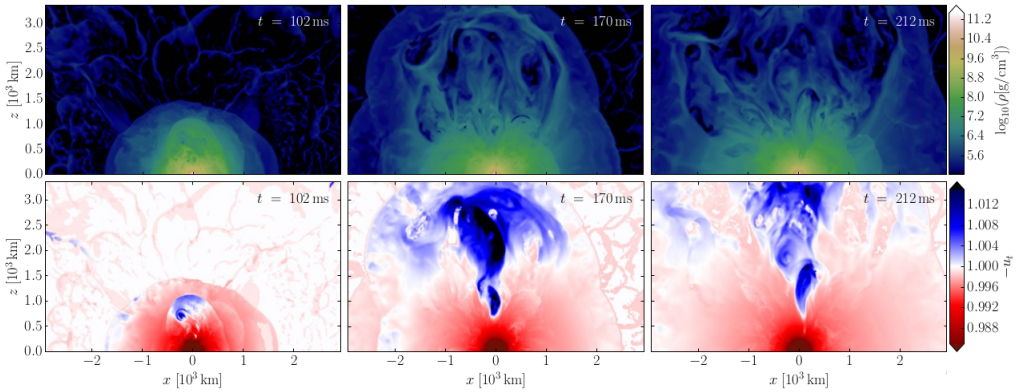

Figure 1.7: The images reports the outflow captured at different times from the merger, from the remnant of the simulated merger in [30]. *Top:* The rest mass density, *bottom:* the lorentz factor. The color blue represent the unbound matter

Disk outflow

The BH's accretion disks originated from a merger are usually quite massive, they span in a mass range of $[0.01 - 0.3]\, M_\odot$ [41]. The expected mass loss rate from accretion disk is usually quite elevated and it can compete with (if not dominate over) the dynamical ejecta. This is mostly due to a combination of neutrino cooling and MHD instabilities development.

During the accretion, the disk overheats and produces strong neutrino winds. However, as it evolves, the generation of MRI due to the differential rotation profile leads to turbulence and strong magnetic stresses which in turn lead to an expansion of the disk with a consequent decrease in the accretion rate (hence on the neutrino production).

When the cooling process becomes inefficient, the outflow switches from being neutrino driven to be led by viscous-turbulent winds, the amount of mass loss during this phase increases with the increasing of the BH spin. At the end of the day, about the 40% of the initial torus mass is lost through winds, this ejecta is usually neutron-rich and relatively slow, $v = [0.01 - 0.1c]$ [38, 41].

The disk ejecta contribution is not only relevant in the case of a long lived NS, but it is in general dominant with respect to the promptly collapse case. If the collapse happens after few ms then the mass and angular momentum of the central object have more time to redistribute, this allows for the formation of more massive accretion disk. Moreover, due to the presence of a hard, neutrino emitting, surface, the outflow gets to unbound up to even the 90% of the initial disk mass for very long-lived remnant [41]. It should be noted that in the case of a highly magnetized MNS remnant the surrounding material is isotropically distributed hence it's not an 'accretion disk' in the classical sense [39].

MNS outflow

When a massive remnant (either the HMNS or the SMNS) is able to survive long enough, its outflow can become comparable or even more important than disk ejecta. In particular, it is shown [43] that if the remnant does not collapse for at least 50 ms than its neutrino luminosity ejects $\sim 10^{-3}\, M_\odot$ overcoming the disk contribution.

Anyway, the main ejecta-driven mechanism for long-lived MNS is the formation of strong magnetic winds. As seen in the previous chapters, after few ms the magnetic lines become disordered, in this regime the outflow is mostly isotropic and quite massive [30]. After some time, a large scale helical structure may form along the spin axis, this triggers a magnetorotational launching mechanism for which the increasing magnetic pressure gradient pushes some mass along the radial direction. There the material interacts with the baryon-polluted environment

and drills through it up to when, after some time (≈ 100 ms), it's able to emerge and to form a collimated outflow (see Fig 1.7).

The interaction between the isotropic baryon wind and the collimated outflow yields a wide angle structure with a velocity profile decreasing as it gets farther from the polar axis. After about $\sim 250\,\mathrm{ms}$ the process is suppressed and the amount of lost mass increases negligibly.

The magnetic wind-driven ejecta is quite massive and baryon loaded, it amounts to a mass of $[0.01 - 0.03] M_\odot$ moving at $[0.1 - 0.3]\, c$ [44].

1.4.3 Kilonova

BNS mergers in general produce two main EM signals: Short GRBs, a very sharp and powerful flare in the gamma-ray band (on which we will focus in the next Chapter) and a more isotropic kilonova transient.

Kilonovae are most likely powered by the radioactive decay of heavy nuclei produced through rapid-neutron capture or *r-processes*. This nuclear reactions occur when heavy stellar material (up to the iron) encounter a neutron-rich environment, then the capture of the free neutrons allows for the synthesis of heavier-than-iron element like gold, which cannot be produced in a normal stellar environment. In order to have a stable process, the r-processes must act on timescale shorter than the neutron decay timescale (β decay, $\sim 15\,\mathrm{min}$) [41].

A critical quantity describing the environment's neutron-richness is the *electron fraction:*

$$Y_e = \frac{n_p}{n_n + n_p} \tag{1.9}$$

where n_n and n_p are the number density of neutrons and protons respectively. In general stellar material has a fraction $Y_e \geq 0.5$ while neutron rich matter is characterized by $Y_e \leq 0.5$, which has to be fulfilled to trigger the r-processes.

Identified kilonovae such as AT2017gfo (the second EM counterpart of GW170817, companion of GRB 170817A) show transient multiwavelength, optical/infrared spectra, visible up to ~ 10 days from the chirp signal (marking the merger). Their signal depend mostly on the composition of the ejecta acting as a site for the r-processes, and it is determined by how far the nucleosynthesis has been able to produce heavy elements. In general, we can identify at least two different components [3, 45]:

1. Blue kilonova: this component is characterized by a mass in the range $[1.5 - 2.5]10^{-2} M_\odot$ rapidly expanding with velocity $\approx 0.2{-}0.3\, c$. Its opacity is relatively low: $k \sim 0.5{-}1\,\mathrm{cm}^2/\mathrm{g}$. These properties suggest that the blue kilonova site is most likely lanthanide-free, yielding $Y_e \geq 0.25$ [29]. The poverty in free neutrons may be due to the neutrino irradiation in the early phases of the the merger, if the blue kilonova component has been produced by the earlier ejecta, then the strong neutrino winds may have interacted with the free neutrons as

$$\nu + n \rightarrow p + e^- \tag{1.10}$$

   increasing the electron fraction. Usually the blue component is not the dominant part of the kilonova spectra and it peaks after ~ 1 day from the merger.

2. Red kilonova: The principal part of the spectra is represented by a more massive and opaque component. The red kilonova spans a mass range of $[4 - 6]\, 10^{-2}\, M_\odot$ and has velocity $\sim 0.1\, c$. The much higher opacity $k \sim 10 - 30\ \mathrm{cm}^2/\mathrm{g}$ testify a lanthanide-rich environment, $Y_e \leq 0.25$. This component is visible for more time than its blue counterpart, peaking after ~ 1 week [29].

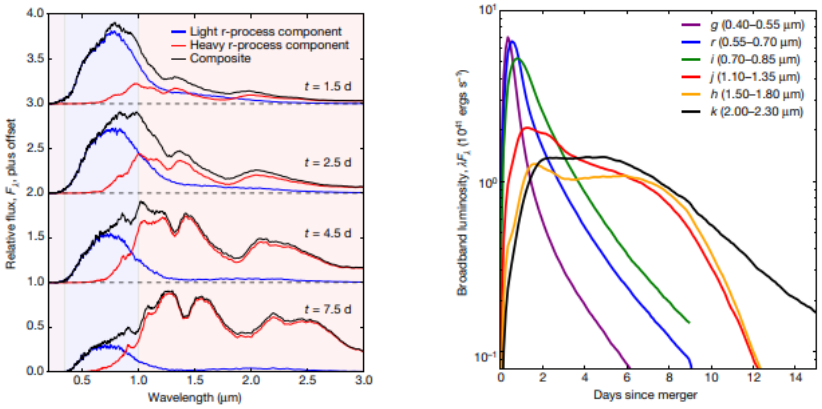

(a) Spectral time series (optical/IR)

(b) Composite broadband lightcurves

Figure 1.8: Model proposed to explain GW170817a kilonova counterpart. It's given by the superimposition of a red and a blue components. *left:* The blue and the red curve represent the respectively kilonova components, the black line represents the sum of the two contributions. *right:* The lanthanide-free component produces the rapidly evolving emission peaked in optical, while the heavier component produces the extended IR continuum. All these properties are featured in the AT 2017gfo signal. Image taken by [45]

We notice that real kilonova signals are quite complex, with the above description corresponding to a simplified model attempting to explain the light curves. More complicated scenarios with more components and including interactions between them have been proposed [41, 43].

According to observations, when averaging over the Galaxy the required production rate of heavy nuclei, say those with atomic mass number A > 140, is $\sim 2 \times 10^{-7}\, M_\odot/yr$ [46]. When we take the rate of detection of NS-NS merger of $\sim 10 yr^{-1}$ given by Advanced LIGO/Virgo at designed sensitivity (considering an horizon of ≈ 200 Mpc) [47], then the amount of r-processed mass per merger should be:

$$\langle M_{r-proc} \rangle \approx 10^{-2} M_\odot \left(\frac{R_{NS-NS}}{10 yr^{-1}} \right)^{-1} \tag{1.11}$$

Even if it's not still clear which type of outflow should be associated to the blue or red kilonovae, the overall merger ejecta may fill this limit suggesting that NS mergers are among the most important sources of heavy nuclei in the Universe.

Chapter 2

Short gamma-ray bursts

In 1967 high energy gamma-ray flares were detected by the U.S military satellites Vela. Even if this event was initially a cause of concern, it didn't lead to an escalation of the Cold War as many feared but instead to one of the main discovery of modern Astronomy: the existence of extragalactic, highly energetic, transient bursts called *gamma-ray burst* (GRB).

GRBs are the most luminous explosions in the Universe since the Big-Bang. They emit an isotropic equivalent luminosity, L_{iso} around $[10^{51} - 10^{53}]$ erg/s, as a comparison the entire Milky Way luminosity (provided by the stars) is 'only' $\sim 10^{44}$ erg/s. To further increase the amazement, GRBs are launched by stellar-sized objects which incur in catastrophic events that take place in very short timescales, around few milliseconds [48].

There are many differences among GRBs population and they're divided in two macro families [49]:

- Long gamma ray bursts (LGRBs): LGRBs have a longer prompt emission duration which peaks in a time between [2-20] s. LGRBs are usually discovered in regions with a rich star formation ratio and are in general associated to core-collapse explosions of massive stars.

- Short gamma ray bursts (SGRBs): SGRBs are shorter lived (< 2 s) flares which span a harder spectra with respect their longer counterpart. Short gamma ray bursts can be found in every type of environment but they are usually associated with star-poor regions with a low density surrounding medium. The origin of SGRBs was discussed longer than the LGRBs one: only recently with the combined observation of the multimessanger signal GW170817/GRB 170817A the canonical paradigm of SGRBs as result of a binary merger have been finally accredited as the correct scenario.

The main criterion adopted to distinguish between the two families is indeed the duration of the burst. A signal which lasts for $> 2s$ will be considered a Long GRBs, while one which peaks at time $< 2s$ will fall into the Short GRBs class.

It's worth noticing that, nevertheless the many differences, LGRBs and SGRBs in the initial 1-2s of their prompt emission are very similar, almost indistinguishable. This may suggest a similar spectral evolution [50].

This chapter is going to focus on the short-hard GRBs family which is intimately linked with the BNS mergers. In Section 2.1 the main observational features of a typical SGRB signal are discussed. In Section 2.2 are shown the more accredited launching mechanism scenarios, trying to connect with the theory discussed in the previous Chapter. Finally, in Section 2.3 will be presented the most recent results for the propagation and possible structure of the relativistic jets associated to the burst. In particular, the case of GRB 170817A will be explored.

2.1 Observation

The main sample of GRB was obtained between 1991-1997 by the Burst and Transient Source Experiment (BATSE) instruments whose observations covered the whole sky [51]. BATSE was able to work in the energy range of 20 keV-1.9 MeV thanks to eight Large Area Detectors (LADs) and in the range 10 keV-100MeV through eight Spectroscopy Detectors (SDs). During the BATSE era it was defined the T_{90} measure which quantifies the duration of a burst as the time interval in which the counts between the 5% and the 95% of the fluency are collected by the detector [48], this allows for the first distinction between Long GRBs and the Short ones.

BATSE provided the very firsts understanding on the nature and on the properties of GRBs, however it lacked the information on their distances. The first advancements in the X-ray astronomy, through the missions BeppoSAX and HETE [52, 53] allowed for the detection of longer wavelength counterparts (i.e the afterglow) of more than 100 GRBs, this provided the event localizations and the identification of their cosmological origin [54].

Nevertheless, the actual breakthrough on the science on GRBs is due to the *Swift* observatory launched in 2004 [55]. It carries both large-field (BAT) and narrow-field instruments (XRT,UVOT), hence it's able to identify burst and immediately search for their X-ray counterpart, providing in the end a quite accurate estimate of their position. The prompt response and high accuracy of *Swift* allowed for the direct observations of the GRBs's early afterglow, revolutionizing the entire sector. The last mission directly dedicated to GRBs was launched in 2008 by NASA: the *Fermi* Gamma-ray Space Telescope (FGST) [56], which is still providing great insights on the details of GRBs emissions and spectra. Finally, the last revolution in the field was recently brought by the start of Multi-Messanger astronomy, in particular with the first detection of gravitational waves [57]

The interpretation of GRBs from observational data is all but trivial as spectra and lightcurves of the events present strong variability, even for elements of the same class. In all generality the short GRBs have a harder spectra and are less bright than the long GRBs, emitting a $L_{iso} = [10^{49} - 10^{51}]$ erg/s. Different GRBs events (or *triggers*) present different features, however there are two main ingredients which are in general present: the *prompt emission* and the *afterglow*. They each present their own peculiar lightcurve and spectrum. Most likely the prompt emission and the afterglow are produced in different sites and through different mechanisms [48].

2.1.1 Prompt Emission

With prompt emission is generally intended the very peaked, highly variable, pulse emitted in a T_{90} period. Usually the prompt emission peaks in the gamma-ray band, however, more broadly, all the smaller wavelengths contributions, if detected in the same period, are often considered too

In Fig 2.1 a couple of prompt emission lightcurves for SGRBs are shown. In general they are quite irregular and may present different signatures which can be used to probe some properties of the central engine.

Among the more typical SGRB features we find:

- Main Peak: The main event is always modelled as a combination of asymmetric pulses. The typical pulse model present a sharper rising phase and a shallower decay (*fast-rising, exponential decay*, also called FRED profile)[48]. In general they vary with the energy according to some power law: $w(E) \propto E^{-\alpha}$, with typical values of $\alpha \sim [0.3 - 0.4]$ [58].

- Precursor: SGBRs event may follow some previous activity which is already able to trigger the detector. In general the precursors are less energetic ($\sim [10^{42} - 10^{47}]$ erg/s) and softer than the main peak, yielding a spectra which is essentially thermal. Precursor signals can

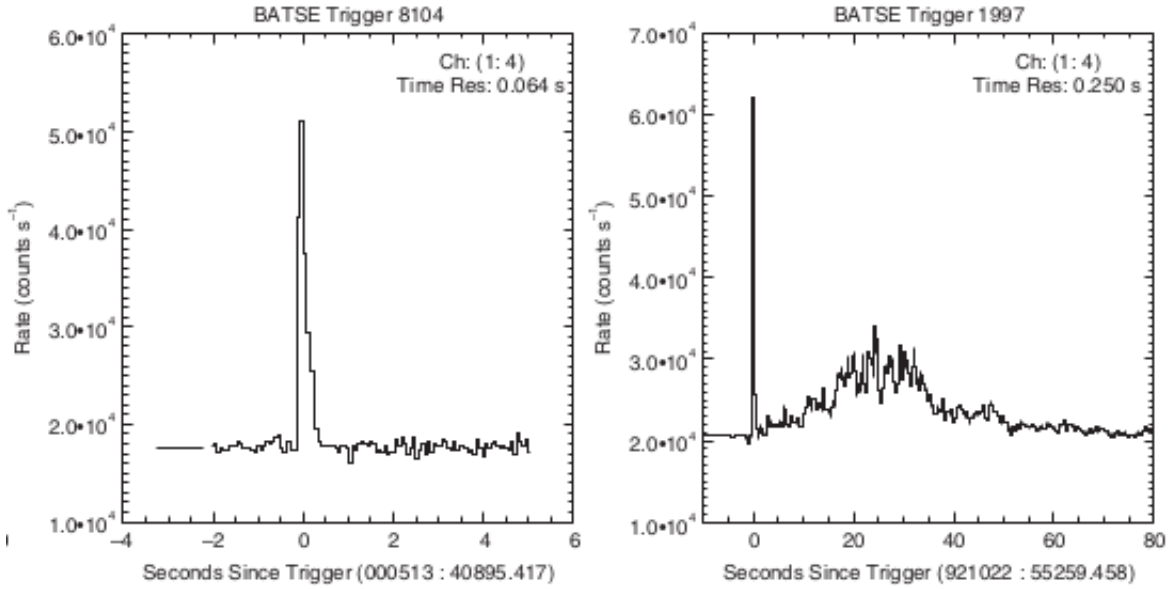

Figure 2.1: Both 8104 and 1997 come from BATSE catalogue of GRBs. The y-axis represents the photon count per second, while the x-axis shows the time since the detector is triggered by the a signal above the background. In the right image is shown an example of SGRBs with extended emission. Image taken from [48]

last up to $\sim 100s$, hence in principle they may be longer than the T_{90} period. An intensive study on *Swift* data reveals that $\sim$ 10% of SGRBs present some precursor profile [59]. While it seems that the main episode is independent from the presence of a precursor, the latter (if there) will share some of the properties of the main prompt emission. It is still not clear the physical process behind the precursor production, some models speculate that it comes from a more isotropic emission with respect the central peak [3], other suggest that the two signals can share the same mechanism but operating with variable power [48].

- Extended Emission: About the same quantity of SGRBs which have a precursor profile (around 10-15% of *Swift* signals [49]) have also an extended, softer emission which can last up to $\sim 100s$ so that they may even exceed the central peak fluency. Usually the extended emissions are characterized by the presence of plateaus or X-ray flares which can recall the onset of the following afterglow (even if they are still considered as prompt emission components). Again, the presence of an extended emission could be associated to some weak activity of the central engine, after the main event. Following this theory some model proposes that the extended plateau could be powered by the spin-down of a fast rotating magnetar, in this case a scenario in which the collapse has been avoided would be necessary [3].

When analyzing the signal at different wavelengths, it's found that the overall GRBs spectra is *non thermal*. Instead, usually a complete burst event is well fitted by a 'Band' function [60] which is formulated as a joint broken power law (with two spectral indices α and β), and smoothly connects the high and the low energy spectral regimes through an exponential profile:

$$N(E) = \begin{cases} A\left(\frac{E}{100keV}\right)^{\alpha} exp\left(-\frac{E}{E_0}\right) & E < (\alpha-\beta)E_0 \\ A\left[\frac{(\alpha-\beta)E_0}{100keV}\right]^{\alpha-\beta} exp(\beta-\alpha)\left(\frac{E}{100keV}\right)^{\beta} & E \geq (\alpha-\beta)E_0 \end{cases}$$

Where N(E) is the photon number spectrum, A is a normalization constant and E_0 is the break energy which separates the two regimes. It is also found that in most of GRBs the following

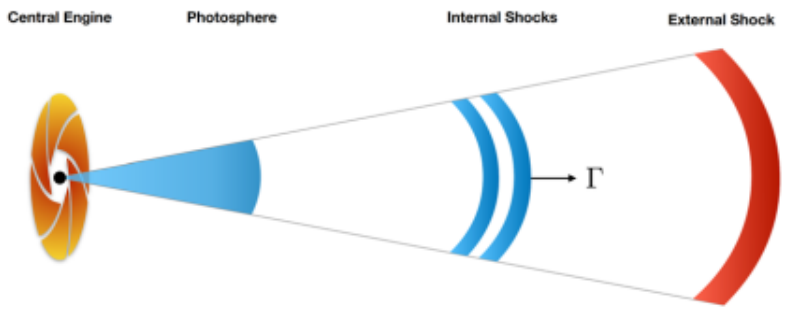

Figure 2.2: This simplified model is useful to provide possible explanations for GRBs emissions. Radiation needs to overcome photosphere in order to breakout from the jet. Moreover the mechanism behind the radiation production fixes also the site from which is emitted. Prompt radiation is assumed to be emitted either at the *photosphere* or behind it, due to the raise of *internal shocks*. The afterglow is most likely produced at the interface between jet and external medium, as consequence of *external shocks*. Images taken from [3]

relation is satisfied:

$$E_p = (2 + \alpha)E_0$$

where E_p is the peak energy in the spectrum. The non thermal profile allows for the spectrum to extend at higher energies, and it's usually a symptom of a non-equilibrium environment.

The Band function provides a good fit for the majority of GRBs spectra. However it has been hypothesize [61] that the actual spectrum is given by a superposition of three contributions: the dominating, non-thermal Band profile, a quasi-thermal component, and finally an extra non-thermal power law which extends at even higher energies. All the components may be generated through different processes and they can, in principle, be found with some correlations in at least some events [48].

GRBs signals are too energetic and present too much variability for being simple isotropic emissions from a central engine. The more accredited scenario states that GRBs are produced by ultra-relativistic jets which are launched by some compact and stellar-sized object. In the case of SGRBs such central engine would be the remnant of a BNS merger.

The site within the relativistic jet in which actually the GRBs is launched is still not definitely constraint, this strongly depends on the mechanism behind the burst launching and on the type of emission. The understanding of such mechanism could also shed light on the nature of the spectra components.

After launch the jets starts a very rapid expansion, if it maintains a constant lorentz factor ($\Gamma \geq 100$) and an almost uniform and isotropic emissivity (in the comoving frame), then it is referred to as a relativistic *fireball* and its shape can be simplistically assumed to be conical [3]. Alternatively one could hypothesize a more structured jet composition, with an angle-variable shape and a inhomogeneous density. Either the model, inside the jet the vast energy accumulated may be released in the form of radiation once the photosphere is reached. The photosphere is defined as the region in which the optical depth $\tau \sim O(1)$ (by convention it's assumed $\tau = 2/3$), the jet should reach this point at around $10^{11} - 10^{13}$ cm [62]. Moreover the ultra-relativistic Doppler effect would beam the radiation inside an angle $1/\Gamma$ which is usually rather smaller than the jet aperture angle, this sets the position for the radiation in a range of radii between $c\delta t - 2\Gamma^2 c\delta t$, where δt is the typical observed radiation timescale, which could depend by the central engine activity. At the end of the day, a typical jet should become transparent to the prompt gamma-ray emissions between $10^{12} - 10^{14}$ cm [48, 63].

Here, two main mechanisms may explain the origin of the radiation and constraint the emis-

sion site.

- Photospheric emission: In the assumption of a relativistic, homogeneous, fireball the radiation is entirely due to the early thermalization during the opaque stages of the jet ($\tau > 1$). This would be supported by the observed distribution of the peak energy at around 10 MeV [63]. However, before reaching the photosphere and escape, the radiation blackbody is modified by the heat provided by dissipation processes, the obtained profile is then able to resemble the observed Band function. [63].
- Internal shock emission: If a structured jet is assumed the homogeneous hypothesis doesn't hold anymore, hence the emission site should be more distant than the photospheric radius. In this case inhomogeneous regions could form due to dissipation processes, like magnetic fields instabilities or internal collisions, and would travel inside the jet with different lorentz factors. This could lead to the formation of local boosted zones, a sort of 'jet inside the jet' [48]. Eventually the fastest mini-jets would reach the slowest regions raising internal shocks which could break out as $\gamma - ray$ emission.

2.1.2 Afterglow

With afterglow is indicated the ensemble of signals immediately following the prompt emission. While the afterglow phase was predicted early on in the GRBs research history, its discovery comes only after the *Swift* telescope operations onset. Thanks to its fast capability to pin-point the source it was possible to locate a GRBs trigger and observe an extended fading signal.

The afterglow is a multi-wavelength phenomena, it can be observed starting from the X-ray all down to the radio band [64]. This is intrinsically related with the process that produces the afterglow

In the relativistic jet scenario, the incredibly fast fireball carrying the central engine's energy will eventually encounter the low-density circumburst medium. The latter will brake the outflow causing its compression which will raise both strong *forward shocks* which penetrates into the medium and *reverse shocks* which will penetrate into the jet instead. Together they are referred to as *external shocks* (see Fig 2.3) and are the cause of the particles acceleration inside the jet, which in turn will trigger the broad-band, non-thermal synchrotron emission observed in the spectra. Moreover, the acceleration is usually strong enough to allow for Inverse Compton event (then the process would take the name of *Synchrotron self-Compton, or SSC*) which boosts photons in the high energy regions, likely producing the observed extra non-thermal power law. Later, as the jet is slowed down, the strength of shocks decreases and the radiation fades at lower wavelengths [48].

In general it seems that the afterglow luminosity is fainter for SGRBs respect to the long one. This could either suggest less energy involved or a less density medium surrounding the burst site [49].

It should be noticed that both the afterglow spectrum and lightcurve are not perfect broken power law but they may present some features, such as plateaus and flares, which could be associated to activity from the central engine. Hence the overall radiation profile should be taken as the sum of the external shocks contribution with the internal late-activity. [49].

The afterglow lightcurve allows to constrain some information on the energy of the burst, the surrounding environment and on the jet opening angle, which is estimated to be in average $\theta_j \sim 10 - 15°$. The canonical and integral GRBs afterglow lightcurve is composed by five distinct contributions which can have different physical origins. They are summarized in Fig 2.3. Most of the observed events can be decomposed into a combination of at least some of these components [48]:

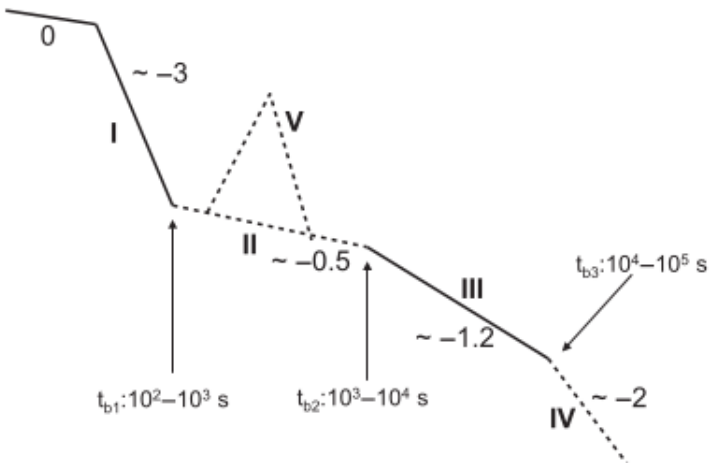

Figure 2.3: This images sketches the five different afterglow lightcurve's components. See text for description. Images taken from [48]

1. Steep decay phase: This is the very initial phase of the afterglow and it's characterized by a steep power-law decay with index ranging from $\sim$ -3 up to -10 s , often it's considered the tail of the prompt event extended emission (if present). For this reason it's not crystal clear what should be the origin of this contribution, it could either come from internal shocks central engine activity related, or be already raised by the synchrotron external radiation. The simplest explanation comes from the so called *curvature effect* assuming an immediate stops of the central energy injection, starting from the line of sight of an observer and moving at higher and higher latitudes, the radiation should arrive at the detector at progressively later times [65][66].

2. Shallow decay phase (Plateau): The first evidence of a distinctively different behaviour between the afterglow and the prompt emission lightcurves coincide with the shallow decay. Usually this phase yields a power-law with slope between ~ 0 (called *plateau*) and ~ -0.7 [48].

   The shallow decay profile is in well agreement with the forward shock process, however in order to maintain a plateau the fireball should be continuously powered by the central engine. This, again, suggests some kind of late-activity such as magnetic processes (long-lived magnetar scenario) or fall-back material accretion (collapse scenario). Sometimes an abruptly decrease may follow a plateau [67] this doesn't coincide with the standard synchrotron emission, hence in these cases an internal shock scenario (due to dissipation processes) at the origin of the plateau should be assumed.

3. Normal decay phase: After the plateau phase the slope increases its steepness (around $\sim$ 1), perfectly coinciding with the standard external forward shock model.

4. Post-jet-break phase: The following segment of lightcurve usually decrease the slope up to ~ -2 or even less. This is again in agreement with the normal forward shock scenario when inside the *jet break* regime. The jet break is reached when the lorentz factor is slowed down at the point in which the radiation beaming angle $\sim 1/\Gamma$ is wider than the jet opening angle causing loss of energy from the relativistic cone [48].

5. X-ray Flares: In many cases GRBs present some sharp and hard peaks super imposed on the decaying and softer background. They are called *flares* and usually lie in the X-ray, early γ range. A single GRB signal may present multiple flares, usually localized at the earlier times, their overall fluency can get to the $\sim 1\%$ of the prompt flux. These

characteristics suggest a different origin with respect to the background, resembling instead more similarities with the prompt emission features. Most likely they are powered in the same way by the central engine and then they are delayed by some phenomena like a retarded outflow ejection [68].

Summing up all the afterglow properties, given the hints on its similarities with some prompt emission features (x-ray flares and plateaus), the idea of a long-lived central engine is being more and more accredited. Recently works have estimated an overall burst duration (measured up to the end of the last observed flare) of hundreds of seconds for most of the case. Remarkably, about the 10 % should be longer than $10^4 s$ [69]

2.2 Jet Launching Mechanism

The information retrieved by SGRB observations lead to the conclusion of an ultra-relativistic jet as the site of such emission. In the previous Chapter it's stated that, according to literature, the favourite progenitors for SGRBs are the BNS merger, hence the link between these two events should be discussed.

In order to be in agreement with GRBs spectra and lightcurve information, a central engine should be able to power an energy of the order $E_{\gamma,iso} \sim 10^{49} - 10^{51}$ erg inside a collimated outflow propagating with a lorentz factor of at least $\Gamma > 100$. To achieve this, a very small amount of baryon loading, hence a 'clean' jet, should be expected.

Moreover the engine should release such amount of energy in a very small amount of time yielding highly variability, it should be also able to restart at later times (after about $\sim 10^2 - 10^4 s$) to produce the observed X-ray flares and plateaus.

The principal scenarios for the formation of an ultrarelativistic jet powering a SGRBs correspond to the possible remnant of a BNS merger: either a hyper accreting Black Hole or a very fast-spinning ('millisecond') magnetar.

2.2.1 Black Hole engine

At the date of writing the most accredited central engine is represented by the accretion around the stellar-mass BH produced as a consequence of the BNS merger remnant's collapse. When the horizon is formed most of the matter inside the first hundreds of kilometers gets sucked into the BH while the rest starts to be accreted into an axisymmetric, toroidal shape. This allows for the formation of relatively empty polar regions which could act as natural site for the jet launching.

In order to power a GRB the BH should be able to accrete material quite fast:

$$L_{GRB} = \xi \dot{M} c^2 = 1.8 \times 10^{51} ergs^{-1} \xi_{-3} \left(\frac{\dot{M}}{1 M_\odot s^{-1}} \right)$$

Where ξ is the efficiency of the process. It turns out that the adequate accretion rate should lie around $0.1 - 1 M_\odot / s$ [48].

This value is quite elevate, hence the definition of *Hyper-accreting Black hole*. Such process is capable to strongly increase the temperature of the inner region of the disk, allowing for electron capture processes to take place with the consequent production of neutrinos winds which in the end will cool out the disk. Moreover, the material's accretion will deposit onto the the central BH a large fraction of angular momentum, this would induce a fast spin which in turn will favour the accretion rate in a runaway fashion.

At this point two processes represent the main candidates for the jet ejection:

Neutrino annihilation

Pairs of neutrinos and anti-neutrinos inside the cooling flow will end up annihilating producing electron-positron pairs which could strip baryon matter from the disk. This process can in principle be able to power a broad and homogeneous jet which would be collimated by the interaction with the surrounding matter, channeling it in the relatively free polar regions. The power required to drive this mechanism depends directly on the accretion rate and can be formulated as:

$$\dot{E}_{\nu\nu} = 1.1 \times 10^{52} erg/s \left(\frac{M}{M_\odot}\right)^{-3/2} \left(\frac{\dot{M}}{M_\odot/s}\right)^{9/4} \tag{2.1}$$

(see [70])

Simulations result [71] shows that even if if the neutrino annihilation could in principle launch a $\Gamma > 100$ jet, most of its energy would be lost by drilling through the surrounding envelope which turns out to be still too baryon polluted to allow for an ultra-relativistic jet to successfully break out. Thus, while this process could in principle provide a non-negligible contribution, some other magnetohydrodynamic process should be considered as well.

Blandford-Znajek mechanism

When a BH is fast spinning, for particular configurations of its magnetic fields, it can be able to drain its rotational energy and use it to power a self-collimated, Poynting flux-driven jet. The required structure should allow for some magnetic field lines to be open, connected to some far astrophysical load see Fig 2.4. If this happens then the BH spin eventually twists the field lines exerting a torque which in turn slows it down, the energy lost is then powered outward along the open field lines, this is called Blandford-Znajek (BZ) mechanism [72].

This scenario is possible in the context of GRBs jets if:

$$\dot{E}_{BZ} = 1.7 \times 10^{50} erg/s a_\star^2 \left(\frac{M}{M_\odot}\right)^2 B_{15}^2 F(a_\star) \tag{2.2}$$

Where $a_\star = \frac{Jc}{GMc^2}$ is the spin parameter (J is the angular momentum) and F is a spin-dependent function. [3, 72]

The BZ process is directly dependent on the strength of the magnetic field and on its rotational energy, it has been shown [73] that it would be more efficient as $a_\star$ is closer to unity, this means that the jet is directly powered by the BH spin rather than its accretion.

The BZ mechanism doesn't exclude the neutrino-annihilation which indeed can contribute in the jet launching. However, the strong magnetic fields required for the process to work will block protons from their penetration into the outflow, hence yielding a much baryon clean jet which in turn should be light enough to reach the observed terminal lorentz factor.

According to recent results in GRMHD simulations ([74, 75] for example) there is still no direct observation of an ultrarelativistic jet production. However the clues for the emerging magnetic field structure and the creation of low-density funnels along the rotation axis suggest that the fast spinning, accreting, BH scenario is the most viable viable one to explain SGRBs.

Nevertheless, it still presents some challenges, in particular the main difficulties concern the interpretation of the observed plateaus and x-ray flares.

2.2.2 Magnetar engine

One of the possible, metastable, remnant of a BNS merger is a supramassive (or hypermassive) NS. The enhanced magnetic fields (see Chapter 1, Section 3) involved during the merger and

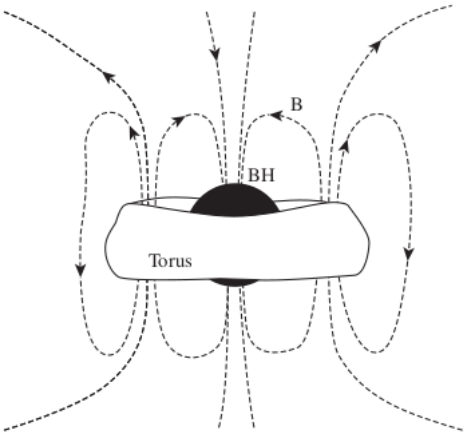

(a) BH magnetic open configuration

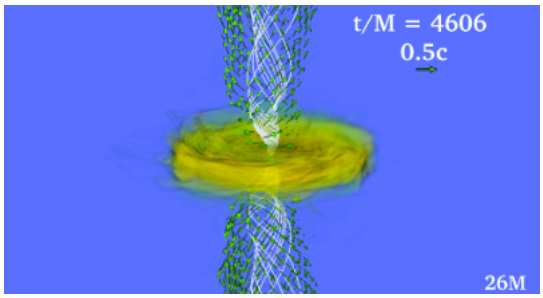

(b) Simulated emerging outflow

Figure 2.4: *left* Sketch of possible magnetic field open configurations which allows BZ mechanism. Image taken from [48]. *right* The result of full GRMHD simulation of a BNS merger with collapse into an accreting BH. An emerging outflow along the spin axis, in the Poynting flux direction, is observed. Image adapted from [74]

post-merger phases can lead to extra-magnetization on the surface of the resulting NS up to $B \sim 10^{14} - 10^{15}$ G. This is what it's usually known in literature as *magnetar* [76]. One of the critical parameter describing a NS is its spin, the more common magnetars rotate with a period P of the order of ten seconds, however in the more extreme situations a magnetar can end up spinning with a period of order $\sim O(1\text{ ms})$, these are called *milliseconds magnetar* and they can in principle provide an explanation for GRBs.

The main mechanism through which a magnetar can emit such powerful ejecta is the *magnetic spin down*, this in general allows for a sufficient energy budget as:

$$E_{rot} \approx \frac{1}{2} I \Omega^2 \approx (2.2 \times 10^{52} erg) \left(\frac{M}{1.4 M_\odot} R_{cm}^6 P_{0,-3}^{-2} \right) \tag{2.3}$$

Where I is the inertia moment ($\approx 10^{45}$ gcm^2 for a NS of mass $1.4 M_\odot$ and radius 10^6 cm), Ω is the rotational velocity and P_0 is the initial spin's period [48].

Notice how the total energy budget depends only on I and P_0 while the strength of the magnetic field accounts only for the duration of the spin down since it is driven by the magnetic dipole radiation:

$$\dot{E} = I \Omega \dot{\Omega} = -\frac{B^2 R^6 \Omega^4}{6c^3} \tag{2.4}$$

yielding an initial spin-down luminosity:

$$L_0 = \frac{B^2 R^6 \Omega^4}{6c^3} \approx 1.0 \times 10^{49} erg/s B_{15}^2 P_{0,-3}^{-4} R_6^6 \tag{2.5}$$

which will decrease in time as the spin energy is consumed [77].

This treatment holds only in the assumption of a rigid rotating supramassive NS however it shows that in principle a magnetar remnant has the right parameters to be claimed as a SGRB central engine. Furthermore, a spin down radiation would be continuous and long-lasting, hence providing a natural energy injection which could explain the internal features of the afterglow lightcurve. The magnetar scenario could even explain the steep decay following the plateau emission invoking the sudden collapse to a BH once the spin has been lowered enough [48, 69].

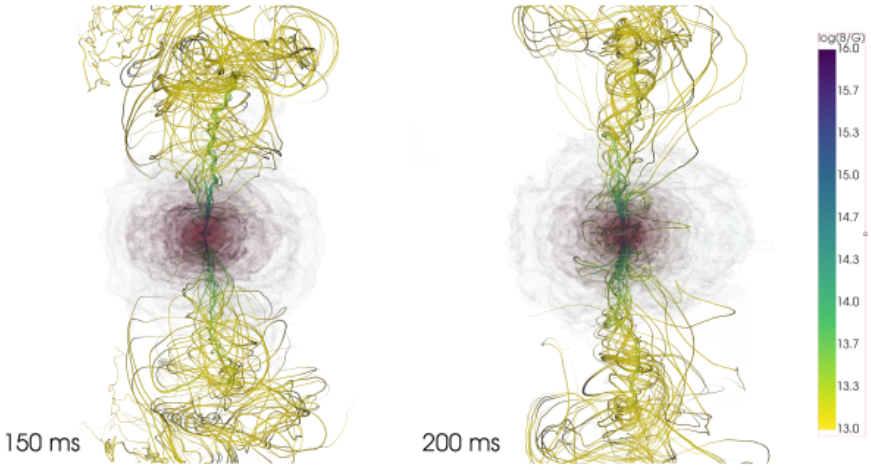

Figure 2.5: The images shows the result of one of the longest full GRMHD simulations in 3D. With the right choice of a the initial magnetic field an helical structure is formed in the polar regions, allowing for collimated outflow to breakout. The color bar indicates magnetic field strength while in the center isodensity surfaces are shown. The scale covers up to 2700 km vertically. Images taken from [38] and adapted from [30]

Nevertheless, the magnetar scenario finds many challenges in explaining the actual main, prompt emission. Realistic simulations [39] [30] have shown that a collimated outflow can in principle emerge form at the polar regions of a metastable remnant, mostly powered by a specific, helical, magnetic configuration (see Fig 2.5). However this would be rather baryon-loaded reaching a lorentz factor no larger than unity, too slow to possibly claim a SGRB emission (also the creation of the necessary helical structure is not itself ubiquitous and always granted, see [38] and Fig 2.6).

For these reasons the most favoured mechanism for SGRB jet launching remains an hyper-accreting BH, possibly not prompt-collapsed but following a metastable NS remnant phase which, among other things, could justify the main contribution on the delay the EM signal has on the gravitational one.

2.2.3 Time-Reversal scenario

Recently an alternative and detailed scheme, attempting to coherently unify the BH and the magnetar contributions in order to explain the overall SGRBs observations, have been proposed by [78]. The so called *Time-Reversal scenario* assumes that the prompt emission and the X-ray afterglow corresponds to two distinct signal sources with the original feature that predicts the X-ray emission to be powered *before* the ultrarelativistic $\gamma - ray$ jet. The differences in the propagation of the two signals would then provide the observed lightcurves.

The phenomenology of the case unravels itself in in the following evolutionary phases (see Fig 2.7. See [78] for a detailed explanation):

1. Right after the merging, a deformed hypermassive NS sustained by its own differential rotation is formed. The remnant however has a mass lower than the limit required for a stable, uniform rotation. During this phase a strong, baryon-loaded, mass ejection is triggered by either neutrino cooling or magnetic-driven winds. The ejecta should be in the range $\dot{M} \sim 10^{-3} - 10^{-2} M_{\odot}/s$, propagating with a speed $\sim 0.1c$. This phase should last a time $\tau_{dr} \sim 0.1 - 10s$ which depends on the strength of the initial magnetic field.

2. After τ_{dr} the remnant settles as an uniformly rotating, supramassive, NS. At this stage

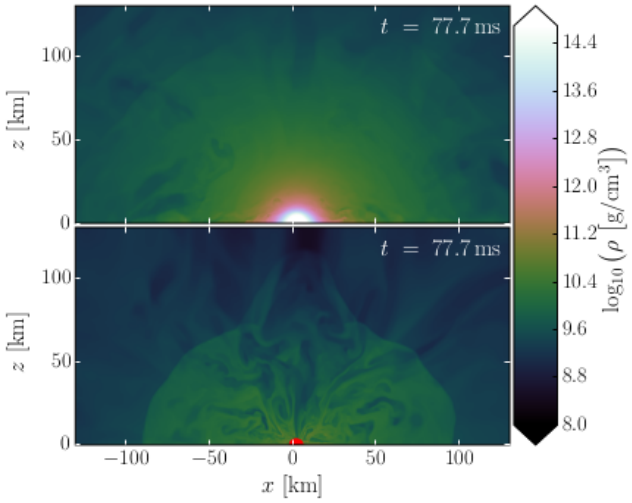

Figure 2.6: Meridional view of rest mass density of two different simulations with same initial data. *top:* long-lasted magnetized NS which has avoided collapse so far, the magnetic wind has had enough time to isotropically pollute the surrounding, preventing a jet to breakout. *Bottom:* BH case, the collapse allows for the cleaning of the surrounding regions, especially near the poles. This sets up an ideal site for jet launching. Image taken from [39]

the mass ejection is stopped and radiation is emitted due to the magnetic spin-down. As pointed out before, the spin-down timescale depends on the initial rotational period and on the surface's magnetic field: $\tau_{sd} \approx 2.7 \times 10^3 B_{15}^{-2} R_6^{-3} P_{0,-3}^2 s$. The emitted radiation has enough energy to yields a plasma of electron-positron pairs henceforth called *nebula*. The nebula is lifted behind the isotropic ejecta and starts comprising it while propagating outward. This will end up raising a strong shock which sweeps the material into a thin shell. The shocked matter will heat up and accelerate up to relativistic speeds, $v_{ej} \leq 0.8 - 0.9c$. If, at this stage, any radiation is able to escape the optically thick ejecta then a SGRB precursor may be seen.

3. After a time-scale τ_{coll} the remnant's rotation will have slowed down enough and it cannot prevent the collapse anymore. The supramassive NS will finally fall into a BH and the energy injection in the nebula is suppressed. Most of the surrounding matter will infall as well, forming an accretion disk and allowing for the ultrarelativistic jet launch outside the less dense polar regions. The collimated outflow will drill through the surrounding and break out yielding the prompt emission. Finally, after some delay, the ejecta shell will become optically transparent to the spin-down radiation allowing for the the long-lasted X-ray afterglow to emerge.

In order for this scenario to be realistic at least two conditions should be satisfied: the time required for the ejecta to become optically thin to the spin-down radiation should be higher than the sum of the time taken by remnant to emit the jet plus the time taken by the latter through breakout; the delay time of the spin-down radiation is assumed to explain the afterglow, hence it should last a similar amount of time, up to $10^2 - 10^5 s$.

The first condition is fulfilled by assuming a relativistic jet launched by the BH (as predicted by observations), while in [78] has been shown that for a rather broad range of reasonable parameters also the second condition is satisfied and the two timescales are compatible.

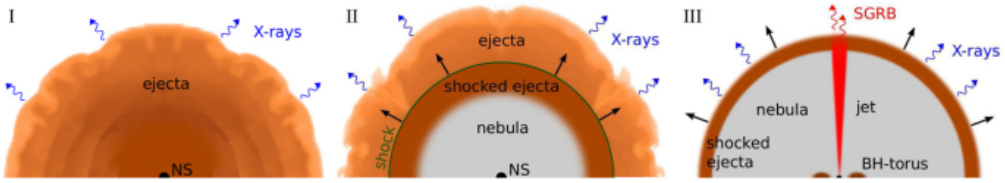

Figure 2.7: From left to right the evolutionary phases accounted in the time-reversal scenario are shown. See text for details. Image taken from [78]

2.3 Jet Structure and GRB 170817A

Getting the launching mechanism and the related role of the progenitors is just the beginning. In order to have a full, integrated, scenario describing the phenomena of a BNS merger up to the SGRB emission, the structure and the propagation properties of the ultrarelativistic jets have to be understood.

Reproducing analytically a realistic BNS merger ejecta can be quite a challenge. For this reason for many years in literature many simplified models were applied, in most of the cases they worked just fine. However, with the identification of GRB 170817A, the EM counterpart of GW170817, an improvement of the theoretical framework was required [79, 80, 81]. Nowadays exploiting the increasingly powerful and modern numerical resources, a number of detailed simulations on relativistic jets propagation into the surrounding medium have been accomplished [82, 83, 84]. About all of them predict the ejection of a *structured jet* in which the properties profiles scale with the angle of view.

2.3.1 Structure and Propagation

The way in which a jet interacts with the circumburst environment determines its final structure and helps to constrain the emission features of the observed SGRB.

Indeed the distribution and the amount of the material filling the environment depends on the final jet progenitor, however another important parameter which can shape the ejecta is the delay time between the merger and the jet launch. An early jet would encounter less matter in the polar region hence it would end up being more disperse with a wider opening angle. As the delay increases the isotropic outflow would increasingly pollute the surroundings, providing an higher jet collimation. Finally, if the launch is too delayed then the polar density could potentially be too heavy ending up chocking the jet, this scenario is known as 'failed (or chocked) jet' [85].

Fig 2.8a shows the analytical model adopted by [79] to reproduce a relativistic jet, whereas in Fig 2.8b a result from the simulations carried in [85] is presented for comparison.

An incipient jet is well represented by a conical outflow which moves radially outwards inside an opening angle $\theta_{j,core} \propto \frac{1}{\Gamma}$ (where Γ is the terminal lorentz factor) which is usually assumed to be in the range $\sim 10°$ -$30°$ [86]. As the jet starts to propagate out, it will eventually bump against the surrounding, slower, ambient material, this will produce shocks. The one propagating ahead of the jet and inside the external medium is called *forward shock*, whereas the one propagating backward, inside the jet material, is refer to as *reverse shock*. The region within the two shocks is what is called *head* of the jet. The head velocity increases up to when the hydrodynamical equilibrium between the ram pressure of the jet and the weight of the ambient material is reached, hence the terminal lorentz factor will strongly depend on the surrounding density. While propagating the jet sweeps aside and pushes the ambient material into an over-pressured zone called *cocoon*. Usually the cocoon is reproduced as a cylindrical region which envelops the jet from its base all up to the top. While the cocoon expands sideways into the ambient medium, pushed by the relativistic outflow, it in turn will exert a confining pressure which increases as the amount of material casted in it grows further. Eventually the cocoon pressure will overcome the

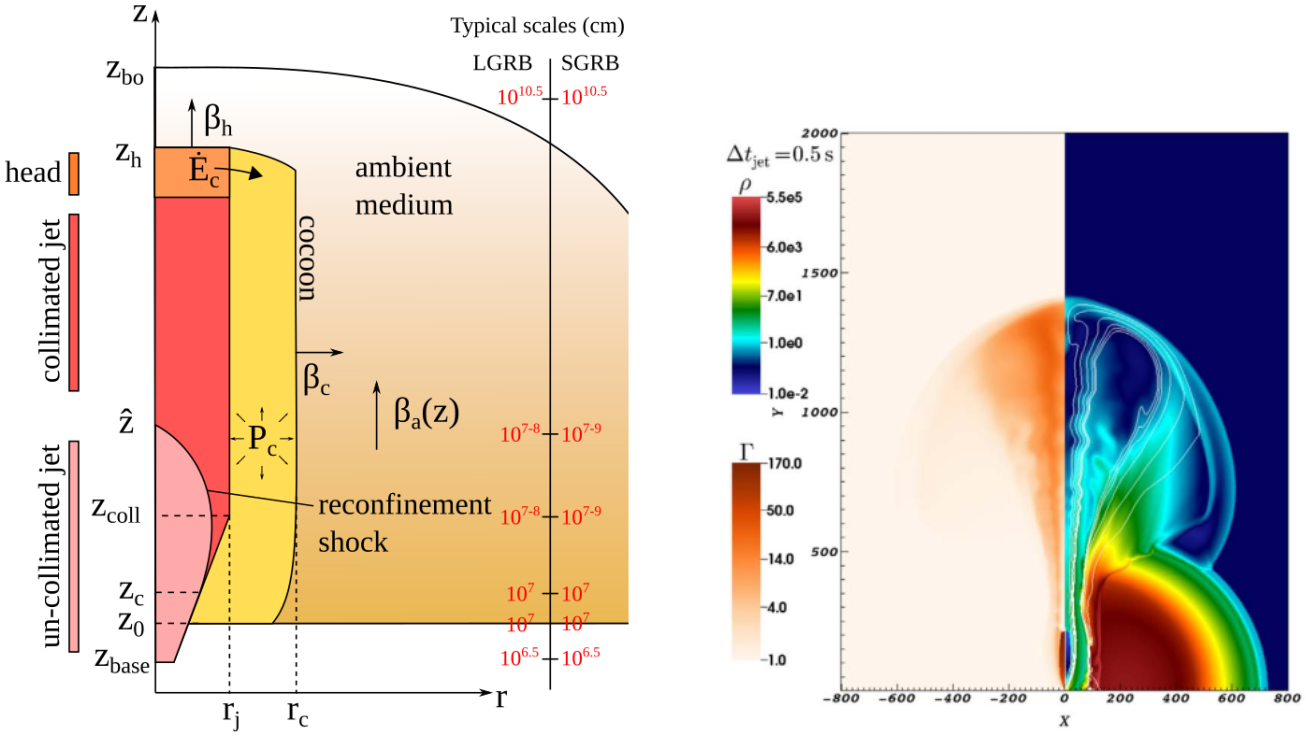

(a) Analytical jet propagation model

(b) 2D map of a simulated successful jet

Figure 2.8: *Left:* Sketch of the components of a general jet propagation model. Images taken from [79]. The plots shows the height Z against the radii from the central origin r. Typical scales (in cm) are highlighted in red and refer to an average on various progenitors and jet emission parameters. *Right:* 2D density and lorentz factor maps of a simulated jet breaking out successfully. The jet was launched with a delay of 0.5s with respect to the merger. Result obtained in [85]

jet thermal pressure, raising the so called *reconfinement shock* which usually takes a parabolic shape [79]. Such shock affects the material providing collimation causing the jet profile to be narrow with a steep fall immediately outside the core, whereas, at the base, where the fast jet injection isn't influenced by the reconfinement shock yet, the profile assumes a quasi-Gaussian shape [79]. The jet propagation will continue up the the eventual *breakout*. Indeed, if the delay in the jet launch is small enough (up to few seconds [85]) then the outflow will be able to exit from the ambient medium and start to freely expand into the Interstellar Medium (ISM), as it turns out from numerical simulations the successful jet breakout represents the majority of the cases [87]. At the breakout radius the cocoon material is free to expand as well, causing a pressure drop and stopping the side reconfinement shock. This will inhibit the collimation effect causing a spread of the jet material which will affect the opening angle. As the pressure decrease exponentially in time, the final jet opening angle will increase in the same way until it recovers its initial value [88]. After the breakout, jet and cocoon merge into a single structure called 'structured jet', then it is finally free to expand at homologous (i.e. ballistic) proportions.

2.3.2 Observing GRB 170817A

17 August of 2017 was a remarkable day for astrophysicists. Almost at the same time the gravitational wave signal GW170817 and the gamma-ray trigger GRB 170817A were independently detected by respectively the Advanced LIGO and Virgo interferometers and the *Fermi* Gamma-ray Burst monitor (GBM) [89][90]. The occurring probability of a simultaneous, non-correlated, observation was 5×10^{-8}, therefore this event strongly confirmed the close relation between BNS merger and SGRB emission [57]. The relative delay between the 2 signal was measured to be of $\approx 1.7s$. This measure allowed to provide new constraints on the gravitational waves speed and on the Lorentz invariance violation [90].

With the detection of GW170817, an immediate follow up campaign in EM bands was started, this led to the discovery of NGC 4993 as the host galaxy for the merger event [90]. Its distance was evaluated to be around 42.9 ± 3.2 Mpc [57]. This means that GRB 170817A is the closest short gamma-ray burst ever observed (by up to two order of magnitude with respect to canonical bursts)

The GBM detection was characterized by a two components signal, the first one which triggered the detector and lasted about one and half second, was spectrally harder and shorter than the second contribution, which in turn was longer (few seconds) and weaker [91]. The analysis of the signal revealed that the first and higher components is well fitted by a power law with a high energy exponential cutoff (so called 'Comptonized function') which peaks at $E_{peak} = 185 \pm 62$ keV. The tail emission instead is best fit by a blackbody (BB) spectrum with temperature $k_B T = 10.3 \pm 1.5$ keV, this is little consistent with the canonical SGRBs lightcurves with extended emission however the signal was rather weak and near to the detector limit [57, 91].

Measuring the intrinsic energy spectrum and knowing the distance from the signal it was possible to derive the luminosity of the event. The equivalent isotropic energy of the gamma-ray emission was estimated to be: $E_{iso} = (3.1 \pm 0.)7 \times 10^{46}$ erg/s hence the associated isotropic luminosity holds: $L_{iso} = (1.6 \pm 0.6) \times 10^{47}$ erg/s in the 1 keV-10MeV band. Despite the closeness, when comparing these values with the canonical SGRB parameters, it turns out that the event of August 2017 was rather subluminal and less energetic of actually two to six order of magnitudes, hence it's sometimes categorized as low-luminosity SGRB [92].

The GRB 170817A peculiarities didn't stop with the the prompt emission characteristics. Despite an intense observational campaign, the X-ray afterglow wasn't detected before than $\sim$ 9 days from the *Fermi* trigger time [93]. Moreover the afterglow flux was found to be rather faint, $\sim 2.7 \times 10^{-15}$ erg/s [93] and not fading (as expected in a canonical SGRB scenario) but instead presenting an increasing profile which peaked after $\sim$ 100 days [94]. A similar brightening behaviour was found in the radio band after $\sim$ 16 days from trigger time [95]. In particular,

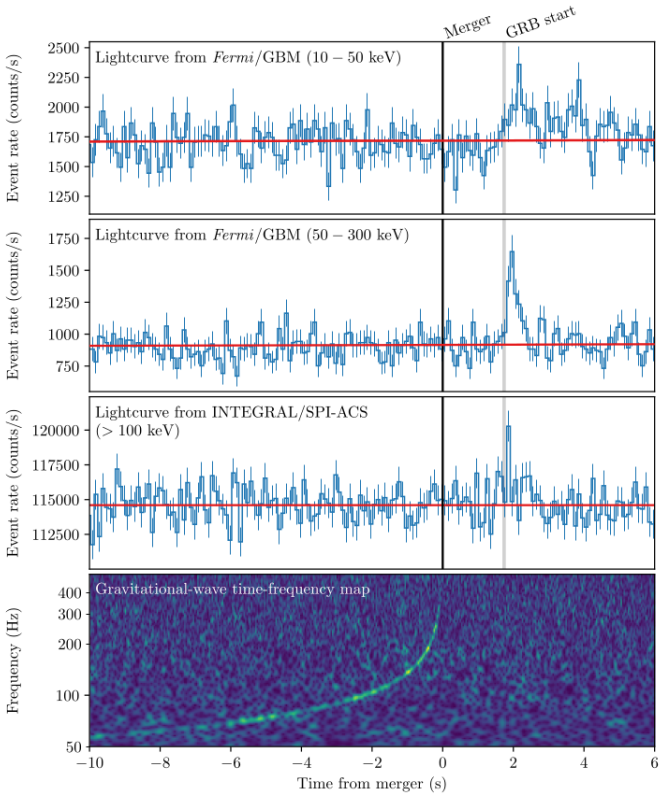

Figure 2.9: Multi-Messanger detection of GRB 170817A and GW170817A. GRB data are presented in different energy bands (hence different instruments), the red line evidences the background. the origin of time is referenced to the GW detection. Image taken from [57]

latest observations, carried with the VLBI observatory, showed the presence of an apparent superluminar motion, with velocity $\beta \sim 4.1$, of the radio signal [96], this finally proved that the event was been produced by a relativistic outflow (hence ruling out isotropic emission models such as [97]) and was observed off-axis. The afterglow observation provides constraints of the angle between the jet propagation and the detector position at $\approx 10°$-$30°$. Despite the afterglow faintness, an ultra-luminous kilonova, AT2017gfo, was detected in the bands from the IR to the UV [98, 99]. The first observations were successful already after 0.5 days from the prompt emission, spectroscopy data showed that the kilonova emission dominated the flux contribution up to the soft X-rays, however the UV luminosity was anomalously bright (hence been called *macronova*), suggesting an additional contribution from the independent afterglow emission [100].

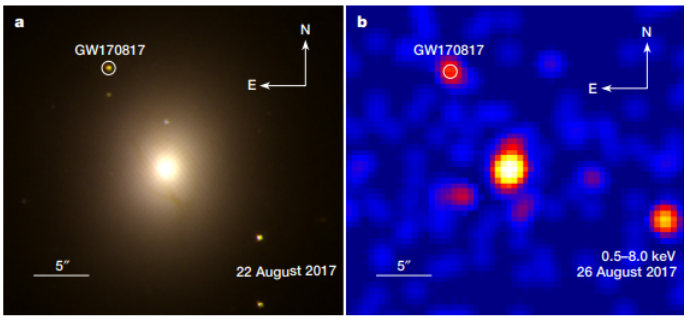

Figure 2.10: Multi-band observations of GW170817. **a:** HST observation, **b:** Chandra observation. At these energies bands the signal comes from the ejected macronova. Image taken from [93]

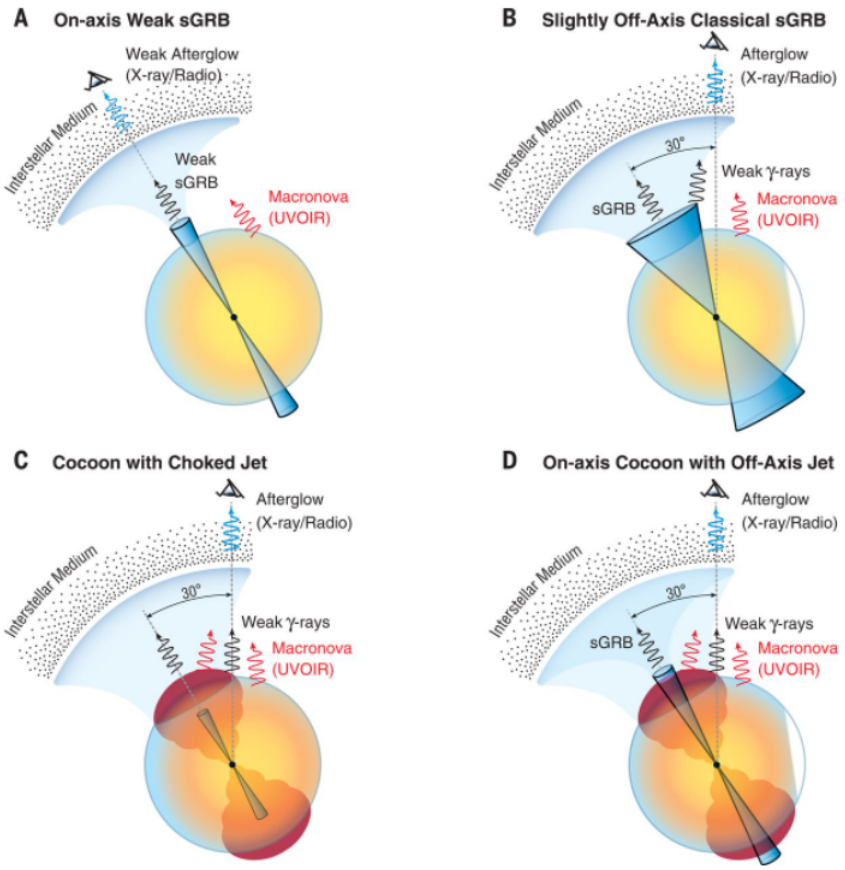

Figure 2.11: Schematics of the four main different phenomenological scenarios for GRB 170817A. See discussion in text. Image taken from [101]

2.3.3 Phenomenology

Available data suggested a peculiar nature for GRB 170817A. Any proposed model attempting to explain the origin behind the signal was required to be simultaneously consistent with all the EM counterparts (prompt emission, afterglow, and kilonova) at the various frequency bands.

Initially, there were four main proposed scenarios, represented in Fig 2.10 and hereafter summarized

A: Weak on-axis SGRB According to this scenario GRB 170817A is emitted from a classical, even if weak and narrow, relativistic jet with aperture $\theta \sim 10°$, Lorentz factor $\Gamma = O(100)$ and observed along the jet propagation direction. However, in order to be so faint but still able to breakout, such jet should encounter less than $O(10^{-6} M_{\odot})$ while propagating, which is in discordance with the amount of material required to power the kilonova, estimated to be at least of order $0.05 M_{\odot}$ [101]. Moreover, the lack of the immediate fading behaviour in the X-ray afterglow and the presence of apparent superluminal motion in the radio band completely ruled out this scenario.

B: Off-Axis Classical SGRB According to afterglow observations, this scenario proposes that the August 2017 event could be emitted by a less powerful, side wing of an ordinary ultrarelativistic jet propagating off-axis with respect to the observer direction. Following this description, many authors also proposed a 'quasi-universality' model for SGRBs, where differences in observations would be explained just with different observation angles [79]. The off-axis

jet well explains the brightening behaviour of the afterglow: if the jet isn't directed toward the observer then the initial emitted synchrotron radiation wouldn't be accessible; as the head is braked by its interaction with the ISM, it would start to spread aside finally intercepting the Earth line of sight. However, off-axis models predict an increase of the luminosity lasting even several hundreds of days, while in this case the afterglow started to decline after only ~ 100 days [100]. Moreover, the sharp drop in the detected prompt emission would suggest, according to this model, that the off-axis angle should be relatively small, $\leq 8°$, [101], but such slight orientation would be in contrast with other observed constraints. In conclusion, the classical SGRB scenario is to be considered very unlikely.

The conclusion so far is that GRB 170817A is not an ordinary burst signal and may be originated through a different mechanism with respect more canonical ones. Observations conclude that a beamed, relativistic outflow is always associated to the emission of a gamma-ray burst [93]; however, scenarios in which the emission site is a wide-angle mildly relativistic outflow that propagates in the observer's direction are also possible.

The cocoon surrounding the incipient jet is a highly energetic, hot region propagating with lorentz factors of order O(1) over a wide region $\sim 40°$ [101]. The cocoon expands radially up to the breakout radius, there the interaction with the jet could arise a strong forward shock allowing for the dissipation of its energy in the form of gamma-ray radiation. The likelihood of this scenario was tested by some simulations [92, 101, 102], in particular assuming two different criteria:

C: Cocoon with Chocked jet Assuming a delayed ejection, a wide angle jet ($\theta \sim 30°$) would end up being braked and chocked by the surrounding BNS ambient medium, however the cocoon formed during the jet propagation would still be able to breakout and emit. In this scenario the X-ray and radio signal would be produced by the forward shock generated by the cocoon interaction with the circum-merger environment. However, further analysis showed that radio data aren't compatible with a uniform expanding cocoon, favoring instead the propagation of an ultrarelativistic and collimated outflow into the ISM [87].

D: On-axis cocoon with Off-axis jet The last scenario is similar to the former with the important difference that now a successful jet is predicted. Indeed, if the outflow is narrow enough ($\theta \sim 10°$) then the jet would be able to drill through the ejecta and breakout as well. In this case the weak prompt emission would still be produced by the forward shock breakout of the cocoon whereas the X-ray and late afterglow would be jet dominated, producing the expected brightening profile in agreement with observations, as predicted already in [80], one of the first (if not the very first) model comparison with prompt and afterglow data based on a relativistic HD jet simulation, and later confirmed by VLBI observations [87, 96]. Thus, the combined successful jet-cocoon breakout scenario is consistent with the multi-band properties of GRB 170817A without giving up the structured jet model.

Currently the last scenario is the widely accepted one although only further work, both on the theoretical and observational levels, could lead to a complete insight of the phenomena.

In this Thesis, the scenario D is considered. The aim is to provide a first, self-consistent modeling of the cocoon breakout emission as a possible candidate for an observed prompt signal. Here only the thermal contribution to the radiation will be considered, leaving the non-thermal processes for future works.

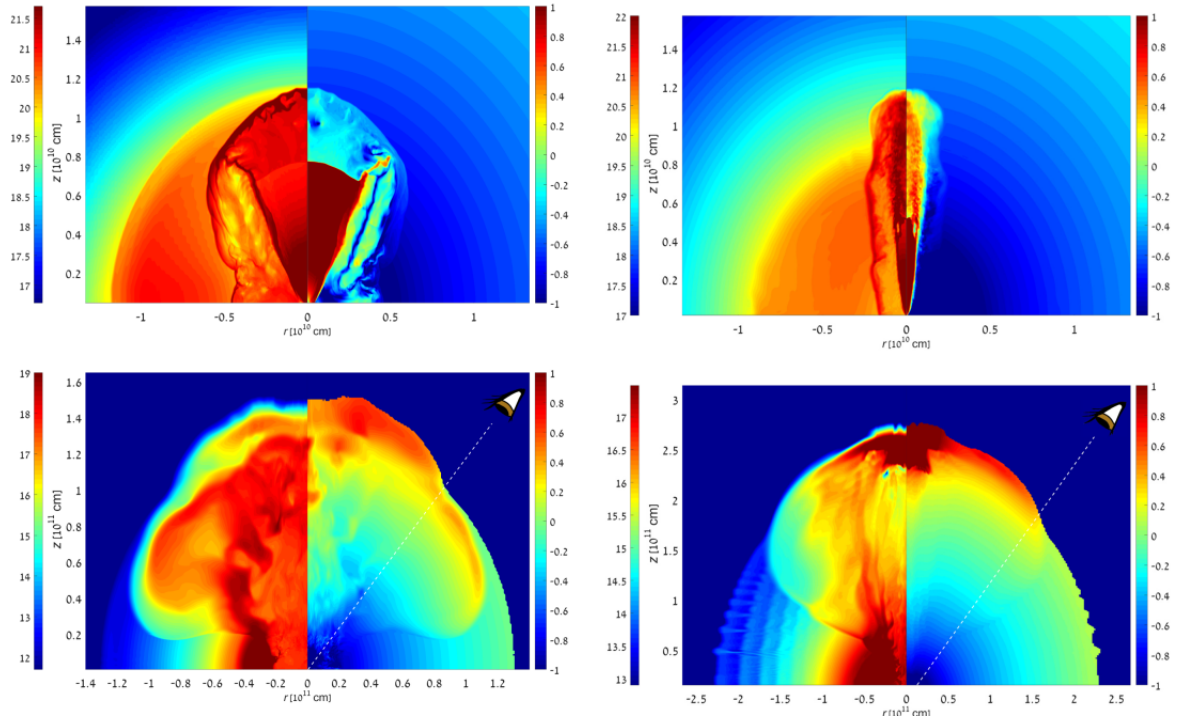

(a) Chocked Jet (b) Successful Jet

Figure 2.12: Logarithmic map of density (left for both) and four velocities (right for both). In both cases the bottom figure is a snapshot taken at the breakout radius. *Left:* Chocked jet, despite the outflow isn't able to break out a quasi-spherically forward shock is produced. *Right:* A narrower, well collimated outflow is able to drill through all the ejecta and break free. These results are obtained in [92].

Chapter 3

Physical Framework

In order to study a physical system the very first step is always to establish the theoretical framework within which the system is going to be represented. In astrophysics, and in particular in the study of GRBs and relativistic jets, the scales involved are big enough to require the fluidodynamical (or hydrodynamical, HD) treatment. A fluid is modeled as a large scale system composed by elements which are basically homogeneous ensembles of microscopical particles. In this way it is possible to avoid to follow the motion of each of them (this would be rather impracticable) focusing on the description of the neighbouring fluid elements dynamics thus providing a bridge between the microscopic and the macroscopic properties of the system. Whenever either all the constituents or the bulk of the fluid itself move at speed comparable to the speed of light, relativistic corrections are required. Jets associated to SGRB emission are supposed to travel with a bulk lorentz factor $\Gamma \sim O(100)$, or at the very least of order $\Gamma \sim O(1)$ if considering the slower cocoon as the possible site for the emission, therefore a relativistic treatment cannot be avoided. Whereas in the the Special relativity treatment spacetime is considered to be flat, further corrections are provided by the application of General relativity when in presence of large masses which would raise non-negligible curvature effects. However in this work jets are treated from the breakout radius, which is typically placed at $\sim 10^{11}$cm from the central compact object, and beyond. As a result the general relativistic corrections can be safely ignored. The discussion about magnetic fields is less trivial. Indeed magnetic effects take place within the jet and can in principle raise shocks and emit radiation. However, due to dissipation mechanisms, the outflow is expected to quickly reach the equipartition. In general, especially at larger times from its emission, the jet should be mostly hydrodynamically-driven allowing for the magnetic field contribution to be neglected, at least in a first approximation.

The aim of this work is to include, for the first time into a realistic jet simulation, the numerical treatment for the radiation transport. To perform this, the best trade-off between accuracy and numerical complexity is represented by the Radiation Relativistic Hydrodynamic (RAD-RHD) formalism.

In this Chapter, in order to set the ground for the numerical discretization, the basic principles behind the Rad-RHD formalism are quickly reviewed. In Section 3.1 the RHD equations are presented in their conservative formulation. In Section 3.2 the radiation transport is going to be discussed leading to Section 3.3 in which the two ingredients can be finally merged together to derive the Rad-RHD equations. It will be mostly followed the treatments developed in [25] and [103]. **A note on the notation**: Typical relativistic treatments use natural units and consider $c = 1$, this will also be the general formulation applied in the Thesis. However, in some paragraphs, using an explicit notation for the c factors helps the understanding of the physical quantities at play. This is the case of subsections 3.1.1, 3.2.1, 3.2.2.

3.1 Relativistic HD

The aim of this section is to present the RHD equations in the form useful to be discretized for numerical applications (see Chapter 4).

Start by considering the microscopic properties of a fluid, this will allow the derivation of a consistent behaviour which agrees both with the large and small scale problems.

3.1.1 Kinetic Theory

The minimal constituent of a fluid is called *element*, it can be thought as the largest volume in the 3-dimensional phase space d^3xd^3p which collects an ensemble of homogeneous, indistinguishable, particles with same mass m and which is still small enough to be considered as a 'macroparticle' with point-like behaviour in the limit of the continuum. Here x^μ is the 4-vector representing the spacetime coordinate whereas $p^\mu = mu^\mu = (p^0, p^i) = \gamma c(m, v^i)$ is the relativistic quadri-momentum since u^μ is the 4-velocity of the particles within the element and $\gamma = (1-(v/c)^2)^{-1/2}$ s the lorentz factor.

The fundamental quantity of the kinetic approach is the *distribution function* $f : f(\mathbf{x}, \mathbf{u})$ [1] which describes the probability, at each instant, to find a particle in the phase space elementary volume. From this definition is possible to compute the total number of particles in a given volume as: fdx^3dp^3 and the total number of particles N in the system as the integral of the previous quantity over the whole fluid:

$$N = \int_\Omega f d^3xd^3p, \qquad n = \int f d^3u \tag{3.1}$$

Where Ω is the total volume embedding the fluid while n is the particles number density

Now, in special relativity, quantities which measure the same in different, inertial, reference frames are called *Lorentz invariant* in the sense that they don't change under a lorentz transformation. The overall number of particles within a fluid element must share this property since it makes little sense that two different observers count a different number of finite items in a volume, hence:

$$fdx^3dp^3 = f'dx'^3dp'^3 \tag{3.2}$$

Where the primed (') quantities are referred to an observer O' which moves with some speed $\vec{v}$ with respect an observer O comoving with the particle.

It's possible to show that the product dx^3dp^3 is Lorentz invariant, then the distribution function f must be an invariant as well:

$$f(\mathbf{x}, \mathbf{u}) = f(\mathbf{x'}, \mathbf{u'}) \tag{3.3}$$

All systems tend naturally to a state of equilibrium, this is formalized through the definition of a *equilibrium distribution function* f_0 which is stationary (i.e time independent) and describes the thermodynamic properties of the system. Moreover, according to the kinetic theory, particles are subjected to external forces and internal interactions known as *collision*, the sum of these effects establishes the natural evolution of the particles distribution toward the equilibrium and its described by the *relativistic Boltzmann equation*:

$$\mathbf{p}\frac{\partial f}{\partial \mathbf{x}} + \frac{\partial(\mathbf{F}f)}{\partial \mathbf{p}} = \Pi(f) \tag{3.4}$$

[1] **Bold** notation is used to indicate a generic tensor

Where $\mathbf{F} = F^\mu$ is the 4-force which acts on the particle and Π represents the relativistic collision integral, it summarizes all the inter-particles effects which can change their wordlines (i.e their trajectories) and velocities [104].

The equilibrium distribution function which solve eq 3.4 allows the derivation of macroscopic properties starting from the microscopic scales. In fact, it's always possible to define an average, for any quantity ψ, with respect the distribution f:

$$< \psi >= \frac{1}{n} \int \psi f d^3u \tag{3.5}$$

The averaged quantities are the macroscopic correspondent to the (microscopic) particles properties and they are necessary to describe the fluid's global behaviour.

The fundamental quantities for a hydrodynamical treatment are the so called *collisionally invariants* since they are conserved during the collision within the particles. A generic quantity ψ is said to be collisionally invariant if it satisfies:

$$\int \Pi(f) \psi d^3u = 0 \tag{3.6}$$

In this way, by multiplying the Boltzmann equation to ψ and carrying the integral, the collision contribution vanishes and a *conservation transport equation* is retrieved. This result allows one to define a further quantity called *transport flux* which computes how much of ψ is transported, per unit time and area, along a generic direction. In the relativistic generalization the tensor $\mathbf{G} = \mathbf{G}(x^\mu, p^\mu)$ contains all the quantities assumed to be conserved during a collision, hence following the procedure above described it's found:

$$\int G^{\alpha_1 \dots \alpha_k} \left(p^\mu \frac{\partial f}{\partial p^\mu} + m F^\mu \frac{\partial f}{\partial p^\mu} \right) \frac{d^3p}{p^0} \tag{3.7}$$

Where $\frac{d^3p}{p^0} = \frac{mc^2 d^3u}{mc^2} = d^3u$ is the relativistic, invariant 3-volume element in the velocity space. Now, assuming that the 4-force vector is independent from the quadri-momentum, and rearranging the terms it's possible to derive the *relativistic conservation (or transport) equation*:

$$\frac{\partial}{\partial x^\mu} \int G^{\alpha_1 \dots \alpha_k} p^\mu f \frac{d^3p}{p^0} - \int \left(p^\mu \frac{\partial G^{\alpha_1 \dots \alpha_k}}{\partial x^\mu} + m F^\mu \frac{\partial G^{\alpha_1 \dots \alpha_k}}{\partial p^\mu} \right) f \frac{d^3p}{p^0} = 0 \tag{3.8}$$

This allows the direct derivation the conservation equations for all the momentum of the equilibrium distribution function, hence it is also called *relativistic momentum equations.*

In fact, it is possible to introduce the quantity:

$$\phi^{\mu \alpha_1 \dots \alpha_k}(\mathbf{G}) = \int G^{\alpha_1 \dots \alpha_k} p^\mu f \frac{d^3p}{p^0} \tag{3.9}$$

Where $G^{\alpha_1 \dots \alpha_k}$ are the contravariant components of $\mathbf{G}$. Φ contains the *relativistic transport fluxes* then, by selecting an order k, all the momentum can be computed.

By taking $k = 0$ one finds $\mathbf{G} = c\mathbf{1}$ ($\mathbf{1}$ is the identity tensor), hence from 3.9 the *first moment* of the distribution is found as:

$$N^\mu = c \int p^\mu f \frac{d^3p}{p^0} \tag{3.10}$$

This is called *number density current* and it is a 4-vector which components represent either:

- The number density :

$$N^0 = c \int f d^3p = cn \tag{3.11}$$

- The flux of particle number along the i-th spatial direction:

$$N^i = c \int p^i f \frac{d^3p}{p^0} = c^2 \int \gamma m v^i f \frac{d^3p}{E} = \int v^i f d^3p \tag{3.12}$$

Where the definition of relativistic energy has been used: $E = \gamma mc^2$, hence $p^0 = E/c$.

Thanks to the number density current is possible to compute the *rest-mass density current*:

$$J^\mu = mN^\mu = mc \int p^\mu f \frac{d^3p}{p^0} \tag{3.13}$$

Then substituting the first momenta in the transport equation one can directly derived the *continuity equation*

$$\frac{\partial J^\mu}{\partial x^\mu} = mc \frac{\partial}{\partial x^\mu} \int p^\mu f \frac{d^3p}{p^0} \tag{3.14}$$

Which describes the mass conservation within the fluid

In the same way, by setting k=1, $\mathbf{G} = G^\mu = cp^\mu$ and 3.9 provides the *second moment* of the distribution function also called *energy-momentum tensor* or *stress-energy tensor*:

$$T^{\mu\nu} = c \int p^\mu p^\nu f \frac{d^3p}{p^0} \tag{3.15}$$

This quantity essentially measures the flux of the μ-momentum along the ν direction (see Fig 3.1 for details). By writing 3.8 for the second moment of the distribution it's possible to derive the *conservation of energy and momentum equations*:

$$\frac{\partial T^{\mu\nu}}{\partial x^\mu} = mc \frac{\partial}{\partial x^\mu} \int p^\mu p^\nu f \frac{d^3}{p^0} = c \int m F^\nu \frac{d^3p}{p^0} \tag{3.16}$$

Both the rest-mass density current and the energy-momentum tensor represent fluxes of conserved quantities within the fluid. Thus it is possible to impose that outside the system domain, enclosed in a 3-surface Σ, every net flux vanishes, hence one can write:

$$\int_\Sigma J^\mu \hat{n_\mu} d^3x = 0 \tag{3.17}$$

$$\int_\Sigma T^{\mu\nu} \hat{n}_\mu d^3x = 0 \tag{3.18}$$

Where $\hat{n}_\mu$ is the versor normal to the surface.

Applying the Gauss divergence theorem it is possible to transform the surface integrals into volume ones:

$$\int_\Omega \nabla_\mu J^\mu d^4x = 0 \tag{3.19}$$

$$\int_\Omega \nabla_\mu T^{\mu\nu} d^4x = 0 \tag{3.20}$$

This results holds for any 4-volume Ω, so that it's straightforward to extract the *general relativistic hydrodynamic equations*:

$$\nabla_\mu J^\mu = 0 \tag{3.21}$$

$$\nabla_\mu T^{\mu\nu} = 0 \tag{3.22}$$

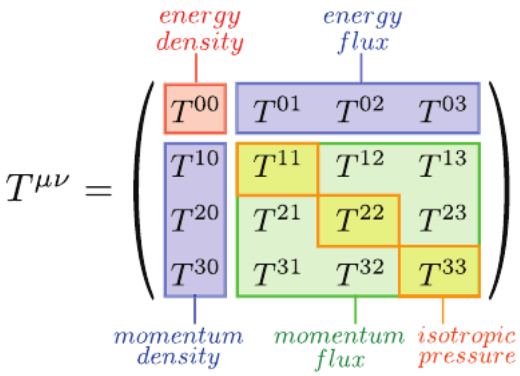

$$T^{\mu\nu} = \begin{pmatrix} T^{00} & T^{01} & T^{02} & T^{03} \\ T^{10} & T^{11} & T^{12} & T^{13} \\ T^{20} & T^{21} & T^{22} & T^{23} \\ T^{30} & T^{31} & T^{32} & T^{33} \end{pmatrix}$$

Figure 3.1: This is a schematic representation of the tensor $T^{\mu\nu}$ components physical meaning, when constructed in the rest frame of an observer comoving with the fluid.

These differential equations describes the spacetime evolution of the fundamental conserved quantities in a fluid. Notice that despite their derivation assumed a flat spacetime, the covariance of their formulation allows them to hold even in the case of curved geometries.

The derivation of RHD equations in this way is perfectly consistent from a mathematical point of view, however it carries the important drawback to rely on the expression of the distribution function. Indeed it is possible to follow a more intuitive approach for the conserved tensor construction once a physical framework is fixed. Then applying the above, general, relations the desired equations are naturally obtained.

3.1.2 Relativistic Perfect Fluids

Kinetic theory, starting from microscopic considerations, sets the mathematical and physical justifications for the construction of fluid-like behaviours. However, directly studying the problem at larger scales, allows to get rid of the nuisance represented by the formulation of an equilibrium distribution function in favour of a more intuitive analysis. To derive consistent physical considerations, it is first necessary to fix a precise framework to work with.

Relativistic perfect fluids are those in which viscous and dissipation effects are neglected hence the pressure tensor is computed to be always diagonal. Although rather simplified with respect realistic scenarios, the perfect fluid treatment carries the important advantage of maintaining the conservation of energy and momentum allowing for the construction of RHD equations in the conservative, hyperbolic formulation which guarantees an easier numerical discretization.

When considering a fluid as a whole the single particles properties are lost in favour of a global behaviour. To begin, it's required the definition of a *flow velocity* intended as the local average of all the particles velocity within the fluid element. The fluid (or flow) velocity is a 4-vector defined as usual as: $u^\mu = dx^\mu/d\tau = u^0(1, dx^i/dt)$. With τ being the fluid *proper time* and t the *coordinate time*. u^μ is defined to be always tangent to the fluid element's worldline.

From this, it is possible to directly derive the fluid 4-acceleration: $a^\mu = u^\nu \nabla_\nu u^\mu$ which is instead always orthogonal to the fluid's velocity. The 4-vectors u^μ and a^μ together describe the totality of the fluid kinematic properties.

In the case of perfect fluid the pressure tensor is considered to be isotropic and the energy flux as vanishing. Moreover, in the relativistic framework the distinction between reference frames is non trivial hence, for simplicity, the computations are first carried in the frame comoving with the fluid (or fluid element's rest frame), then the generalization to any generic frame is straightforward once the Lorentz transformations are employed. Assuming the local rest frame

of the comoving observer to be indicated with the ˆ notation, it is possible to re-draw expression for the conserved fluxes following natural considerations. For example, in the comoving frame it's expected no flux of matter along any directions, hence the *rest-mass density current* should read:

$$\hat{J}^{\mu} = (\rho, 0, 0, 0) \tag{3.23}$$

Where ρ is the rest-mass density.

Moreover, as the *stress-energy tensor* $\hat{T}^{\mu\nu}$ has been defined to be the expression for the flux of μ-momentum in the ν-direction, its construction is straightforward and, again, well summarized by Fig 3.1

In the comoving frame it reads simply:

$$\hat{T}^{\mu\nu} = \begin{pmatrix} e & 0 & 0 & 0 \\ 0 & p & 0 & 0 \\ 0 & 0 & p & 0 \\ 0 & 0 & 0 & p \end{pmatrix} \tag{3.24}$$

Where e is the *total energy density*: $e = n < p^0 >$, and it's given by the sum of the energy densities provided by the rest-mass and the internal energy ϵ.

$$e = \frac{Nm}{V}(1 + \epsilon) = \rho(1 + \epsilon) \tag{3.25}$$

By construction the stress-energy tensor is symmetric, however this must be true regardless its formulation, indeed the presence of asymmetries could induce local torques on the fluid element which can diverge in the continuum limit.

Relating the conserved tensors components to the fluid's kinematic properties it is found:

$$\hat{J}^{\mu} = \rho \hat{u}^{\mu} \tag{3.26}$$

$$\hat{T}^{\mu\nu} = e\hat{u}^{\mu}\hat{u}^{\nu} + p(\hat{\eta}^{\mu\nu} + \hat{u}^{\mu}\hat{u}^{\nu}) \tag{3.27}$$

Where η is the Minkowski metric for a flat spacetime which, for a signature (-,+,+,+), reads:

$$\eta^{\mu\nu} = \begin{pmatrix} -1 & 0 & 0 & 0 \\ 0 & 1 & 0 & 0 \\ 0 & 0 & 1 & 0 \\ 0 & 0 & 0 & 1 \end{pmatrix} \tag{3.28}$$

As the 4-velocity of the fluid's comoving frame is simply: $\hat{u}^{\mu} = (1, 0, 0, 0)$, it is straightforward to verify that 3.27 and 3.26 reduces to the respective 3.24 and 3.23.

Since these relations have to be covariant, it's immediate the generalization to any other frame:

$$J^{\mu} = \rho u^{\mu} \tag{3.29}$$

$$T^{\mu\nu} = eu^{\mu}u^{\nu} + p(g^{\mu\nu} + u^{\mu}u^{\nu}) = (e + p)u^{\mu}u^{\nu} + pg^{\mu\nu} \tag{3.30}$$

Where now u^{μ} is the 4-velocity of the observer in the generic frame with metric $g^{\mu\nu}$ [2]

[2]However it is important to remember that the quantities e and p are not Lorentz invariants but they are computed in the comoving frame In order to find the respective expression as measured in a frame with a generic velocity u'^{μ} it should be applied a Lorentz transformation to the stress-energy tensor.

Finally, it is now possible to put together the results derived for the perfect fluid framework, with the general equations obtained according to the kinetic theory (3.21,3.22) to obtain the following equations:

$$\nabla_\mu J^\mu = \nabla_\mu(\rho u^\mu) = u^\mu \nabla_\mu \rho + \rho \nabla_\mu u^\mu = 0 \qquad \textit{Continuity eq.} \tag{3.31}$$

$$\nabla_\mu T^{\mu\nu} = \nabla_\mu[(e+p)u^\mu u^\nu + p g^{\mu\nu}] \qquad \textit{Energy} - \textit{Momentum conservation} \tag{3.32}$$

These are here expressed in a rather compact and efficient notation, however it' possible to further decompose 3.32 into the three momentum conservation equations plus the energy conservation equation. The way to achieve this is to project 3.32 along, perpendicularly, to the 4-velocity. Where, in order to project any tensor onto the hypersurface orthogonal to the 4-velocity, it should be introduced the *projection tensor* $\mathbf{h}$ as $h_{\mu\nu} = g_{\mu\nu} + u_\mu u_\nu$.

Thus, by taking the contraction $\mathbf{h} \cdot \nabla \cdot \mathbf{T} = 0$ and carrying the computation, it is found:

$$u^\mu \nabla_\mu u^\nu + \frac{1}{\rho h} h^\mu_\nu \nabla_\mu p = 0 \tag{3.33}$$

Where h is the *relativistic specific enthalpy*: $h = (e+p)/\rho = 1 + \epsilon + p/\rho$ so that ρh is the *enthalpy density* which describes the inertial contribution of the rest mass. 3.33 is nothing but the *relativistic Euler equation*, it acts as the fluidodynamic formulation of the Newton' second law and states that the acceleration (the first term in the LHS) is proportional to the pressure gradient.

Instead, by taking the projection $\mathbf{u} \cdot \nabla \cdot \mathbf{T} = 0$, one derives:

$$u^\mu \nabla_\mu e + \rho h \Theta = 0 \tag{3.34}$$

Where $\Theta = \nabla_\mu u^\mu$ is called *expansion scalar* and it is the parameter describing how much the fluid volume changes (without affecting the shape) during its propagation. An incompressible fluid is defined as having zero expansion. From the continuity equation (3.31) it's directly derived that:

$$\nabla_\mu u^\mu = \Theta = -\frac{1}{\rho} u^\mu \nabla_\mu \rho \tag{3.35}$$

Hence 3.34 can be rewritten in:

$$u^\mu \nabla_\mu e - h u^\mu \nabla_\mu \rho = 0 \tag{3.36}$$

Which is the final form of the *relativistic energy-conservation equation*

In the end, the RHD consist in a system of five equations in six unknown (three components for the 4-velocity, the rest-mass density and two thermodynamic quantities such as pressure and internal energy). Therefore it requires a sixth relation to be closed. The extra equation usually relates the thermodynamic quantities of the system and it's known as Equation of State (EoS).

3.1.3 Conservative Formulation

Perfect fluid RHD has the beautiful property of being described by an *hyperbolic* system of equations and can be in principle be casted into a conservative form. The importance of this formulation follows from a couple of theorems (Lax and Wendroff,1960 and Hou and LeFloch, 1994) which state that numerical solution derived from schemes written in a conservative form are always guaranteed to converge to the physical solution even when the flows develop a discontinuity (like a shock). This section will follow the treatments of both [25] and [105].

The conservation equations previously derived can be casted in matrix form as:

$$\boldsymbol{A} \cdot \boldsymbol{\nabla U} = 0 \rightarrow (A^\mu)_{JK} \nabla_\mu U_K = 0 \tag{3.37}$$

Now, $\boldsymbol{U} = (u^\mu, e, s)^T$ is called *state vector* and contains the system variables [3], whereas $\mathbf{A}$ is a tensor embedding the 6×6 matrices $(A^\mu)_{JK}$ with the indices J and K running from 1 to 6. In components:

$$A^\mu = \begin{pmatrix} \rho h u^\mu \delta^\alpha_\beta & h^{\alpha\mu} c_s^2 & h^{\alpha\mu} \partial_s p \\ \rho h \delta^\mu_\beta & u^\mu & 0^\mu \\ 0^\mu_\beta & 0^\mu & u^\mu \end{pmatrix} \tag{3.38}$$

Where $c_s^2 = (\partial p/\partial e)_s$ is the *relativistic speed of sound*, 0^μ is the zero 4-vector and 0^μ_β is the zero 4×4 matrix. The term $\rho h u^\mu \delta^\alpha_\beta$ is a diagonal 4×4 matrix as well, with elements $\rho h u^\mu$.

In this very compact notation is summarized the set of partial differential RHD equations, in particular if the separation between the time and the spatial component is allowed, it's possible to retrieve the following expression:

$$\partial_t \boldsymbol{U} + \boldsymbol{A} \cdot \boldsymbol{\nabla U} = \boldsymbol{S} \tag{3.39}$$

Where $\mathbf{S}$ is called *source term* and can depend on $\mathbf{U}$ but not on its derivatives. If also $\mathbf{A}$ depend on the state vector, the system is called *non-linear* (or 'quasi-linear'), if instead the matrix of coefficients is independent from it, the system is *linear*.

Using this notation allows one to identify the presence of a *hyperbolic* system of equations, which is the case when $\mathbf{A}$ is diagonalisable with n real eigenvalues λ to which correspond N linearly independent right eigenvectors $\mathbf{R}$ so that it can be written:

$$\boldsymbol{A R}^{(i)} = \lambda_i \boldsymbol{R}^{(i)} \tag{3.40}$$

The advantage brought by this property is of crucial importance when dealing with numerical discretization of partial differential equation (PDEs). In fact, when studying the system evolution one has to solve a *Cauchy problem*, namely the problem of finding a solution to a set of PDEs at an arbitrary time t, knowing the solution at the origin $t = 0$ (or 'initial data'). If the solution varies little from changing the initial data, then the system is said to be *well posed*. This is a basic requirement for the convergence of a numerically computed solution. As it turns out, hyperbolic equations are always well posed hence very suitable for the discretization (see [106]). A lengthy algebraic computation is able to show that RHD equations admit a set of real eigenvalues and linearly independent right eigenvectors [105]. Therefore relativistic hydrodynamics satisfies the conditions for being considered an hyperbolic system.

The term $\mathbf{S}$ in 3.39 summarizes all those effects capable of adding (or extracting) mass, momentum and energy in (or from) the system. In the special case of ideal hydrodynamic all the dissipation effects are neglected and the fluid is assumed adiabatic, hence the term $\mathbf{S}$ vanishes and 3.39 can be treated as a homogeneous set of equations. Moreover, if $\mathbf{A(U)}$ depends on the state vector, by being the Jacobian of the related flux, it can be written: $\boldsymbol{A(U)} = \partial \boldsymbol{F}/\partial \boldsymbol{U}$, and the 3.39 can be finally casted in the *conservative form*:

$$\partial_t \boldsymbol{U} + \boldsymbol{\nabla F} = 0 \tag{3.41}$$

$\mathbf{U}$ is now called 'conserved variable', and 3.41 states that its time evolution, over any finite volume, depends only on its flux across the boundaries of said volume [25].

Indeed RHD equations, when derived within an ideal fluid framework, can be casted in this form by suitably combining the original covariant equations [107][25]. This is easy to show when dealing with a flat spacetime. In order to construct a conservative set of equations it is necessary

[3] In this formulation the thermodynamic variables are chosen to be the total energy density and the entropy s

to shift from the frame comoving with the fluid to an external one, this defines an Eulerian observer[4] and its *laboratory frame*. As usual to go from one reference frame to the other a Lorentz transformation is required, hence the Eulerian observer will measure a flow 4-velocity: $u^{\mu}_{lab} = \gamma u^{\mu} = \gamma(1, v^i)$.

Considering the conservation equations 3.31-3.32 it is clear that the continuity equation is already in the required formulation, separating the time and the spatial parts, from the laboratory point of view it will read:

$$\partial_t(\rho\gamma u^t) + \partial_i(\rho\gamma u^i) = \partial_t D + \partial_i(Dv^i) = 0 \tag{3.42}$$

Where $D = \rho\gamma$ is the laboratory, conserved mass density. Similarly by separating the contributions in 3.32:

$$\partial_t(\rho h\gamma^2 u^{\nu} + p\eta^{t\nu}) + \partial_i(\rho h\gamma^2 v^i u^{\nu} + p\eta^{i\nu}) = 0 \tag{3.43}$$

Hence:

$$\nu = t) \quad \partial_t(\rho h\gamma^2 - p) + \partial_i(\rho h\gamma^2 v^i) = 0 \tag{3.44}$$

$$\nu = j) \quad \partial_t(\rho h\gamma^2 v^j) + \partial_i(\rho h\gamma^2 v^i v^j + p\eta^{ij}) = 0 \tag{3.45}$$

Finally, by introducing the *conserved momentum* $\boldsymbol{m} = \rho h\gamma^2 \boldsymbol{v}$ and the *conserved energy* $\boldsymbol{E} = \rho h\gamma^2 - p$ the system is correctly posed in the form of 3.41, with the state vector and the flux being respectively:

$$\boldsymbol{U} = \begin{pmatrix} D \\ \boldsymbol{m} \\ E \end{pmatrix}, \qquad \boldsymbol{F(U)} = \begin{pmatrix} D\boldsymbol{v} \\ \boldsymbol{m}\boldsymbol{v} + p\mathbf{1} \\ \boldsymbol{m} \end{pmatrix} \tag{3.46}$$

Notice that while the conserved variables are directly derived from the primitive ones $(\rho, \boldsymbol{v}, p)$, the latter cannot straightforwardly be obtained from the former. Instead, such inversion requires the solution of a non-linear equation which is usually tackled through the implementations of root-finding algorithms that can introduce numerical inaccuracies.

3.2 Radiation Hydrodynamics

Hydrodynamic approach is crucial in describing a variety of problems from the small scale of laboratory experiments up to the vast astrophysical settings. However RHD equations alone have the strong limitation to be adequate only for systems in which the photon fluid (i.e the radiation) is well coupled with the matter fluid. In such a situation the *Local Thermodynamic Equilibrium* (LTE) approach is invoked, this implies that both material and radiation particles would share the same temperature and that the main interaction between the two fields is dominated by emission and absorption processes. In order for the LTE to hold, the *photon mean free path* λ_{ph} (namely the distance travelled by a photon between the interactions with gasseous matter) should be smaller than the dynamic characteristic length λ_{fluid}, over which the system changes significantly. In other words the timescale λ_{ph}/c, required to reach thermal equilibrium, should be a lot shorter than the dynamical timescale of the system λ_{fluid}/c_s (with c_s being the speed of sound). Hence the LTE is valid as long:

$$\frac{\lambda_{ph}}{c} << \frac{\lambda_{fluid}}{c_s} \rightarrow \frac{\lambda_{ph} c_s}{\lambda_{fluid} c} << 1 \tag{3.47}$$

[4]See [25] Section 7.1 for a complete explanation on the definition of 'Eulerian observer'

When this condition is satisfied the radiation system can be successfully treated in the *diffusive regime*, driven by a photon equilibrium distribution consistent with the local properties of the fluid[103].

There are, however, situations in which the 3.47 condition isn't satisfied. As the radiation moves towards the external boundaries of the fluid the density profile tend to drop, increasing the length scale between one interaction and the other. Eventually the material will become disperse enough to be transparent to the the radiation, at this point the LTE assumption ceases to be valid and the mathematical treatment for the interactions between gas particles and photons becomes increasingly involved due to the lack of equilibrium. While the LTE approximation is well suited for describing a variety of systems, from the stellar interiors to the accretion disk around a compact object, in order to study radiative emissions and shocks breakout it is necessary to develop a coherent treatment to describe the interaction between radiation and matter in radiating fluids. This will lead to the development of a *radiation hydrodynamic* formalism, which is crucial to study the SGRBs emissions. The work on which Thesis is based on rely on the algorithms derived in [108] which in turn exploits the radiation hydrodynamic formalism discussed in [103] and which is hereafter summarized.

3.2.1 Radiative Transfer

It is known since the beginning of XX-th century that light has the peculiar nature to behave simultaneously like particles and waves. In order to derive a treatment which can be efficiently discretized into a numerical method, the radiation-matter interaction should be treated choosing one of the two natures. The *radiative transfer* approach treats photons as point-like packets hence neglecting all the wave-like features such as the effects of interference and diffraction (but also refraction, dispersion and reflection), the computed intensity is assumed to be averaged over all the possible polarization states [109].
Following the same idea behind the derivation of the hydrodynamic equations, the radiative transfer approach aims to explain the global radiation field behaviour starting from microphysical considerations.

First of all, notice that photons are the relativistic particles par excellence, they yield an energy $E = h_P\nu$ and a momentum $\boldsymbol{p} = (h_P\nu)\boldsymbol{n}/c$, where h_P is the Planck constant and ν is the photon's frequency. Then, the purpose is to perform a statistical description of the photons populating the radiation field. In fact, it is possible to define an analog *photon distribution function* f_R defined so that $f_R(t,\boldsymbol{x},\boldsymbol{p})d^3p$ represents the number of photons in the momentum space. The function f_R is a Lorentz invariant and can be used to construct the *radiation specific intensity* I_ν which is defined as the amount of energy carried by a certain frequency range, in an unit time dt per unit area dS, through an infinitesimal solid angle $d\omega$ which subtends to a direction $\mathbf{n}$. Hence it holds:

$$dE = I_\nu(t,\boldsymbol{x},\boldsymbol{n})dScos\alpha d\omega d\nu dt \tag{3.48}$$

Where α is the angle between the direction $\mathbf{n}$ and the normal to the surface. In cgs I_ν is measured in $ergcm^{-2}s^{-1}Hz^{-1}sr^{-1}$. Once the distribution function along the propagation direction is known, it is possible to write:

$$I_\nu(t,\boldsymbol{x},\boldsymbol{n}) = \frac{h\nu}{c} f_R(t,\boldsymbol{x},\boldsymbol{p})d^3p \tag{3.49}$$

$$= \frac{h_P^4\nu^3}{c^2} f_R(t,\boldsymbol{x},(h\nu/c),\boldsymbol{n}) \tag{3.50}$$

Where the final expression follows from $d^3p = p^2dpd\omega = (h_P/c)^3\nu^2d\nu d\omega$.

From 3.48 and 3.50 it can be seen that the macroscopic and the microscopic properties of the radiation fields are, once again, connected by the distribution function. This means that an analog to the Boltzmann equation can be derived to describe the photons temporal evolution:

$$\frac{\partial I_\nu}{\partial t} + \boldsymbol{n} \cdot \nabla I_\nu = \eta_\nu - k_\nu I_\nu - \sigma_\nu I_\nu + \int_0^\infty d\nu' \oint d\Omega' \hat{\sigma}(\nu, \nu', \boldsymbol{n}, \boldsymbol{n'}, t, \boldsymbol{x}) I_{\nu'}(t, \boldsymbol{x}, \boldsymbol{n'}) \tag{3.51}$$

This relativistic covariant relation is called *radiative transport equation* and it is crucial to the construction of the radiation system of equations as the conservation transport equation (3.8) was for the RHD system. The terms in the RHS describe all the possible interference with the photons stream, to sum up:

- η_ν is called *emissivity* and it's the amount of energy spontaneously released, in unit time, inside the flow from spontaneous processes
- $k_\nu I_\nu$ is instead the *spontaneous absorption* and it draws energy from the radiation field.
- $\sigma_{nu} I_\nu$ acts similarly to the absorption, extracting photons from the flow, however it is due to *scattering* processes between the radiation and the gas particles, in which light is not destroyed but simply ejected away from the propagation direction
- The integral contribution to the radiation field represent the photons scattered inside the stream, with direction $\mathbf{n}$ and frequency ν from all the other directions and frequencies.[5]

The terms k_ν and σ_ν are respectively called *absorption coefficient* and *scattering coefficient*, they cannot stand alone in the equation as both the absorption and the scattering processes are directly related to the intensity of the radiation field, as opposed to the emissivity term which depend only on the properties of the surrounding matter.

Despite the clear linearity of the problem, to solve the general formulation of 3.51 can become quickly involved if the various coefficients aren't known in every point of the spacetime domain, in general to simplify the treatment an average over all the frequencies is taken (*grey-body approximation*), this allows an easier implementation of the equation at the expense of the informations on the propagation of each single wavelength. This actually prevent to formulate prediction about the emerging spectrum of the radiation but it preserves all the informations about the intensity, luminosity and temperatures of the emitting body.

3.2.2 LTE and Thermal Radiation

Before proceeding it's appropriate to set a consistent basis for the study of the radiation field evolution. In particular, as introduced before, at large densities (small photons free paths) the radiation is in equilibrium with the matter field hence its distribution function relies entirely on the temperature T of the system.

In the ideal limit of very high opacities a body is said to be in the *Black Body regime* (BB), there radiation is fully thermal and it's isotropic specific intensity can be described by the *Planck function*:

$$B_\nu(T) = \frac{2h_P\nu^3}{c^2}(e^{\frac{h_P\nu}{k_B T}} - 1) \tag{3.52}$$

Where k_B is the Boltzmann constant, the expression for $B_\nu(T)$ can be entirely derived from Bose-Einstein quantum statistics.

The total, monochromatic, *radiation energy density* can be obtained by integrating the specific intensity over the total solid angle yielding a term 4π hence:

$$E_{BB}(T) = \frac{8\pi h_P\nu^3}{c^2}(e^{\frac{h_P\nu}{k_B T}} - 1) \tag{3.53}$$

[5] $\oint$ indicates an integration over all the solid angles

Moreover, carrying an integration over all the frequencies range provides the well known relation (see [110] for computation details):

$$E_{BB}(T) = a_R T^4 \tag{3.54}$$

Which is called *Stefan's law*, here $a_R = 8\pi^5 k_B^4/15c^3h_P^3 = 4\pi\sigma_R/c$ is the *radiation constant*, whereas σ_R is the *Stefan-Boltzmann constant* which is introduced to describe the radiation flux emerging from the black-body:

$$F_{BB} = \pi B(T) = \sigma_R T^4 \tag{3.55}$$

Photons carries a relativistic momentum hence they are able to exert a pressure by interacting with the surrounding matter, since thermal radiation is isotropic then the photons collisions should equally distribute the radiation energy within the black-body 3-dimensional volume, this can be translated in the relation

$$P_\nu^{BB} = \frac{1}{3}E_\nu^{BB} = \frac{4\pi}{3}B_\nu(T) \tag{3.56}$$

Hence the total thermal radiation pressure yields:

$$P = \frac{1}{3}a_R T^4 \tag{3.57}$$

Finally, the basic assumptions for the BB regime to be valid is that the absorbed radiation should be isotropically emitted in its entirety, in other words this means that within a black-body the emissivity and the absorption coefficients must be equals:

$$\eta_\nu = k_\nu I_\nu \tag{3.58}$$

$$= k_\nu B_\nu(T) \tag{3.59}$$

This is known as *Kirchhoff-Planck relation* and allows one to derive an expression for the gas emissivity based only on the matter equilibrium with the photons thermal bath.

3.2.3 Moment Approach

Starting with the LTE formalism as zeroth assumption, it should be constructed a theory which describes non equilibrium condition, hence in which the interaction between matter and photons is not entirely dependent on the temperature. Similarities in the construction of radiative formalism with the kinetic fluidodynamic suggests the possibility to integrate the radiative transfer equations in the system describing RHD. In order to do so an analog conservation formalism should be pursued, this can be started by introducing a set of conservation laws which describe the radiation field evolution together with its interactions with the matter distribution.

The derivation will be drawn according to a mixed-frame approach [103], indeed to derive a set of hyperbolic conservation laws the point of view of the Eulerian observer (i.e the laboratory frame) should be considered. However, the physical treatment of the coefficients governing the radiation-matter interactions may suffer from the presence of anisotropies in the fluid's velocity which would burden the computations. For this reason, opacity coefficients will be derived in the comoving frame allowing one to average out any deviation from isotropicity.

Even in the grey approximation, directly solving equation 3.51 is a non trivial task, instead an alternative approach has been proposed in [108] based on the derivation of the specific intensity momentum.

The aim is to provide a formalism consistent with RHD one, so the first step is to admit that the conserved stress-energy tensor is actually provided by two contributions:

$$T^{\mu\nu} = T^{\mu\nu}_{gas} + T^{\mu\nu}_{rad} \tag{3.60}$$

While $T^{\mu\nu}_{gas}$ would be the same tensor introduced in equation 3.30, but now assuming a LTE regime for its derivation, the radiative stress-energy tensor is better understood starting from the radiative field specific intensity in the grey approximation (i.e integrated over the frequency domain). The tensor momentum can be defined by integrating it over all solid angles, yielding the covariant expression:

$$T^{\mu\nu}_{rad} = \int_0^\infty d\nu \oint d\Omega I_\nu(t, \boldsymbol{x}, \boldsymbol{n}) n^\mu n^\nu \tag{3.61}$$

Where $n^\mu = (1, \boldsymbol{n})$ is the radiation direction of propagation and $d\Omega$ the differential solid angle which subtends to $\mathbf{n}$. In this way, $T^{\mu\nu}_{rad}$ basically describes the rate of transport of the μ-th component of the radiative momentum (per unit volume) along the ν direction. In components:

$$E_{rad} = \int_0^\infty d\nu \oint d\Omega I_\nu(t, \boldsymbol{x}, \boldsymbol{n}) \tag{3.62}$$

$$F^i_{rad} = \int_0^\infty d\nu \oint d\Omega I_\nu(t, \boldsymbol{x}, \boldsymbol{n}) n^i \tag{3.63}$$

$$P^{ij}_{rad} = = \int_0^\infty d\nu \oint d\Omega I_\nu(t, \boldsymbol{x}, \boldsymbol{n}) n^i n^j \tag{3.64}$$

Among other things, this formally defines the quantities of radiative energy, fluxes and pressure which were already functionally introduced in the previous section.

Finally, the radiative stress energy tensor can be casted in the compact form:

$$T^{\mu\nu}_{rad} = \begin{pmatrix} E_{rad} & F^i_{rad} \\ F^j_{rad} & P^{ij}_{rad} \end{pmatrix} \tag{3.65}$$

This formulation allows treating consistently the fluid and the radiative stress-energy tensor. In fact, by requiring the conservation of energy and momentum one finds:

$$\nabla_\mu T^{\mu\nu} = 0$$
$$\nabla_\mu (T^{\mu\nu}_{gas} + T^{\mu\nu}_{rad}) = 0$$

Hence

$$\nabla_\mu T^{\mu\nu}_{gas} = -\nabla_\mu T^{\mu\nu}_{rad} \tag{3.66}$$

This relation explicitly express the existence of a connection between matter and radiation, which can be quantified by substituting $\nabla_\mu T^{\mu\nu}_{rad}$ through 3.61 and applying the RHS of the radiative transfer equation to directly derive the interaction terms:

$$G^\mu = -\int_0^\infty d\nu \oint d\Omega \left[\eta_\nu - k_\nu I_\nu - \sigma_\nu I_\nu + \int_0^\infty d\nu' \oint d\Omega' \hat{\sigma}(\nu, \nu', \boldsymbol{n}, \boldsymbol{n'}, t, \boldsymbol{x}) I_{\nu'}(t, \boldsymbol{x}, \boldsymbol{n'}) \right] n^\mu \tag{3.67}$$

This is called *4-force vector* and represents the way the two fluids communicate during the propagation of the radiative flow. Notice that the system of equation which will be constructed, despite being expressed in a hyperbolic and conservative formulation, won't be homogeneous anymore due to the introduction of a source term:

$$\nabla_\mu T^{\mu\nu}_{gas} = G^\mu \tag{3.68}$$

$$\nabla_\mu T^{\mu\nu}_{rad} = -G^\mu \tag{3.69}$$

3.2.4 Interaction term

The above *4-force vector* is rather involved, however in the chosen momentum approach a few simplifications can be applied (see [108] for a detailed treatment).

First of all, as said before, the treatment of the interacting terms should be carried in the comoving frame of the fluid, in this way any anisotropies related to the fluid's flow can be safely neglected. The covariant derivation will then guarantee the extrapolation of the expression for G^μ in the laboratory frame just by applying a Lorentz transformation. To differentiate, quantities computed in the comoving frame will be indicated with the $\hat{}$ notation.

For simplicity the scattering processes are assumed to be coherent (i.e they don't change with the frequency) and isotropic. In fact it's possible to shown that the form for the RAD-RHD system of equations is going to be the same either by considering isotropic or highly anisotropic scattering processes [108]. This condition translates in the fact that photons have equally probability to be scattered along any direction, hence $\hat{\sigma}$ is independent from both **n** and **n'**. Thus by introducing the angle average of the specific intensity $\hat{J}_\nu$ (i.e the *mean intensity*) it is possible to rewrite:

$$\hat{G}^\mu = \int_0^\infty d\nu \oint d\Omega \left(\chi_\nu \hat{I}_\nu - \sigma_\nu \hat{J}_\nu - \hat{\eta}_\nu\right) n^\mu \tag{3.70}$$

Where $\chi_\nu = k_\nu + \sigma_\nu$ is the *total opacity coefficient*.

Then, as this relation has been written in the comoving frame, the intensity is isotropic suggesting a form for the emissivity coefficient $\hat{\eta}_\nu$ similar to the one which holds in the LTE (eq 3.58-3.59). This is a first order approximation of the treatment, as the region in which it is applied may diverge a lot form the equilibrium. However, due to the fact that RHD is derived assuming LTE, the alternative would consist in introducing a totally different modeling of matter dynamics, extremely increasing the complexity.

Moreover, by applying *grey-body approximation*, it is possible to carry out the chromatic integrals by substituting the frequency-dependent opacities with their respective averaged values, this is possible by introducing the *Planck average*:

$$k_P = \frac{\int_0^\infty d\nu k_\nu B_\nu(T)}{\int_0^\infty d\nu B_\nu(T)} \tag{3.71}$$

and the *Rosseland average*:

$$\chi_R = \frac{\int_0^\infty d\nu \left(\frac{\partial B_\nu(T)}{\partial T}\right)}{\int_0^\infty d\nu \chi_\nu^{-1} \left(\frac{\partial B_\nu(T)}{\partial T}\right)} \tag{3.72}$$

This introduces some errors, in particular k_P is mostly valid in optically thin material whereas χ_R is more correct in the diffusion regime [103].

Replacing the approximations and carrying out the angle integrals, the final form for the interaction term, in the comoving frame, can be written as:

$$\hat{G}^\mu = \rho \left[k_P \left(\hat{E}_{rad} - 4\pi B(T)\right), \chi_R \hat{\boldsymbol{F}}_{rad}\right] \tag{3.73}$$

Where the relation between the mean intensity and the energy density: $\hat{J} = \hat{E}_{rad}/4\pi$ has been used.

Lastly, the laboratory frame 4-force is retrieved just applying a lorentz transformation [111]:

$$G^\mu = \Lambda^\mu_\alpha(\boldsymbol{v}) \hat{G}^\alpha \tag{3.74}$$

Where $\Lambda^\mu_\alpha(\boldsymbol{v})$ is the tensor representation of a Lorentz boost for a fluid with velocity **v**.

This yields:

$$G^{\mu} = -k_P \rho (T^{\mu\alpha}_{rad} u_{\alpha} + 4\pi B(T) u^{\mu}) - \sigma \rho (T^{\mu\alpha}_{rad} u_{\alpha} + T^{\alpha\beta}_{rad} u_{\alpha\beta} u^{\mu}) \tag{3.75}$$

Despite all the approximations, the great advantage of this formulation is to provide an interaction term that, once fixed the opacities parameters, can be always computed starting from the local values of matter and radiation fields.

3.3 RAD-RHD equations

The momentum approach to the radiation field introduces three extra fields to the treatment, however it is possible to provide a closure relation which relates the radiative pressure to the energy density and the flux, effectively reducing the independent radiation variables.

The choice was to implement a relation able to handle both the optically thick and thin regimes, this is possible by introducing the so called M1 closure[112]. In order to develop such relation the radiation specific intensity is assumed to be isotropic in at least one specific reference frame called *radiation frame*. There the radiation stress-energy momentum can be easily computed. Then, by extrapolating it in the external laboratory frame by means of a Lorentz transformation, the desired closure relation is obtained. This procedure yields:

$$P^{ij}_{rad} = D^{ij} E_{rad}, \tag{3.76}$$

$$D^{ij} = \frac{1-\xi}{2}\delta^{ij} + \frac{3\xi - 1}{2} n^i n^j, \tag{3.77}$$

$$\xi = \frac{3 + 4f^2}{5 + 2\sqrt{4 - 3f^2}}, \tag{3.78}$$

$$n^i = \frac{F^i_{rad}}{||F^i_{rad}||}, \qquad f = \frac{||F^i_{rad}||}{E_{rad}} \tag{3.79}$$

These equations are explicitly covariant and hold in any reference frame. The M1 closure can smoothly handle all the optically regimes of the fluid, in particular:

- if $||F^i_{rad}|| << E_{rad}$ then $P^{ij}_{rad} \to (\delta^{ij}/3) E_{rad}$. This correspond to the more common *Eddington approximation* which assumes the specific intensity to be overall isotropic as usually happens in diffusive regimes.

- if $||F^i_{rad}|| \approx E_{rad}$ then $P^{ij}_{rad} \to E_{rad} n^i n^j$. This correspond to a delta-like specific intensity oriented in the flux direction. This is the *free streaming limit* limit, it holds when the radiation frame velocity tends to c, and it is used to describe regimes in which the radiation is de-coupled from the matter

The main drawback of the M1 closure occurs with the treatment of highly asymmetric systems in which it is not possible to find a reference frame in which I_ν can be considered isotropic. This can eventually lead to the development of important physical instabilities.

Finally, having introduced the radiation through equations 3.68-3.69 with source term given by equation 3.75 and implementing the M1 closure relations, it is possible to draw a quasi-conservative systems of equations describing consistently the evolution of a radiative, relativistic

fluid:

$$\frac{\partial(\rho\gamma)}{\partial t} + \nabla \cdot (\rho\gamma \boldsymbol{v}) = 0 \tag{3.80}$$

$$\frac{\partial E}{\partial t} + \nabla \cdot (\boldsymbol{m} - \rho\gamma \boldsymbol{v}) = G^0 \tag{3.81}$$

$$\frac{\partial \boldsymbol{m}}{\partial t} + \nabla \cdot (\rho h \gamma^2 \boldsymbol{v}\boldsymbol{v}) + \nabla p = \boldsymbol{G} \tag{3.82}$$

$$\frac{\partial E_{rad}}{\partial t} + \nabla \cdot \boldsymbol{F}_{rad} = -G^0 \tag{3.83}$$

$$\frac{\partial \boldsymbol{F}_{rad}}{\partial t} + \nabla \cdot \boldsymbol{P}_{rad} = -\boldsymbol{G} \tag{3.84}$$

These are the equations constituting the RAD-RHD system. They hold in any frame and can be computed in linear and curvilinear geometries. Moreover, these equations are consistent with the modern discretization algorithms, allowing one to safely handle a variety of problems in different regimes. Therefore the system is well suited to describe and model SGRB propagation and emission.

Chapter 4

Numerical Framework

In the previous chapter the equations governing the evolution of relativistic fluidodynamic have been derived. It was shown how the obtained system is naturally quasi-linear and hyperbolic and, in particular, how the non linearity may rise problems hard to be tackled analytically hence justifying the importance of constructing efficient methods which provide approximated, but consistent, numerical solutions.

Numerical method for hydrodynamics consist in a variety of approaches and implementations or schemes which are divided in two macro-families:

- Grid-Based Methods: These techniques are based on an Eulerian kind of approach. They include the existence of a finite grid (or mesh) which discretises the continuum domain providing that numerical solutions are evaluated at each specific point.

- Particle-Based Methods: Also known as *Smooth Particle Hydrodynamics* (SPH) methods, they are based on a Lagrangian point of view. Within these methods the physical domain isn't discretised in a grid and the system properties are represented by an ensemble of coordinate-free particles [113].

While the SPH approach offers many advantages in terms of computational efficiency and resolution, it still lacks a full covariant formulation hence limiting its applications especially when dealing with relativistic problems. As a consequence, the work developed in this Thesis has been chosen to follow the Eulerian approach.

Traditionally grid-based implementations rely on *finite difference* techniques in which the solution of the differential equation system is assumed to be smooth at each spacetime point, however this prevents from correctly handling discontinuous flows and shocks.

The whole effort spent at deriving a conservative formulation for the hydrodynamic equation is now justified by the possibility to develop and implement a new class of methods . In fact while the finite difference methods are non-conservative and require continuity, the so called *high-resolution shock capturing methods* (HRSC) are entirely time-conservative and able to to efficiently manage the presence of perturbations.

This Chapter is devoted to the review of the key points for the numerical framework applied in the Thesis and it's based on the treatments proposed in [25] and [114]. In section 4.1 will be presented the basic aspects of numerical treatment for hyperbolic equations. In section 4.2 the HRSC methods will be introduced paying particular attention at the PLUTO code for the treatment of relativistic astrophysical plasma. Finally in section 4.3 the PLUTO additional module able to handle radiation hydrodynamic will be briefly described.

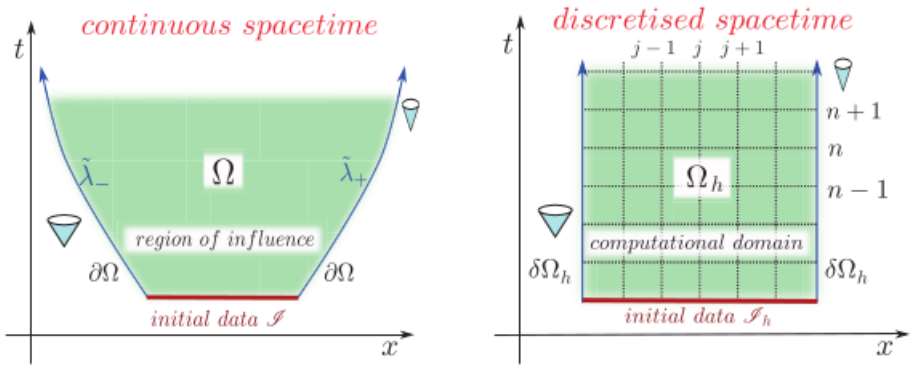

Figure 4.1: This schemes summarizes the process of discretise the spacetime domain for the solution Ω. The edges $\partial\Omega$ mark the boundaries that contains the region in which the characteristics of the solution act. In the discretised domain, $\delta\Omega$ edges can usually causally interact with the solution space Ω_h, providing the so called *boundary conditions*. Image taken from [25].

4.1 Basic Notions

The fundamental concept on which numerical techniques are based on is the *discretisation* of the problem at hand. Every physical fluidodynamic problem is naturally defined in the continuum limit, however in order to be handled numerically a finite decomposition must be performed (see Fig 4.1), even if this will inevitably include errors in the treatment. If the discretisation is performed consistently then the approximated computed solutions will eventually converge to the exact ones.

4.1.1 Discretisation

Consider a Cauchy problem, for the scope of the treatment it's possible to work with an easier, linear and 1-dimensional system.

$$\begin{aligned} &\partial_t u + A\partial_x u = 0 \\ &(x,0) = u_0(x) \end{aligned} \tag{4.1}$$

Where u_0 indicates the *initial value* of the problem.

Discretising means fixing a grid so that the spacetime coordinate points can be represented as

$$\begin{aligned} t_n &= t_0 + n\Delta t, \qquad & n &= 0, 1, ..., N_t \\ x_j &= x_0 + j\Delta x, \qquad & j &= 0, 1, ..., J \end{aligned}$$

If the grid has uniform spacing then the distance between space points would be $h = \Delta x$ and between temporal points $k = \Delta t$.

The generic solution of the problem can be discretised as well by applying a finite numerical method which produces a discrete set of variables U_j^n (also called *gridfunctions*) which in turn approximate the exact value the real solution would assume at the gridpoint x_j^n, these are usually denoted as:

$$U_j^n \approx u(x_j^n) = u_j^n \tag{4.2}$$

When defined in this way, that is for each point of the discrete spacetime domain, the approximation is said to be *pointwise*. More often in modern algorithm for conservation laws the approximation is defined as the approximation of the *cell average* of the true solution, namely:

$$\bar{U}_j^n \approx \bar{u}_j^n = \frac{1}{h}\int_{x_{j-(1/2)}}^{x_{j+(1/2)}} u(x, t_n)dx \tag{4.3}$$

In general the discretised solutions properties depends on the specifics of the discretisation (namely, h and k) and on the numerical method chosen. In fact, the differential operator acting on the true solution u should be also discretised through the implementation of some scheme. In this way the continuum Cauchy problem initially defined is now entirely replaced by a discrete initial value problem.

Say that the real problem can be casted in the form $l(u) - f = 0$, where $l(u)$ is a generic differential operator and f is a source function dependent on u only, then after the discretisation process the problem becomes:

$$L_h(U_j^n) - F_h = 0 \tag{4.4}$$

Now L_h represents the numerical differential operator so that when it's applied to the approximated solution U_j^n the system is satisfied. However notice that if the discretised formulation should be applied to the true solution then: $L_h(u_j^n) - F_h \neq 0$, as U_j^n is only an approximation of the real solution. The difference between this relation and the zero is a measure of the error introduced with the discretisation process

4.1.2 Errors and convergence

The application of a numerical method inevitably raises errors which differentiate the approximate solution from the real one. Well done implementations are those that generate predictable numerical errors, this allows to straightforward subtract the nuisance and to correct, for what is possible, the computed solution. The basic source of inaccuracy comes from the machine precision, in fact every calculators has a finite way to represent rational number which instead should be infinite by definition. The machine precision error is the computers ability to distinguish between two floating point numbers and it mostly depends on the hardware features. Many numerical errors, summed over various floating-point operations, build up the *round-off error*, this depends roughly on the square number of the operations implemented and fixes a minimum in the available accuracy.

Finally, the so called *truncation error* represent the 'goodness' of the numerical discretisation applied, and its entirely under human control. The *local truncation error* states how much the numerical method is able to reproduce, point by point, the differential equation. It can be expressed by applying the discretised differential operator $L_h - F_h$ to the true solution u_j^n:

$$(\epsilon^{(h)})_j^n = [L_h(u_j^n) - F_h] - [l(u_j^n) - f] = L_h(u_j^n) - F_h \tag{4.5}$$

This clearly correspond to evaluate the difference between the action of the numerical method on the exact solution and the application of the continuum differential operator as the latter part is zero by default. In other words, the local truncation error can be seen as the error introduced when selecting a specific numerical representation for the differential problem. Notice that the superscript 'n' can be dropped as the time and the spatial discretisation are assumed to be comparable $h = \Delta x \sim \Delta t$, in particular for time dependent hyperbolic equation in general the *mesh ratio* k/h is considered constant. This allow to consider just one spacing in the notation. Furthermore, as the truncation error clearly depend on the discretisation it can also be written:

$$\epsilon_j^{(h)} = \bar{C} h^{\bar{p}_j} + o(h^{\bar{p}_j + 1}) \tag{4.6}$$

Where $\bar{C}$ is a constant and $\bar{p}_j$ is called *local order of accuracy*. The overall difference between the real solution and the approximated one is known as *local error* and can be expressed as:

$$E_j^{(h)} = u_j - U_j^{(h)} \qquad pointwise\ \ error \tag{4.7}$$

or

$$\bar{E}_j^n = \bar{u}_j - \bar{U}_j^{(h)} \qquad cell - averaged\ \ error \tag{4.8}$$

From this is clear that local error and local truncation error are related:

$$E_j^{(h)} = (L_h)^{-1}\epsilon_j^{(h)} = Ch^{\bar{p}_j} + o(h^{\bar{p}_j+1}) \tag{4.9}$$

Therefore also the local error depends the spacing of the discretisation.

From the local error is possible to derive a generalization to all the gridpoints, defining the *global error*. This can be performed considering a spatial average over the whole numerical domain which can be achieved, for example, introducing the *norm*. There are many different implementations for the norm, the more applied in conservative numerical methods is the 1-form:

$$||v(x)||_1 = \int_{-\infty}^{\infty} |v(x)|dx \tag{4.10}$$

Where v(x) is a generic function. For the discrete solution this can be easily re-written as:

$$||U^n||_1 = h\sum_j |U_j^n| \tag{4.11}$$

Applying the norm it's possible to extrapolate the definition of *global truncation error* as:

$$\epsilon^{(h)} = |||\epsilon_j^{(h)}| = ||L_h(u_j^n) - F_h|| \tag{4.12}$$

and that of *global error* as:

$$E^{(h)} = ||E_j^{(h)}|| = ||u_j - U_j^{(h)}|| \tag{4.13}$$

The described errors definitions are fundamental to derive a few basics principles necessary to discriminates whether a numerical method is adequately implemented or not.

First of all a scheme must be *globally consistent* that is the discretised differential operator should satisfy:

$$\lim_{h\to 0} \epsilon^{(h)} = 0 \tag{4.14}$$

Moreover it should also *globally convergent*, which translates to:

$$\lim_{h\to 0} E^{(h)} = \lim_{h\to 0} Ch^p = 0 \tag{4.15}$$

Where now p is the *global order of convergence*.

Clearly the equivalent local expression of these criteria can be obtained by substituting $E^{(h)}$ and $\epsilon^{(h)}$ with their respective $E_j^{(h)}$, $\epsilon_j^{(h)}$.

Finally, the last criteria to be satisfied is the *stability*. The repeated application of the discretised L_h accumulates, each time, some truncation error which should grow in a controlled way. It is possible to show, by performing a Taylor expansion [114], that for each time $T = t^n$ (after n applications) there exist a constant C_s and a number h_0 so that:

$$||L_h^n||_1 \leq C_s \qquad \forall nh \leq T \quad \& \quad h < h_0 \tag{4.16}$$

This condition doesn't exclude some growth of the of the error, in particular stability is still guaranteed if

$$||L_h||_1^n \leq (1+\xi h)^n \leq e^{\xi hn} \leq e^{\xi T} \tag{4.17}$$

This means that the solution can grow no more faster than an exponential.

The stability of a numerical method can be further characterised by introducing the *Courant-Friedrichs-Lewy* (CFL) condition. This requires that the domain of dependence of the numerical solution always contains the domain of dependence of the true solution at a generic point, which

is defined by the slope of the characteristics (λ) converging at that point. In other words the CFL condition guarantees that no physical perturbation can propagates faster than the numerical speed: $\Delta x/\Delta t$, hence:

$$|\lambda| \leq \frac{\Delta x}{\Delta t} \tag{4.18}$$

In practice, once the resolution is fixed, the CFL condition is used to define a factor (always ≤ 1) which constraints the timestep so that stability is obtained.

4.2 HRSC codes

In chapter 3 was briefly developed the system of equations governing the relativistic hydrodynamic flows in a conservative formulation, as a justification it was reported the fundamental result of Lax and Wendroff which states that convergent conservative numerical method always converge to the solution of the problem. In fact, as long as the solution is smooth and well-behaved, non-conservative methods are still found adequate to work with. However it was quickly noted that in presence of shocks and perturbations more stable and efficient methods should be applied [115]. This consideration led to the development of a conservative class of methods which is able to handle accurately even the most discontinuous problems and that are known as *high-resolution shock-capturing* (HRSC) methods.

An appropriate conservative scheme must be able to efficiently solve a Cauchy problem presenting a discontinuity in the initial value, namely a *Riemann problem*. Consider for simplicity a generic conservative equation in 1 dimension:

$$\partial_t U + \partial_x F(U) = 0 \tag{4.19}$$

It is said that the solution is discontinuous if there exist a jump in the initial conditions moving with speed S along a spacetime worldline (s(t),t). Such jump separates two regions in which the solution admits two well distinct states $U_L = U(x_L, t)$ and $U_R = U(x_R, t)$. Then, by integrating the system in a spatial domain $[x_L, x_R]$ big enough to comprise the discontinuous curve it is found:

$$F(U_L) - F(U_R) = \frac{d}{dt}\int_{x_L}^{x_R} U(x,t)dx \tag{4.20}$$

$$= \frac{d}{dt}\int_{x_L}^{s(t)} U(x,t)dx + \frac{d}{dt}\int_{s(t)}^{x_r} U(x,t)dx \tag{4.21}$$

$$= S(U_L - U_R) + \int_{x_L}^{s(t)} \partial_t U(x,t)dx + \int_{s(t)}^{x_r} \partial_t U(x,t)dx \tag{4.22}$$

Where $S = ds/dt$. Restricting in the limit: $x_L \to s^-(t)$ and $x_R \to s^+(t)$ the integrals vanish and it is obtained:

$$F_L - F - R = S(U_L - U_R) \tag{4.23}$$

This is the *Rankine-Hugoniot condition* (R-H) condition which express the conservation laws across a discontinuity. Notice that this is a mathematical derivation which is not able to discriminate the physical solution from the un-physical ones, thus in order to guarantee the former, additional considerations should be provided. One of the most famous is the *entropy condition* which states that in order to retrieve physical realism a solution must admit a discontinuity which collides from both sides with only one of the systems characteristics, while it collides from one side with all the remaining.

There are many formulations for the conservative numerical methods, they mostly differ for:

The discretisation technique: If the scheme is built on cell-averages (see 4.4) it's known as a *finite-volume method*, and it yields:

$$U_j^{n+1} = U^n + \frac{\Delta t}{\Delta x}(F_{j-1/2-F_j+1/2}) \tag{4.24}$$

Where the fluxes are the time average of the physical fluxes.

$$F_{j\pm1/2} = \frac{1}{\Delta t}\int_{t^n}^{t^{n+1}} F[U(x_{j\pm1/2}, t)]dt \tag{4.25}$$

Instead if the differential operator is directly represented through a finite-difference scheme, obtained through a Taylor expansion and without integrating in space and time, then it's known as *conservative finite-differences method* (as opposed to the non-conservative finite-differences method) which can be written as:

$$\frac{dU_j}{dt} = \frac{1}{\Delta x}(\hat{F}_{j-1/2} - \hat{F}_{j+1/2}) \tag{4.26}$$

In this case the state variable is defined as in 4.3 and $\hat{F}_{j\pm1/2}$ is an high order approximation of the primitive, physical flux defined so that its cell average coincides with the pointwise real term. Notice that both the numerical fluxes are defined so that they reduce to the real ones in the case of a constant flow. The two methods turn out to behave similarly for low-order method, however when applied to irregular or complex meshes the finite-volume method is preferred.

The update scheme: One of the main properties of a conservative method should be the correct tracking of the formation and evolution of perturbations. A way to do this is to implement *Central numerical schemes*: one of the main implementation families of this class is known as *staggered central scheme* and consists in performing a new discretisation of the problem by taking a volume average centered in $x_{j+1/2}$ rather than in x_j, hence yielding:

$$U_{j+1/2}^{n+1} = U_{j+1/2}^n - \frac{1}{\Delta x}\left[\int_{t^n}^{t^{n+1}} F[U_{x_j+1,t}]dt - \int_{t_t^n}^{t_t^{n+1}} F[U(x_j, t)]dt\right] \tag{4.27}$$

Where the state vector is now a *staggered average*:

$$U_{j+1/2}^n = \frac{1}{\Delta x}\int_{x_j}^{x_{j+1}} U(x, t^n)dx \tag{4.28}$$

This enables the big advantage of having no discontinuity in the middle point of the staggered cell $U(x_j, t)$, hence the fluxes computation can avoid to deal with shocks.

Nevertheless, more usually the choice falls on the so called *upwind schemes*. Upwinding is the properties of capturing and following the position of the discontinuities in the flow, this can be performed by working with the characteristic structure of the problem. In other words upwind schemes are able to manage the informations on all the eigenvalues of the matrix $\mathbf{A}$ (see 3.39), which represent the velocities associated to the system's components. This can be performed by solving a Riemann problem at each cell interface.

Upwind methods were first designed by Godunov [116] whose idea was based on the concept that, in practice, when performing a numerical discretisation at each juncture between adjacent cells an artificial discontinuity is inevitably generated. Therefore fluxes at the edges of the cells can be computed by solving a series of local Riemann problem.

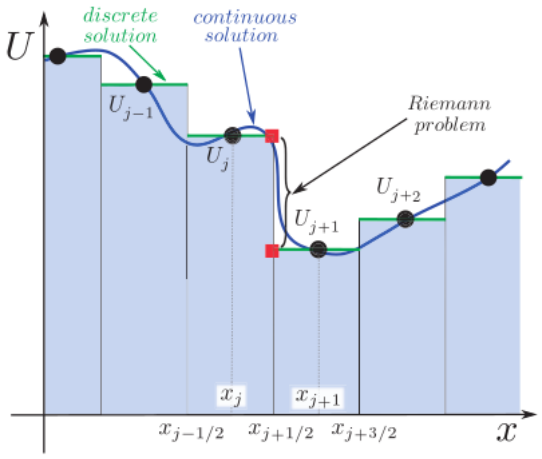

Figure 4.2: This is a schematic representation of the Godunov method. The real solution (blue line) is discretised into a series of finite volume as constant values (green line). hence between each cell edge a local Riemann problem is obtained. The image is taken from [25]

The basic Godunov method (summarized in Fig 4.2) consists into taking a cell-average discretisation in which the real solution is represented by finite, different constant values over different cells. Then at each interface a Riemann problem is generated:

$$U(x,0) = \begin{cases} U_j^n & if\ x < x_{j+1/2}, \\ U_j^n + 1 & if\ x > x_{j+1/2} \end{cases} \tag{4.29}$$

Then, after solving the problem, the state $U(x_{j\pm1/2}, t)$ is obtained from which the computation of the fluxes $F_{j\pm2}$ is straightforward (see 4.26). This method guarantees that the numerical fluxes naturally follow the characteristic waves propagation, hence they are able to track the correct perturbations directions. The original scheme implemented by Godunov was accurate only at first order, as no linear and stable method can be more accurate than that [116]. However modern implementations exploits non-linear techniques thanks to which the spatial accuracy of the method is increased by reconstructing the left and right states of the Riemann problem with a polynomial representation (hence they aren't anymore simple constant values as in the original formulation) before being effectively solved. Indeed modern Godunov-based method are at all effects considerable as HRSC. They are usually able to handle large discontinuities without introducing spurious oscillations, maintaining at at least a second order in accuracy for the smooth parts of the solution.

4.2.1 PLUTO

The main part of this work is based on numerical simulations performed with the relativistic-magnetohydrodynamic (RMHD) open-source code PLUTO [117]. PLUTO is a grid-based code able to solve 1-,2-, or 3-dimensional systems of conservative differential equations in different geometries, with particular orientation toward hypersonic astrophysical plasmas. In particular the code implements finite volume schemes and it is specialized in solving and evolving fluid discontinuities applying the more recent implementations of Godunov-type shock-capturing schemes.

As a member of the HRSC family, PLUTO strategy is based on the RSA (*reconstruct-solve-average*) algorithm, which consists in a 3-step procedure that leads to the solution update. Furthermore, despite being casted in a conservative formulation, with U denoting the state vector, PLUTO performs an extra step during which a primitive state vector V is obtained from

the former as, it turns out, interpolation on primitive variables allows the enforcing of some physical constraints and it's in general preferable [117].

The basic routine of the code is here quickly reviewed:

Step 1: Reconstruction As mentioned above, in order to improve the spatial accuracy a first interpolation is performed to better fit the solution behaviour within the cell averages. To do so in each cell a specific routine is implemented obtaining a piecewise polynomial approximation:

$$V_{\pm s} = I(P, V) \tag{4.30}$$

Where s is the generic state (left or right), P is the polynomial function to be obtained and I represents the chosen interpolation procedure. This provides the reconstructed left and right edges of the cell $V_{\pm}$.

Now, implementing an interpolation introduces extra approximations and it can in principle rise spurious oscillation especially if in presence of steep gradients. A way to measure the number of oscillation is through the definition of *total variation* (TV), in 1-D:

$$TV(U^n) = \sum_{j=-\infty}^{+\infty} |U^n - U^n_{j-1}| \tag{4.31}$$

So, an adequate method is the one that in its implementation doesn't increase the TV:

$$TV(U^{n+1} \leq TV(U^n)) \tag{4.32}$$

That is a *total-variation diminishing* (TVD) method. One way to impose the TVD is through the application of a *slope limiter* which appropriately caps the steepness of the approximated solution within the cell. Thus, the generic reconstruction interpolants would produce:

$$V_{\pm,s} = V \pm \frac{\Delta\tilde{V}}{2} \tag{4.33}$$

Where the slopes $\Delta\tilde{V}$ are suitably controlled by said limiter. A frequently used example of interpolation routine is the *piecewise-parabolic method*, which is also the one applied in the Thesis work.

Step 2: Riemann Solver Once the reconstruction has been performed the extremes of the Riemann problem are set, in this way, once solved, it will be possible to derive the numerical fluxes enabling the timestep evolution. Nevertheless, the exact solution of a Riemann problem can be a difficult and expensive task to achieve. Rather, a number of approximate solvers have been proposed, they are all based on different approximations order going from the less expensive but diffusive, to the more sophisticated and pricey ones.

In general approximated Riemann solver divides into *complete* and *incomplete* ones, while the former works with the totality of the informations on the characteristic waves of the system, the latter focus on a a subset comprising only the more important. Notice that usually the completeness of a solver depends on the set of equations.

In PLUTO are implemented a number of solver, the main used are the HLL [118] and the HLLC [119].

The HLL is an incomplete Riemann solver in which the initial discontinuity is assumed to be decomposed into only the two fastest waves of the problem, propagating in opposite directions with velocities $\lambda_L \leq 0$ and $\lambda_R \geq 0$:

$$U(x,t) = \begin{cases} U_L & if\ x/t < \lambda_L \\ U^{HLL} & if\ \lambda_L < x/t < \lambda_R \\ U_R & if\ x/t > \lambda_R \end{cases} \tag{4.34}$$

Where U^{HLL} is the constant state created between the characteristics. From this configuration it is possible to define a *control volume* $W = [-\Gamma, \Gamma] \times [0, T]$ where $\Gamma = max(|\lambda_L|, |\lambda_R|)T$. Integrating eq 4.20 over W it is found:

$$\begin{aligned}\int_{-\Gamma}^{\Gamma} U(x,T)dx &= \int_{-\Gamma}^{\Gamma} U(x,0) + \int_0^T F(U(-\Gamma,t))dt - \int_0^T F(U(\Gamma,t))dt \\ &= \int_{-\Gamma}^{0} U_L dx + \int_0^{\Gamma} U_R dx \int_0^T F(U(-\Gamma,t))dt - \int_0^T F(U(\Gamma,t))dt \\ &= \Gamma(U_L + U_R) + T(F_L - F_R) \end{aligned} \tag{4.35}$$

Whereas the LHS can be rewritten as:

$$\begin{aligned}\int_{-\Gamma}^{\Gamma} U(x,T)dx &= \int_{-\Gamma}^{T\lambda_L} U_L dx + \int_{T\lambda_L}^{T\lambda_R} U^{HLL} dx + \int_{T\lambda_R}^{\Gamma} U_R dx \\ &= U_L(T\lambda_L + \Gamma) + U^{HLL}(\lambda_R - \lambda_L)T + U_R(\Gamma - T\lambda_R) \end{aligned} \tag{4.36}$$

In this way the terms in Γ and T cancel out and it is obtained:

$$U^{HLL} = \frac{\lambda_R U_R - \lambda_L U_L + F_L - F_R}{\lambda_R - \lambda_L} \tag{4.37}$$

Applying the R-H condition across the discontinuity yields:

$$F_{L*} = F_L + \lambda_L(U^{HLL} - U_L) \tag{4.38}$$

$$F_{R*} = F_R + \lambda_R(U^{HLL} - U_R) \tag{4.39}$$

As U^{HLL} is known given the characteristics speeds, the HLL flux is provided by:

$$F_* = \frac{\lambda_R F_L - \lambda_L F_R + \lambda_L \lambda_R (U_R - U_L)}{\lambda_R - \lambda_L} \tag{4.40}$$

Which will be implemented as:

$$F^{HLL} = \begin{cases} F_L & if \quad x/t < \lambda_L \\ F_* & if \quad \lambda_L < x/t < \lambda_R \\ F_R & if \quad x/t > \lambda_R \end{cases} \tag{4.41}$$

Therefore, once the characteristic velocities have been computed, the solver can be easily implemented.

It turns out that the HLL Riemann solver handles well even the stronger shocks, however it performs poorly in presence of contact discontinuities due to the lack of middle informations between the two principal waves. For this is reason it has been implemented the complete HLLC approximate solver. In HLLC two extra, intermediate states are introduced U_{L*}, U_{R*} separated by an approximated contact discontinuity propagating with λ_C. Then the total system state and the respective HLLC flux can be written as:

$$U(x,t) = \begin{cases} U_L & if \quad x/t < \lambda_L \\ U_{L*} & if \quad \lambda_L < x/t < \lambda_C \\ U_{R*} & if \quad \lambda_C < x/t < \lambda_R \\ U_R & if \quad x/t > \lambda_R \end{cases}, \qquad F^{HLLC} = \begin{cases} F_L & if \quad x/t < \lambda_L \\ F_{L*} & if \quad \lambda_L < x/t < \lambda_C \\ F_{R*} & if \quad \lambda_C < x/t < \lambda_R \\ F_R & if \quad x/t > \lambda_R \end{cases} \tag{4.42}$$

Where fluxes and states are as usual related by the R-H condition

Step 3: Temporal Evolution Consider again the problem described by 4.19 but this time generalized to 3-dimensions (as in 3.41):

$$\partial_t U + \nabla \cdot T(U) = S(U) \tag{4.43}$$

Where now T(U) is the rank-2 flux tensor.[1] As the state U has been adequately reconstructed and the fluxes derived to the approximate Riemann solver, it is possible to update the timestep and start over. In PLUTO various schemes are available, consisting mostly in fully discrete *zone-edge extrapolated* and the semi-discrete *method of lines*.

The zone-edge extrapolated techniques has second order temporal accuracy and are formulated as single step methods:

$$U^{n+1} = U^n + \Delta t L^{n+1/2} \tag{4.44}$$

Where L is the discretisation of the time-differential operator applied to the state vector $U^{n+1/2}$. This technique offers a low computational cost especially when dealing with multi-dimensional evolution as, working with a single step, it has to apply only one Riemann solver per cell and per direction [117].

The method of lines is the classical implementation of the time evolution schemes. It is based on a semi-discrete algorithm which distinguished the time and the space discretisation in to different phases. While the problem is left continuum in time it is discretised in space yielding a set of, easier to integrate, ordinary differential equations (ODE):

$$\frac{dU_j(t)}{dt} = \frac{1}{\Delta x}(F[U(x_{j-1/2}, t)] - F[U(x_{j+1/2}, t)]) + S_j \tag{4.45}$$

The cornerstone method of lines implementation is the Runge-Kutta, which is implemented in PLUTO both at the second and third order in the TVD formulation of [120]. The method is developed as a series of predictor steps which anticipate the final update $t^n \to t^{n+1}$.

The 2^{nd} order RK is formulated as:

$$U^* = U^n + \Delta t L^n \quad predictor \tag{4.46}$$

$$U^{n+1} = \frac{1}{2}][U^n + U^* + \Delta t L^*] \quad update \tag{4.47}$$

The time evolution provided by the $3^r d$ order RK requires instead an extra step:

$$U^* = U^n + \Delta L^n \quad 1^{st}\ predictor \tag{4.48}$$

$$U^{**} = \frac{1}{4}[3U^n + U^* + \Delta t L^*] \quad 2^{nd}\ predictor \tag{4.49}$$

$$U^{n+1} = \frac{1}{3}[U^n + 2U^{**} + 2\Delta t L^{**}] \quad update \tag{4.50}$$

The input states U^n are provided by the interpolation method chosen in the reconstruction. Furthermore, additional informations have to be provided in the form of *boundary conditions* defined just outside the edges of the numerical grid in the so called *ghost zones*. RK methods reaches higher accuracy (even higher than the actual order of implementations for TVD schemes [120]) however they are more expensive than zone-edge extrapolation as they require to solve two (or three) Riemann problem per cell and per direction.

[1] Notice that now working with curvilinear coordinates could introduce additional *geometrical source terms* which should be consistently dealt with [117].

4.3 Radiative module

PLUTO is a multi-physics, modular code which allows to select the better configuration to describe the problem at hand and then to integrate it in the more appropriate way. In particular, a module for the treatment of radiation transport in relativistic hydrodynamics was implemented in [108]. The numerical scheme is based on the resolution of the RAD-RHD equations as derived in Chapter 3, which can be here summarized as:

$$\frac{\partial U}{\partial t} + \nabla \cdot (U) = S(U) \tag{4.51}$$

Where now the state the radiative energy and fluxes are added to the state vector: $U = (\rho\gamma, E, \boldsymbol{m}, E_{rad}, \boldsymbol{F}_{rad})$ and the source S is not zero but contains the radiation-matter interaction terms $(G^0, \boldsymbol{G})$.

The numerical algorithm required to tackle the RAD-RHD problem differs from the one applied to the RHD system alone precisely due to the presence of the interaction terms. In fact their timescales may be a lot shorter than the typical timescales involved in the pure dynamical evolution, hence a non-trivial treatment of the timestep is required. This kind of problems are called *stiff* and can be summarized as:

$$\partial_t U = Q(U) + \frac{1}{\tau} R(U) \tag{4.52}$$

Where Q and R are both discretised, spatial differential operators and τ is the relaxation timescales. In the limit $\tau \to 0$, $R(U) >> Q(U)$ and the two terms are described by very different speeds. Explicitly integrate both term together would require an overwhelming amount of time and resources and may rise strong instabilities. For this reason stiff problems required to be tackled with a hybrid schemes which handles differently the two different contributions. This class of methods is called IMEX-RK [121] and it's based on the appropriate implementation of explicit and implicit Runge-Kutta schemes. When applied to the system 4.52 it reads:

$$U^{(1)} = U^n + (1 - \frac{\sqrt{2}}{2})\Delta t^n S^{(1)} \tag{4.53}$$

$$U^{(2)} = U^n + \Delta t^n R^{(1)} + \Delta t^n [1 - \sqrt{2} S^{(1)} + (1 - \frac{\sqrt{2}}{2}) S^{(2)}] \tag{4.54}$$

$$U^{n+1} = U^n + \frac{\Delta t^n}{2}[R^{(1)} + R^{(2)}] + \frac{\Delta t^n}{2}[S^{(1)} + S^{(2)}] \tag{4.55}$$

Where the flux contribution has been approximated by: $R \approx -\nabla \cdot F$ and operator S includes the stiff terms which depends on the opacity coefficient.

Then the terms in the RHS that drive the evolution timestep of the state vector are integrated implicitly while the rest is dealt with explicitly.

4.3.1 Explicit Step

In the explicit step the system is integrated according to the techniques described in the previous section, taking $S = 0$. In this way the RAD-RHD system can be separated into two independent subsystems in which the respective variables are evolved without affecting each other. Furthermore, each subset of equations uses its own, derived. characteristic speeds, this allows to reduce the numerical diffusion, as tested in [108].

In order to compute RHD and RAD fluxes an approximate Riemann solver has to be implemented. For the latter, an additional radiation-oriented HLLC solver has been implemented, however it has been shown that it is able to improve the accuracy only in the optically thin regimes hence, for the problem tackled in this work, the standard HLL solver has provided the best performances.

4.3.2 Implicit step

The interaction between matter and radiation requires to be treated through an implicit integration. From the IMEX equations [4.53-4.59] it is possible to retrieve the general formulation for the implicit step:

$$U = U' + s\Delta t^n S \tag{4.56}$$

Where the primed notation refers to some intermediate predictor level and s is a numerical constant. Equation 4.56 expresses the conservation of the rest mass and of the total energy and momentum densities, thus one can write:

$$E_{tot} = E + E_{rad}, \qquad \boldsymbol{m}_{tot} = \boldsymbol{m} + F_{rad} \tag{4.57}$$

These uniquely relate the matter field (in the primitive variables V) to the radiation field U_{rad}. [2] Therefore the total system of 4.56 can be solved in terms of the reduced system:

$$U_{rad} = U'_{rad} - s\Delta t^n G \tag{4.58}$$

With $U_{rad} = (E_{rad}, \boldsymbol{F}_{rad})$ being the radiation state vector.

In 4.58 the RAD terms can be expressed as functions of RHD ones and vice versa so the system is non-linear and to solve the equations a (multidimensional) root finding algorithm must be implemented. The module provides three of them

Fixed-point method This method follows the approach developed in [122] and consists in finding the solution by iterating on the U_{rad}. First the system is rewritten, for a generic iteration m as:

$$G^{(m)} = M^{(m)} U_{rad}^{(m+1)} + b^{(m)} \tag{4.59}$$

Where M is a matrix and b a vector, both depending on the primitive fields and are evaluated at an iteration before with respect to U_{rad}. Then it is possible to obtain the update state by substituting this expression in 4.58:

$$U_{rac}^{(m+1)} = (I + s\Delta t^n M^m)^{-1} (U'_{rad} - s\Delta t^n b^{(m)}) \tag{4.60}$$

From this the primitive fields can be computed again by inverting relations 4.57 and the algorithm goes on until the difference between the initial field and the last updated is below a certain threshold.

Newton's method for radiation fields This method was first implemented in [123], instead of operating directly on the state vector it consists in iterating over a non-linear function which depends on the radiation field:

$$Q(E_{rad}, \boldsymbol{F}_{rad}) = U_{rad} - U'_{rad} + s\Delta t^n G \tag{4.61}$$

To do so, at each step the new variables are computed from the previous ones by:

$$U_{rad}^{(m+1)} = U_{rad}^{m} - [J^{(m)}]^{-1} Q^{(m)} \tag{4.62}$$

Where $J = J_{ij} = \partial Q_i / \partial U^j$ is the Jacobian of the non-linear function which elements are numerically determined. Again, the matter fields are obtained by inverting 4.57.

[2] Notice that while the primitive and the conservative variables of the RHD system are different, this isn't true for the radiative variables which are the same in both the formulations

Newton's Method for matter field This implementation [124] is analogous to the previous one with the difference that now the iteration is performed on the RHD fields: W = (p,**u**) and so now the Jacobian is computed as $J_{ij} = \partial Q^i / \partial W^j$. This method turns out to be actually faster than the previous ones since the radiation fields can be directly obtained from W without having to first invert the conserved fields.

The fixed point method seems to converge faster than the Newton ones in which is present the inversion of the Jacobian matrix. However, the latter methods are more stable especially when the difference between E and E_{rad} becomes relevant. When implementing the radiative module is fundamental to choose the right root-finding algorithm according to the problem at hand, or the convergence may be not reached. For example, say that $E << E_{rad}$, then when the radiation field converges the matter one may still present large errors, hence choosing the 2^{nd} method would rise important inaccuracies.

Chapter 5

3D Relativistic Hydrodynamic Jet Simulations

Having introduced the required physical and numerical background of the problem, now it is time to actually present the carried out work along with the obtained results. The final aim is to find and develop a procedure which allows us to consistently study the photospheric (thermal) emission from the jet at different viewing angles (with respect to the jet propagation axis). To do this, we have chosen to start by using a realistic jet prescription as initial data, building on the results already obtained by the group in [82]. In that work, the authors were able to successfully insert a jet prescription into a BNS merger environment previously obtained in a non magnetized version of the GR BNS merger simulations of [30], thereby obtaining the very first jet evolution with 'realistic' surrounding environment. Since the simulations of [82] were performed in PLUTO, we could directly start from those results to include the radiation and thus tackle our goal.

At the scales of jet launching and break-out the optical depths are rather high. There the fluid is assumed to be in the condition of local thermal equilibrium (LTE) with the radiation, i.e. with all the photons trapped inside the matter. In this regime makes little sense to apply the radiative module. However, as the outflow propagates radially outward, its density decreases and the material becomes gradually more transparent to the radiation. The first step of the present work, then, consisted in extending further the evolution of the propagating jet at larger radii and at later times (up to 10^{11-12} cm, around ~ 6 to 7 s after merger) with respect to the fiducial simulation already performed in [82], which was limited to 1 s after merger only.

This has been accomplished using again the RHD PLUTO module to perform a 3D evolution of the bulk region of the jet (or 'head' of the jet). At these distances, the influence of the central engine and of the dynamics at smaller radii is negligible, which allows us to 'excise' or cut out a large portion of the inner regions to reduce the required computational cost (see details below). This type of 3D simulations have been performed on the CINECA HPC cluster Galileo100[1].

In this Chapter, the derivation of the initial condition then used for the radiative problem will be explained. In Section 5.1 and 5.2 we present the results of [82] used as initial data for our further runs, while in Section 5.3 and 5.4 we discuss the 3D hydrodynamical simulations performed in this work.

[1] https://www.hpc.cineca.it/

5.1 Setup

The reference BNS merger simulation considered in [82], corresponding to a non magnetized version of the simulations presented in [30], had a chirp mass of the system adjusted to match the one measured for GRB 170817A and a mass ratio of $q = 0.9$ (hence considering a nearly equal-mass binary). It produced a long-lived massive NS remnant with mass $\sim 2.596 M_{\odot}$, which was evolved up to 156 ms after merger. In order to inject an ultra-relativistic jet according to the standard accreting BH scenario (favoured as SGRB central engine, see chapter 2), the authors of [82] assumed the remnant collapse to a BH at a given time, chosen as a parameter. For their fiducial model, they set the collapse 101 ms after merger, also corresponding to the time at which data where taken/imported from the original BNS merger simulation, before starting the RHD evolution in PLUTO. After a short time window of order 10 ms, accounting for the effects of the collapsing BH on the inner environment, the jet was injected.

The selected BNS data (3-velocity, density and pressure) had to be interpolated into the PLUTO computational grid, which has been done through the PostCactue Python package[2], a tool for the management and the post-production for Einstein toolkit results. Whereas the data from the BNS simulations were obtained in a 3D Cartesian grid with imposed symmetry on the equatrial plane, a jet evolution is better handled by using a spherical system of coordinates (r, θ, ϕ), in a full 3D domain. Furthermore, to avoid effects on the jet evolution due to the polar axis singularity of spherical coordinates, the latter were tilted by 90 degrees, so that BNS orbital axis (or jet propagation axis) and polar axis of the grid resulted orthogonal.

The PLUTO spherical grid was fixed to be homogeneous in the angular directions, but logarithmic in the radial one, allowing one to cover long distances while saving computational resources and still resolving well the inner region close to the remnant. The equatorial angle θ was defined in the range $[0.1 - \pi - 0.1]$ to avoid the polar singularity, while the azimuthal one, ϕ, lied between $[0 - 2\pi]$. The radial, r, coordinate was instead initialized in the range $[380 - 2.5 \times 10^6]$ km, where the distances are measured with respect the remnant's center of mass. With this choice, all the region within 380 km radius was not evolved, but simply *excited* spherically with radius $r_{exc} = r_{min}$. This procedure yields the following advantages:

- It allows one to ignore the central engine evolution which would require an high level of resolution, but at the same time it doesn't crucially affects the jet propagation.
- It allows one to ignore general relativistic effects, hence justifying the special relativistic HD approach.

We refer the reader to [82] for details on the boundary conditions and the special treatment of the post-collapse phase prior to the jet launching.

For the resolution, it was chosen a setup with $756 \times 252 \times 504$ points in r, θ, ϕ respectively (see the Appendix of [82] for a resolution study). For the logarithmic spacing in r, the variable spacing is given by

$$\Delta x_i = \left(x_{i-\frac{1}{2}} + |x_L| - x_L \right) (10^{\Delta\xi - 1}), \qquad \Delta\xi = \frac{1}{N} log_{10} \left(\frac{x_R + |x_L| - x_L}{|x_L|} \right) \tag{5.1}$$

where N is the total number of points in the radial direction, i is the index referred to the cell-center value of the point x and x_L, x_R are the grid edges. In this way, at the smallest radius (380 km) the resolution is $\Delta r \sim 4.4$ km, $r\Delta\theta \sim 4.4$ km and $r\Delta\phi \sim 4.7$ km.

In order to close the system of RHD equations, an EOS needs to be chosen. In [82], the one adopted is the TAUB EOS [125], first implemented in [126]. In said work the authors derived a numerical formulation for the EOS based on the closure relations first derived by [127].

[2] https://github.com/wokast/PyCactus

According to the relativistic kinetic theory of gasses the specific enthalpy h of the system should be a function of the temperature $\Theta = P/\rho$ in such a way that the TAUB fundamental inequality is satisfied:

$$(h - \Theta)(h - 4\Theta) \geq 1 \tag{5.2}$$

This sets constraints on the definition of whatever EOS expressed in terms of the specific heat ratio (or 'adiabatic index') γ which in turn has to reduce to a constant value law when limiting to the very high or very low temperatures. In [126] it was shown that a smooth EOS covering the whole range of physical temperatures can be formulated as

$$\gamma_{eq} = \frac{h - 1}{h - 1 - \Theta} \tag{5.3}$$

where γ_{eq} is the numerically approximated values of γ which, as it turns out, differ from the true one by only less than the 4 per cent. Moreover, it was shown that by taking 5.6 with the equal sign, the EOS can be formulated in terms of the enthalpy as:

$$h = \frac{5}{2}\Theta + \sqrt{\frac{4}{9}\Theta^2 + 1} \tag{5.4}$$

Which reduces to the limits:

$$\lim_{\Theta \to 0} \gamma_{eq} = \frac{5}{3}, \qquad \lim_{\Theta \to \infty} \gamma_{eq} = \frac{4}{3} \tag{5.5}$$

For intermediate values of temperatures, the TAUB EOS allows for the hydrodynamic quantities to have smooth variation within the physical range.

Another important element of the simulation is the artificial density and pressure floor or 'atmosphere', necessary to maintain the stability of the code. While in the BNS simulation such a density floor was set to a uniform value of $\sim 6 \times 10^4$ g/cm^3, the jet simulation requires the propagation up to orders of magnitude larger scales and to avoid significant effects of the floor on the jet evolution a much lower level has to be imposed. In particular, in [82] the exact data from the BNS merger were imported in the regions $r_{exc} < r < 1477$ km and at larger radii the velocities were set to zero and the density and pressure floors were replaced with power law profiles $\propto r^{-\alpha}$ up to the outer end of the domain. The fiducial jet simulation of [82] employed $\alpha = 5$.

It should be noted that the artificial density/pressure floor is a particularly critical aspect of the investigation presented in this Thesis, since the details of the outer layers of the jet outflow can have an influence on the emitted radiation (see Section 5.4). For this reason α should be treated as a free parameter of the problem and any artificial effects isolated by comparing the results obtained with different atmoshere levels.

Figure 5.1 shows a meridional view of the rest-mass density at the data import (or remnant collapse) time, comparing the original BNS merger data with the PLUTO setup resulting from the import procedure (including the interpolation on new coordinates and the redefinition of the atmosphere level).

Concerning the numerical methods for RHD, the fiducial simulation of [82] was carried out employing a RSA strategy characterised by a piecewise parabolic reconstruction, the HLL as Riemann solver and the 3^{rd} order Runge-Kutta to update the solution (time stepping). Other details can be found in [82].

As final note, the simulation included the (Newtonian) gravitational pull from the central object, representing an important ingredient as demonstrated in [82].

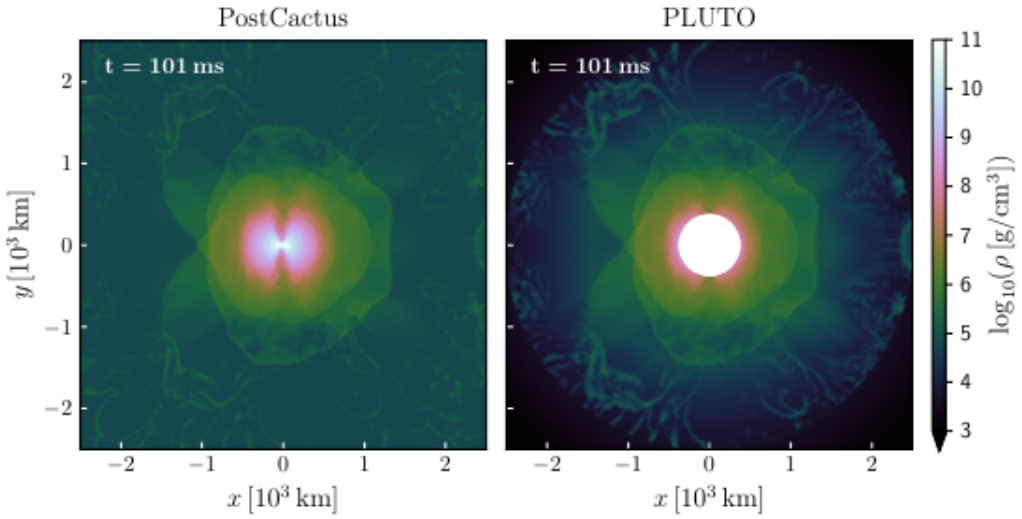

Figure 5.1: Meridional view of the rest-mass density at the moment of data import or, equivalently, in which the collapse to a BH is assumed to occur ($t = 101$ ms). *Left* and *right* panels compare the original BNS merger data as retrieved via PostCactus on a uniform Cartesian grid to the PLUTO setup obtained by interpolating on the new (tilted) spherical grid, by redefining the artificial atmosphere, and by excising the inner region (below a radius of 380 km).

5.2 Jet Injection and evolution

The jet was injected 112 ms after merger, along the y-axis (corresponding to the BNS orbital axis), both in the positive and negative directions, and according to a simple top-hat model within a half-opening angle of 10 degrees. The injection was realized by imposing suitable radial boundary conditions at the excision radius (380 km). The authors chose a set of injection properties in agreement with the typical parameter ranges used in the literature ([81] for example). Free parameters of the problem are:

- **Lorentz factor:** The terminal Lorentz factor is defined as $\Gamma_\infty = h_0\Gamma_0$, where the RHS terms are respectively the specific enthalpy and the Lorentz factor at the injection time. The incipient jet was set with $h_0 = 100$ and $\Gamma_0 = 3$, yielding $\Gamma_\infty = 300$. The velocities at the excision were then derived from Γ_0;
- **Luminosity:** The initial jet power is given by:

$$L_0 = 4\pi r_{exc}^2 \int_0^{\alpha_j} (h_0\Gamma_0^2\rho_0 c^2 - P_0) v_0 sin\alpha' d\alpha' \stackrel{!}{=} 3\times 10^{50}\,\mathrm{erg/s} \tag{5.6}$$

  where α_j is the jet half-opening angle and α is the angle with respect the orbital axis, while ρ_0 and P_0 are the (uniform) density and pressure within the injected outflow. Choosing a value for L_0 allows to fix ρ_0 (while P_0 is fixed via the EOS).

At 112 ms from the merger (time of jet launching), a slowly expanding baryonic wind was already expelled by the post-merger system and had propagated outwards with a velocity of $\sim 0.07c$, reaching a distance of $\sim$ 2000 km (see Fig. 5.2, left panel). The overall amount of mass in the wind was about $\sim 0.02M_0$, consistent with the typical range of ejected material during a BNS merger (Chapter 1), with the majority of the material concentrated in the inner radii, i.e. $r \leq 500$ km. Moreover, the baryonic wind showed an irregular density distribution characterised by the presence of a lower density funnel along the y-axis, which is important for the following emergence of an incipient jet. It should be noted that the collapse time is a crucial

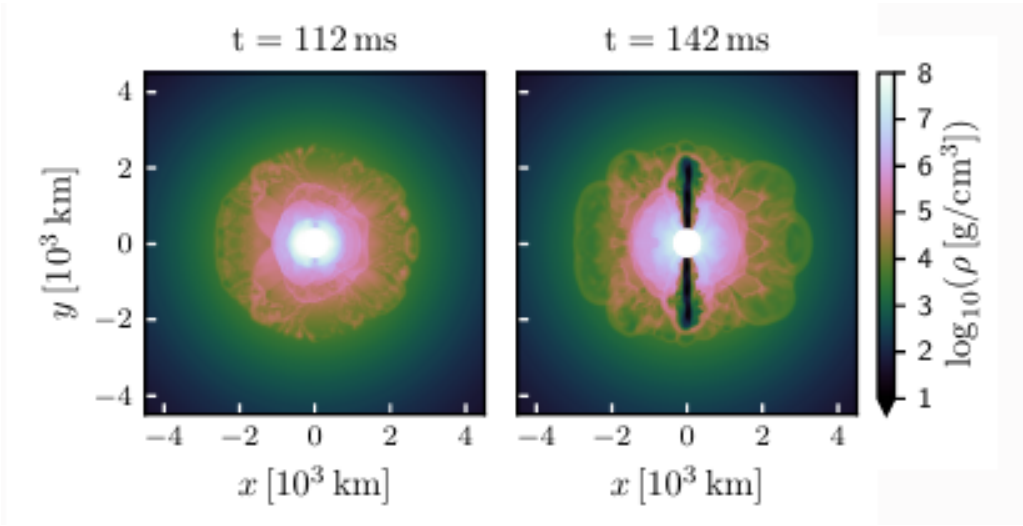

Figure 5.2: Evolution snapshot of rest-mass density (meridional view) at the time of jet injection and at the jet breakout time. At 112 ms the presence of a low density funnel can be appreciated above the polar regions favouring the jet launching. Then, after 30 ms the successful jet has drilled through the BNS environment material.

free parameter. Indeed, a later collapse would increase the amount of baryon wind material encountered by the jet, hence producing a larger collimation, but also increasing the probability that the jet itself will be choked.

Soon after the time of jet launching, about 30 ms, the latter propagates up to the outer border of the dense cloud of material surrounding the central object, thus breaking out and starting to propagate in the outer medium (Fig. 5.2, right panel). During this process some of the initial energy is deposited in the slower side wings of the jet, leading to the formation of a surrounding, hot cocoon and of a complex angular structure.

At the end of the simulation, at 1012 ms from the merger, the outflow reached about $\approx 2.7 \times 10^5$ km, directed slightly off-axis, at $\sim 0.8°$ with respect the injection direction. The jet structure was composed by a well distinguished, ultra-relativistic head, which contained the bulk of the jet energy and it was associated to a Lorentz factor of $\Gamma \sim 40$, separated by a slower, wide and rather turbulent tail (see Fig 5.3).

5.3 Further jet evolution

The end of the fiducial simulation of [82] represents the starting point of the present Thesis work. At 1012 ms, the densities are still high enough to enforce a LTE regime and to prevent the decoupling between photons and matter. Therefore, to study the photospheric (thermal) radiation emitted by the jet's head, we first need to further evolve the system up to much larger distances.

With the setup described in the previous Sections, the simulation covering about 1 second of evolution was computationally rather expensive and took a long time to complete. Moreover, for what concerns the radiative signal we are interested in, the important part is the jet's head, were most of the energy (including internal energy) resides. For these reasons, we can save time and computational resources by continuing the evolution after having excised a much larger inner sphere, which in turn implies that we are significantly reducing the number of grid points. Specifically, the new radial grid is set to cover $r \in [1.5 \times 10^5 - 2.5 \times 10^6]$ (see Fig. 5.4), and, in order to fill the entire domain, the atmospheric floor profile with $\alpha = 5$ is continued. In doing so, the new number of points associated to the radial direction should be properly computed to guarantee a perfect superposition of old and new grid points. This can be performed by inverting

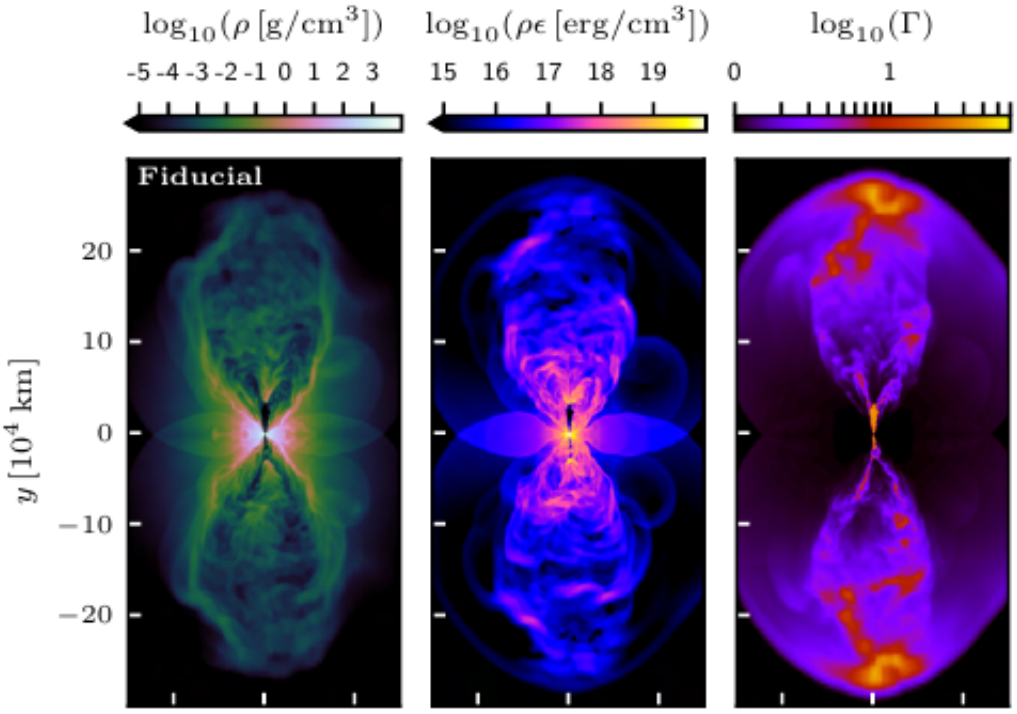

Figure 5.3: Meridional snapshots of rest-mass density (left), internal energy density (center), and Lorentz factor (right), at 1012 ms after merger. It is possible to notice the development of an angular structure composed by a relativistic, slightly off-axis head (right panel) on the top of a rather turbulent and slower tail. At 1012 ms, the jet clearly exceeds the 2×10^5 km of distance from the central engine.

5.1:

$$N = \frac{log_{10}\frac{x_R}{x_L}}{log_{10}\frac{\Delta x_{min}+x_L}{x_L}} \tag{5.7}$$

where Δx_{min} is the distance between the point corresponding to the new smallest radius and its adjacent in the old grid. By substituting the new edge values we found that the best match is provided by $N = 241$ points in the radial direction. As a consequence, the new number of grid points is reduced by a factor ~ 3 with respect to the old one.

Proceeding in this way, we obtained the initial data for the further jet evolution run. The inner radial boundary conditions for the new run do not have any impact on the final results (also because the jet's head is travelling faster, at velocities near the speed of light) and are simply set to the no-gradient (or 'outflow') condition.

The first run was carried out with the RHD PLUTO module, in a very similar way to the [82] simulation, adopting the same RSA procedure. As a result we produced (rather quickly) almost 1 second of additional evolution (see Fig. 5.5), after which another cut was required to further extrapolate the jet bulk at even larger distances. This time the minimum radius was placed at $\approx 3.7 \times 10^5$ km, further reducing the number of points in the radial direction to $N = 163$.

The second run allowed us to reach up to almost 7 seconds after merger Fig. 5.6. As expected, with the adopted setup, the jet propagates at ballistic proportions with the radial motion being the dominant one. We note that the jet's head, even at those much larger distances, still preserves many irregularities, which are imprinted in the final escaping radiation.

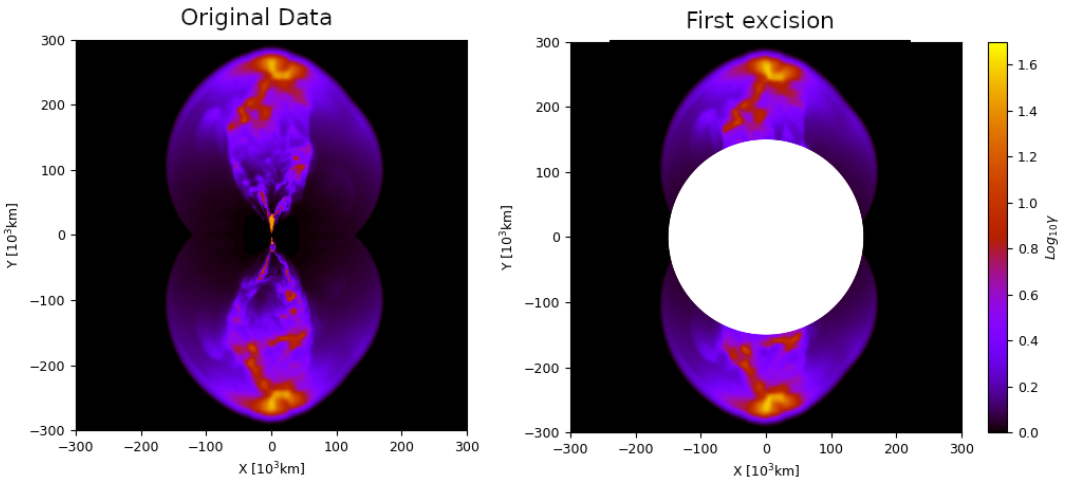

Figure 5.4: 2D meridional view of the Lorentz factor (log scale) at 1012 ms after merger for the fiducial simulation of [82], before (left) and after (right) extending the excision radius from 380 km to about 1.5×10^5 km.

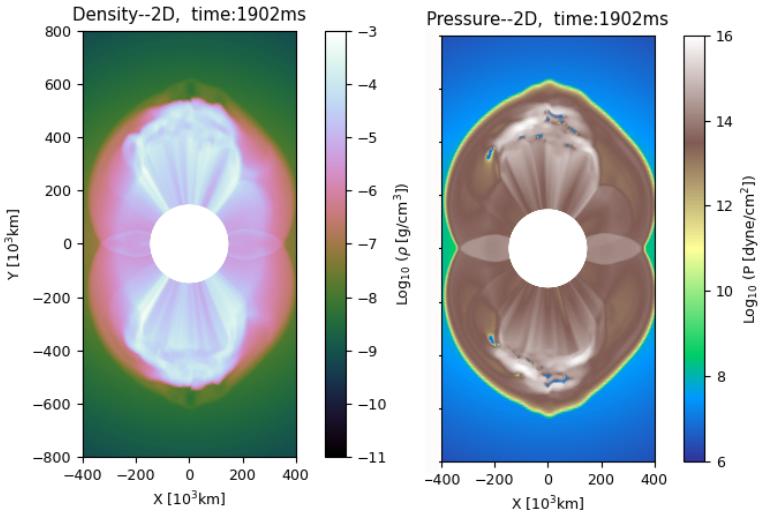

Figure 5.5: 2D meridional view of rest-mass density (*left*) and pressure (*right*) at 1902 ms after merger.

5.4 New Atmosphere

In Fig. 5.6 it's possible to notice the presence of a non zero pressure contribution ahead of the jet bulk. In the real physical scenario, after the breakout from the BNS environment, the jet's head should encounter only an extremely low-density ISM material. However, the presence of a smoothly declining artificial floor may rise spurious effects which occur in the form of clumps of compressed matter that are built at the jet front. The density floor is an artificial approximation required to make the simulation work, and its presence may lead to unwanted effects when investigating the emitted radiation (see Chapter 6).

In order to quantify the impact of the artificial atmosphere on our final results, we have chosen to carry out an extra simulation with the same setup previously described but changing the floor decreasing exponent to $\alpha = 5.5$. It should be noted that a similar evolution was already carried out up to 762 ms after merger in [82] (as reported in their Appendix). In the current work, we have first continued that run up to 1012 ms (see Fig. 5.7) and then we have applied the same procedure as for the fiducial run (i.e. moving the excision radius outwards and continuing the evolution), this time reaching up to almost 8 s (Fig. 5.8).

At 1012 ms, the two setups with different atmospheric floor show a rather similar profile, with the main difference being the development, in the new run, of a more isotropic and slightly less collimated structure (Fig. 5.7). However, despite the differences seems to be minor at smaller times, at larger distances the atmospheric contribution becomes more and more important: the relativistic jet's head compresses and accumulates atmospheric material in its outward layers, which is also hot and, as a consequence, can provide a non-negligible (unwanted) contribution to the energy that can in principle be radiated away by the system. At ~ 8 s, the domain is entirely covered by the jet expansion, thus border effects are expected to manifest (Fig. 5.8). This already suggests that the following investigation steps should better consider the final state of the system some time before 8 s.

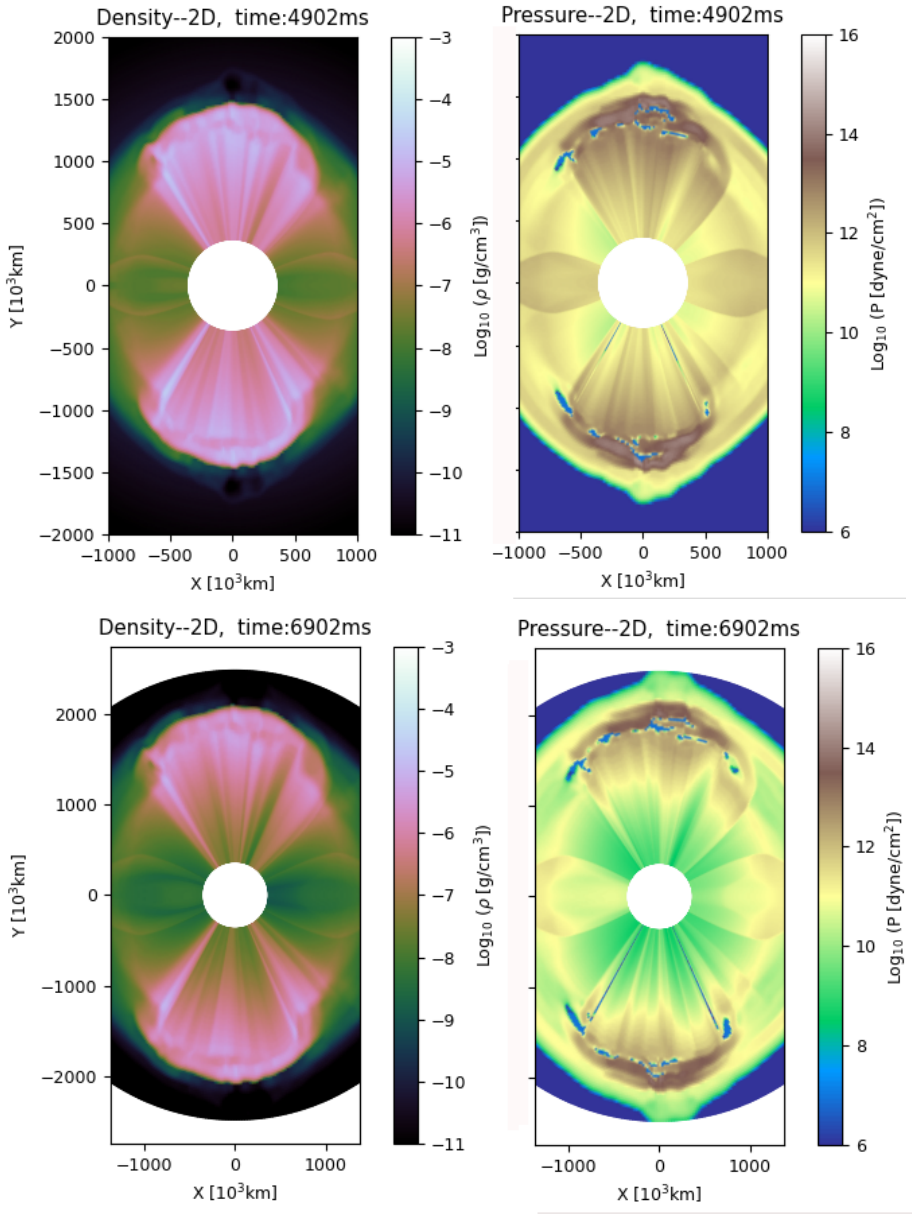

Figure 5.6: 2D meridional view of rest-mass density (*left*) and pressure (*right*) at 4902 ms (top) and 6902 ms (bottom) after merger.

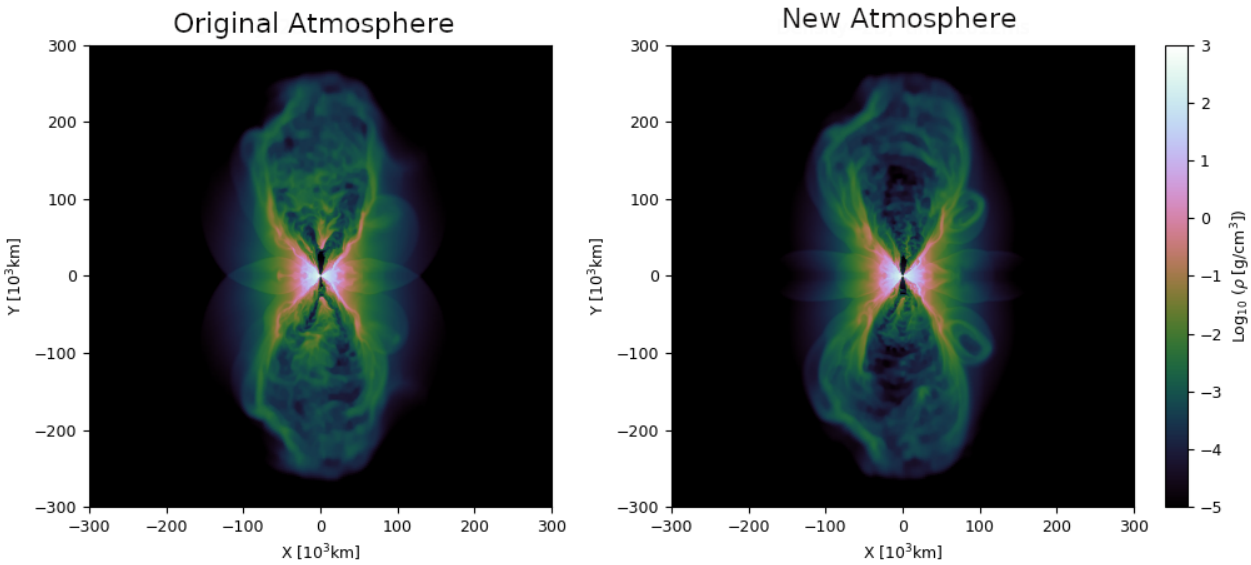

Figure 5.7: 2D meridional view of rest-mass density at 1012 ms after merger. *Left:* fiducial simulation of [82] with $\alpha = 5$. *Right:* the new simulation carried out with $\alpha = 5.5$.

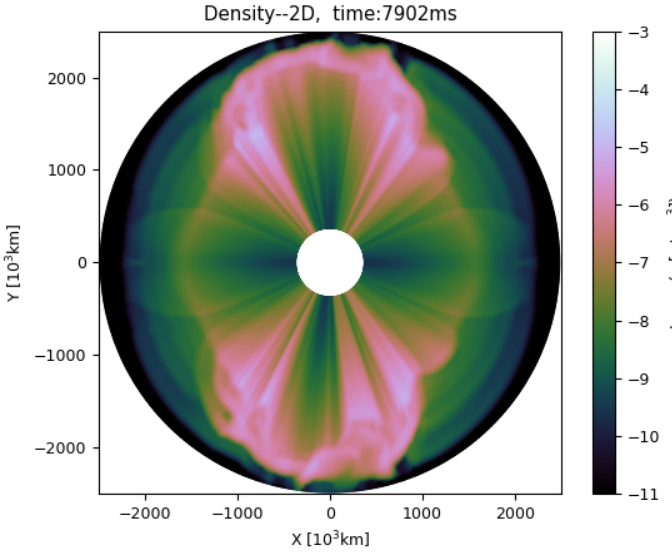

(a) 2D log rest-mass density map

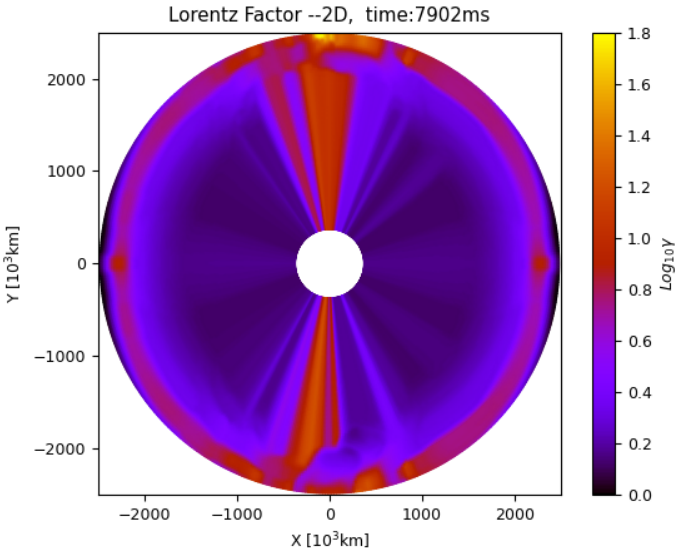

(b) 2D log Lorentz factor map

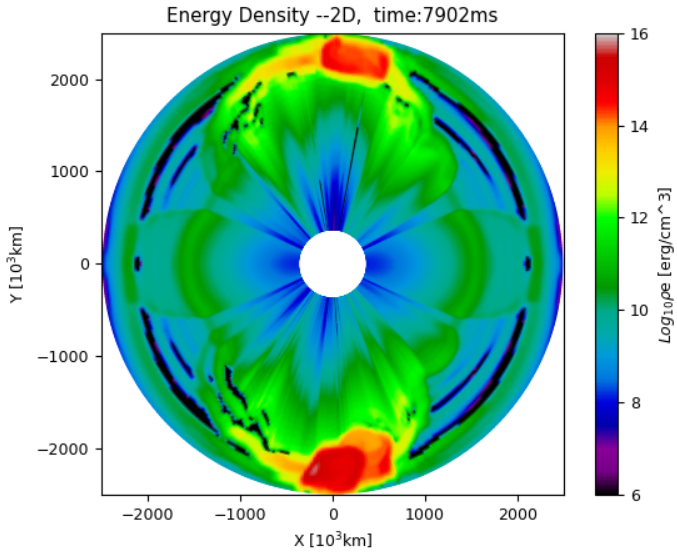

(c) 2D log internal energy density map

Figure 5.8: Final state of the case with new atmospheric floor level at about 8 s after merger, described by 2D meridional view panels of rest-mass density, Lorentz factor, and internal energy density.

Chapter 6

Evolution with radiation transport

The output from the 3D RHD simulations described in the previous Chapter is the starting point to further evolve the system with the inclusion of radiation transport. Nevertheless, the high opacity of the system requires to reach much larger times (or distances from the central object) before it becomes useful to add the radiative contribution. To achieve this, we chose to reduce the complexity of the problem by focusing on the 1-dimensional profile evolution along a chosen radial direction. Then, after a further 1D hydrodynamic evolution (very fast and computationally cheap), we were finally able to successfully activate the PLUTO radiative module. The time at which we move from 3D to 1D evolution and the time at which we introduce the radiative contribution are parameters of the treatment, whose impact needs to be assessed. The final result, given in terms of lab-frame isotropic equivalent luminosity of the photospheric (thermal) emission as measured by a distant observer, also depends on main physical parameters like the chosen direction and the chosen opacity of matter.

To the best of our knowledge, this is the first application of a two-moment radiation transport scheme in RHD simulations of jets in the context of SGRB/BNS mergers. The present work is mostly focused on establishing the correct procedure and deriving a first set of physical results. The outcome of a direct comparison with the prompt emission of GRB 170817A bodes well for the future viability of the developed framework.

First, we discuss the setup of the radiative problem, describing the adopted approach (Section 6.1). Then, in Section 6.2 we discuss a fiducial model and the optimal setup of the various parameters of the treatment (including the spatial resolution to be adopted in the 1D evolution), while in Section 6.3 and 6.4 we report our results along with the comparison with GRB 170817A.

6.1 Setup and Procedure

The crucial quantity which describes how strong is the light-matter coupling over a certian region of space (or, in our case, radial interval) is called *optical depth* and can be defined as the adimensional number:

$$\tau = \int_{r_{in}}^{r_{end}} \rho(r)\kappa dr \tag{6.1}$$

where κ is the material's opacity coefficient, r_{in} is the inner radius of the integration and r_{end} the outer boundary of our domain. The *photospheric* radius is defined as the r_{in} of the above expression such that $\tau = 2/3$. Above such a radius light is essentially decoupled from matter and can freely stream outwards (towards a distant observer).

At $[5-8]$ s after merger (time reached in our extended 3D RHD jet simulations, see previous Chapter), τ computed from the latest excision radius ($\approx 3.7 \times 10^5$ km) up to the end of our domain, comprising the whole relevant part of the propagating jet, is of order $O(10^5)$. Now, even if the PLUTO radiative module was implemented to work in both the optically thin and thick

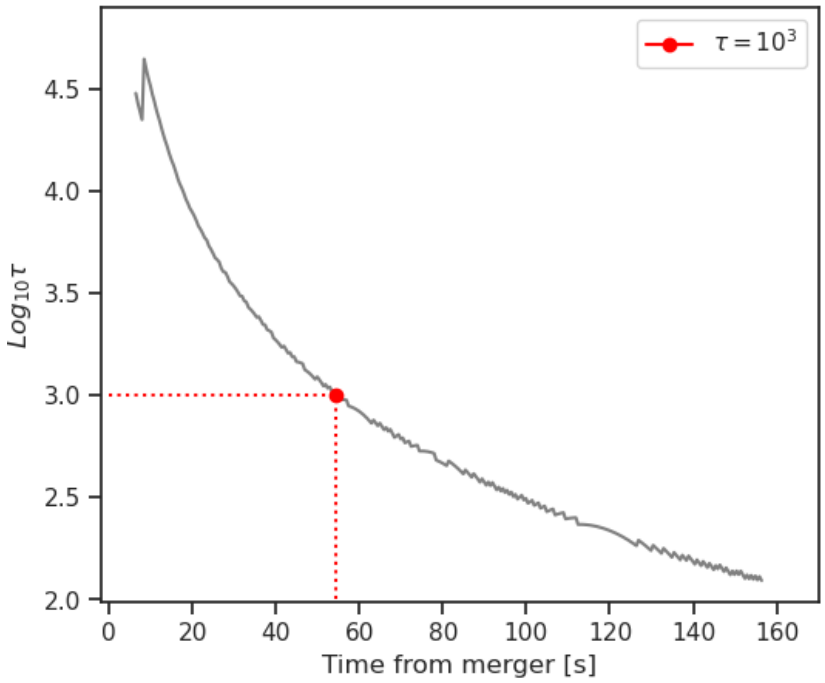

Figure 6.1: Time evolution of (log-scale) optical depth computed via Eq. (6.1) by setting r_{in} as the radial location of the maximum density. τ becomes order 10^3 or lower only at times later than ~ 50 s after merger.

regimes, it was tested only for total opacities up to $\tau \sim O(10^3)$, which are still large enough to enforce a quasi-LTE condition in the system. For this reason, we had to evolve our system much further before introducing the radiation transport.

6.1.1 RHD evolution in 1D

While a 3D evolution is crucial to conserve in full the realistic structure of the propagating outflow, performing multi-dimensional simulations is a rather expensive task which can hardly be sustained for the times and distances needed in out investigation. As shown in Fig. 6.1, the ideal regime for the radiative module implementation is reached only after ~ 50 s, which we could not cover with a 3D simulation. For this reason, we have decided to continue in 1D for different chosen directions (corresponding to different observer viewing angles). The time at which we switch to the 1D evolution, namely t_{1D}, is a parameter of the treatment.

We notice that already after a few seconds (see for example Fig. 5.8) the jet head propagation is dominated by the relativistic radial motion and is no longer strongly affected by the transversal components. This makes the approximation of a 1D evolution reasonable. Nonetheless, investigating the impact of different t_{1D} is necessary (see Section 6.2.1).

In order to extract a 1D profile from the original data we chose to fix the meridional plane, $\theta = 90°$ (we recall that the spherical coordinates are tilted, so that $\theta = 90°$ corresponds to a plane containing the jet propagation direction) and vary ϕ to consider different viewing angle with respect to the jet axis (in particular, we consider 15° and 25°). As a reference, GRB 1780817A was observed 15-30° away from the jet axis.

As can be seen in Fig. 6.2a, in doing so the velocity vector is reduced to the only radial component and we obtain profiles that vary along the radial coordinate. The new initial data was then easily evolved up to ~ 150 s, eventually ending up in the suitable optical regime for the inclusion of radiation.

Now, while the interaction of the incipient jet with the surrounding post-merger environment

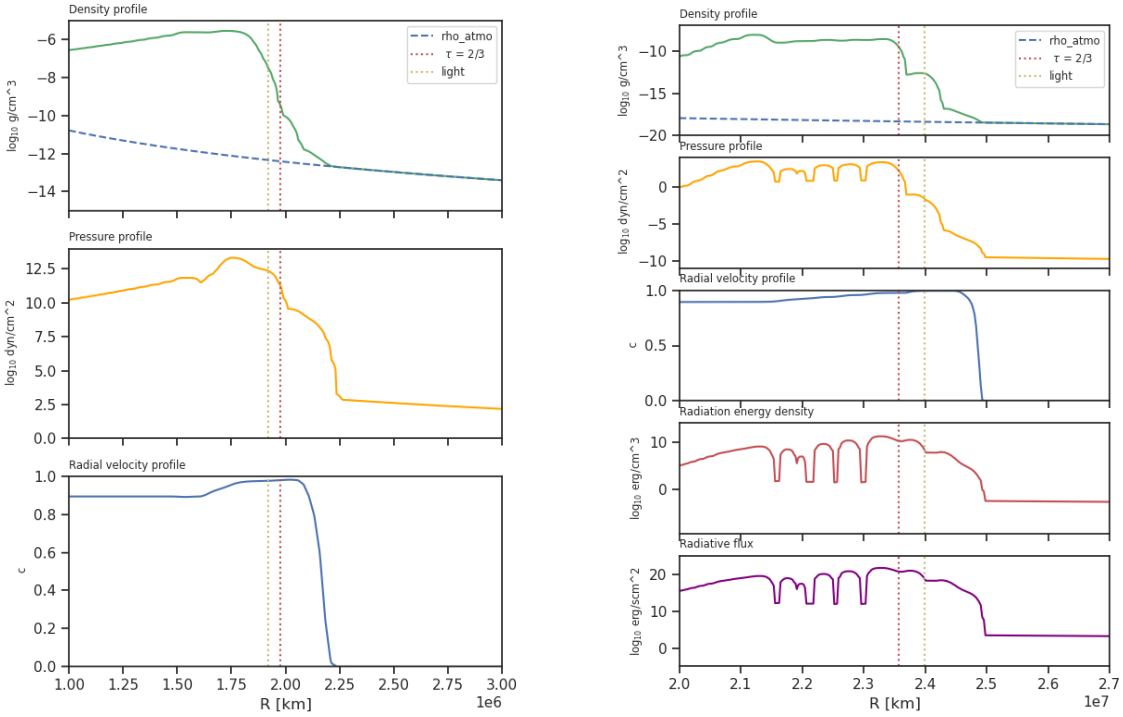

(a) 1D RHD Initial data

(b) 1D RAD-RHD Initial data

Figure 6.2: *Left:* Initial data as extracted from the 3D jet profile along the chosen direction (see text). *Right:* Data obtained after a time t_{rad} of 1D hydrodynamic evolution, setting the beginning of the evolution including radiation. In all panels, the blue dashed line illustrates the atmospheric floor that scales as $r^{-\alpha}$, whereas the vertical, yellow, dashed line indicates the photon radius (i.e. the distance reached at speed c since the merger time.). This can be used to discriminate the physical contributions from artificial superluminar ones raised by the atmospheric floor. Lastly, the dotted red line marks the location of the photosphere, i.e. the radius where the optical depth is $\tau = 2/3$.

(and in particular its breakout) is what powers the ultimate photospheric emission we are studying, the high opacities (and thus optical depths) keep the radiation fully coupled with the jet material moving at relativistic speed for a rather long time. As fast as the jet can be, it cannot exactly match the speed of light, hence the outflow's front accumulates a delay with respect to the the photon radius, as can be seen in Fig. 6.2. There the vertical, yellow, dashed line indicates the distance covered by a hypothetical photon emitted right after merger. We note that, as the gravitational waves travel with the same speed of E.M. perturbations, the photon radius indicates also the distance covered by the GW signal.

In the same Figure the dotted red line marks the location of the jet's photosphere which is found by finding the r_{in} in the integral (6.1) that gives $\tau = 2/3$. While initially the photosphere falls above the jet head (Fig. 6.2a), after $\sim 100s$ of evolution it recedes close to the jet front. This is the ideal time to activate the radiative module and to start studying the propagation of radiation from the jet interiors towards the external regions up to the crossing of the photosphere.

6.1.2 Including radiation

In the same way as t_{1D}, the time at which we introduce the radiation t_{rad} is a parameter of the problem that should be explored to check that the final results are not strongly influenced by a specific choice. The smaller t_{rad}, the more precise would be the modeling, but we have to face also the limitations of the radiative module at excessive total opacities. Examples of the convergence of t_{rad} for different models can be found at Fig. 6.7 and Fig. 6.9.

Once we have chosen the time to activate the radiation module, we can define the initial data for the RAD-RHD simulation. As discussed in Chapter 3 and Chapter 4, the radiative module introduces two additional fields to the problem: the radiation energy density E_{rad} and the flux density $\vec{F}_{rad} = (F_r, F_\theta, F_\phi)$, which reduces to the only radial flux in our 1D treatment. This implies the break of the hydrodynamical system's energy conservation and the loss of the LTE condition, since now the photons are allowed to freely propagate outwards. We found that the best way to implement these changes was to preserve the total pressure of the system, P_{tot}, by imposing the old[1] hydrodynamical pressure as equal to the sum of the new gas pressure plus the radiation pressure. In this way, we can write

$$P_{tot} = P_{gas} + P_{rad} \tag{6.2}$$

where P_{gas} is the new gas pressure which should be determined. In the comoving frame, radiation pressure

$$P_{rad} = \frac{1}{3} a T_{rad}^4 = \frac{1}{3} E_{rad} \tag{6.3}$$

will be isotropic (here a is the radiation constant). The hydrodynamical temperature is implemented in PLUTO by means of the ideal gas law

$$T_{gas} = \frac{P_{gas}}{\rho} \frac{m_u \mu}{k_B} \tag{6.4}$$

where $m_u = 1.66 \times 10^{-24} g$ is the atomic mass unit and μ is the mean molecular weight of the gas. According to literature, the regions surrounding the merger site are not homogeneous and due to the emission of anisotropic neutrino winds, the matter composition profiles vary with the angular distribution. Simulations show that a good average for the mean molecular weight in the range [15°-30°] from the jet axis is given by $\mu = 78$ [128]. Assuming that at t_{rad} the LTE still holds, then we have a commmon temperature

$$T := T_{rad} = T_{gas} \tag{6.5}$$

[1] Here 'old' refers to quantities evolved in the pure RHD simulations and 'new' to the quantities obtained after the inclusion of radiation.

and we can rewrite (6.2) as:

$$\begin{aligned} P_{tot} &= P_{gas} + \frac{1}{3}aT^4 \\ &= P_{gas} + \frac{1}{3}a\left(\frac{P_{gas}}{\rho}\frac{m_u\mu}{k_B}\right)^4 \end{aligned} \tag{6.6}$$

Hence the new gas pressure is determined by the relation:

$$P_{gas}^4\left[\frac{1}{3}a\left(\frac{m_u\mu}{\rho k_B}\right)^4\right] + P_{gas} - P_{tot} = 0 \tag{6.7}$$

which is a quartic equation of the form

$$Ax^4 + x - c = 0 \tag{6.8}$$

where A and c are both known as P_{tot} and ρ are directly imported from the old pressure and density respectively. Eq. (6.8) can be solved numerically by implementing a root-finding algorithm, and in particular we have chosen to apply the third order Householder's method which belongs to a family of numerical methods based on the iteration of the equation

$$x_{n+1} = x_n + d\frac{(1/f_n)^{(d-1)}}{(1/f_n)^(d)(x_n)} \tag{6.9}$$

where d is the order of the method and f is a 1D real function so that $f_n = f(x_n)$. By providing an initial guess x_0 close enough to the real solution, the convergence is guaranteed with a rate d+1 [129].

It's easy to see that the first order Householder is just the Newton-Rapson method, in fact for $d = 1$:

$$\begin{aligned} x_{n+1} &= x_n + \frac{(1/f_n)}{(1/f_n)'} \\ &= x_n + \frac{1}{f_n}\left(\frac{-f_n'}{f_n^2}\right)^{-1} \\ &= x_n - \frac{f_n}{f_n'} \end{aligned} \tag{6.10}$$

Instead, by taking $d = 3$ we can easily obtain the third order method by iteratively applying the formula for the derivative of a reciprocal function:

$$\frac{1}{f}' = -\frac{f'}{f^2} \tag{6.11}$$

$$\frac{1}{f}'' = \left(\frac{-f'}{f^2}\right)' = \frac{-f''}{f^2} + \frac{2f'^2}{f^3} \tag{6.12}$$

$$\frac{1}{f}''' = \left(\frac{-f''}{f^2} + \frac{2f'^2}{f^3}\right)''' = -\frac{f'''}{f^2} + 6\frac{f'f''}{f^3} - 6\frac{f'^3}{f^4} \tag{6.13}$$

Hence, after some straightforward algebra:

$$\begin{aligned} x_{n+1} &= x_n + 3\frac{(1/f_n)^{(2)}}{(1/f_n)^(3)} \\ &= x_n + h_n\frac{1 + \frac{1}{2}\frac{f_n''}{f_n'}h_n}{1 + \frac{f_n''}{f_n'}h_n + \frac{1}{6}\frac{f'''}{f'}h_n^2} \end{aligned} \tag{6.14}$$

where $h_n = -f_n/f'_n$. This method was particular suited for the solution of the polynomial equation 6.8 since its derivatives were quite easy to compute.

After having obtained the new gas pressure is then possible to compute the temperature and derive the radiation energy density in the comoving frame. Moreover, as described in Chapter 3, the radiative module requires the radiation fields to be initialized in the Eulerian frame, therefore a Lorentz boost should be applied:

$$\bar{E}_{rad} = \gamma^2 \left(E_{rad} + 2 v_i F^i + v_i v_j P^{ij}_{rad} \right) \tag{6.15}$$

$$\bar{F}^i_{rad} = \gamma^2 v^i E_{rad} + \gamma \left[\delta^i_j + \left(\frac{\gamma - 1}{v^2} + \gamma \right) \right] F^j_{rad} + \gamma \left(\delta^i_k + \frac{\gamma - 1}{v^2} v^i v_k \right) v_j P^{jk}_{rad} \tag{6.16}$$

where the barred notation indicates quantities computed in the laboratory/Eulerian frame and δ^i_j is the Kronecker delta. This expressions can be further simplified by knowing that in the radiation frame we are assuming the usual isotropic pressure tensor: $\bar{P}^{ij}_{rad} = p_{rad}\delta^i_j = \bar{E}_{rad}\delta^i_j/3$ and null fluxes: $\bar{F}^i_{rad} = 0$. Therefore, we can implement the following relations:

$$\bar{E}_{rad} = \gamma^2 E_{rad} \left(1 + \frac{v^2}{3} \right) \tag{6.17}$$

$$\bar{F}^i_{rad} = \frac{4}{3} \gamma^2 E_{rad} v^i \tag{6.18}$$

where, in 1D, only the radial component of the velocities (hence of the fluxes) is different from zero.

Finally, by applying this setup to a chosen RHD frame, we were able to initialise the profiles for the RAD-RHD evolution as shown in Fig. 6.2b. The main difference between the two initial data concerns the fluid pressure. In fact, after inserting the radiation, we found that the radiative energy dominates over the hydrodynamical one and the gas pressure collapses to very low values, not too far from the machine precision. This made the radiation evolution rather unstable and very sensitive to the choice of the parameters required to run the simulation; in particular, we had to fine tune the PLUTO's density scale[2] and pressure limit floor to allow the radiative module to work properly. Once a working setup is found, however, the results a reliable.

6.2 Fiducial Model

Radiative simulations have been run with the same RSA strategy of the RHD ones, once the opacity coefficients have been fixed. In a first step the evolution is performed up to the moment in which the photosphere is exactly superimposed on the radiative flux peak. At this stage the radiation is already decoupled from the gas particles but still contained inside the jet. Then, once the jet head crosses the $\tau = 2/3$ limit, it becomes optically thin to the radiation and the photons are finally free to stream away. To collect the information about the emitted energy we decided to place a fictitious detector at an arbitrary distance from the photosphere. In doing so we were able to measure the isotropic equivalent luminosity as:

$$L_{iso} = 4\pi r^2_{det} \times F_{rad} \tag{6.19}$$

where r_{det} is the detector radius computed as $r_{det} = r_{phot} + 5 \times 10^{12}$ cm

Moreover, we can compute the time delay of the signal with respect to the time of arrival of the GW signal generated at merger, as it would be seen by a distant observer

$$\Delta t = t_{det} - r_{det}/c \tag{6.20}$$

[2]PLUTO works with adimensional quantities, that is, before the actual computation when providing the inputs, the user should also set the length, density and velocity scales on which the physical fields will be normalized.

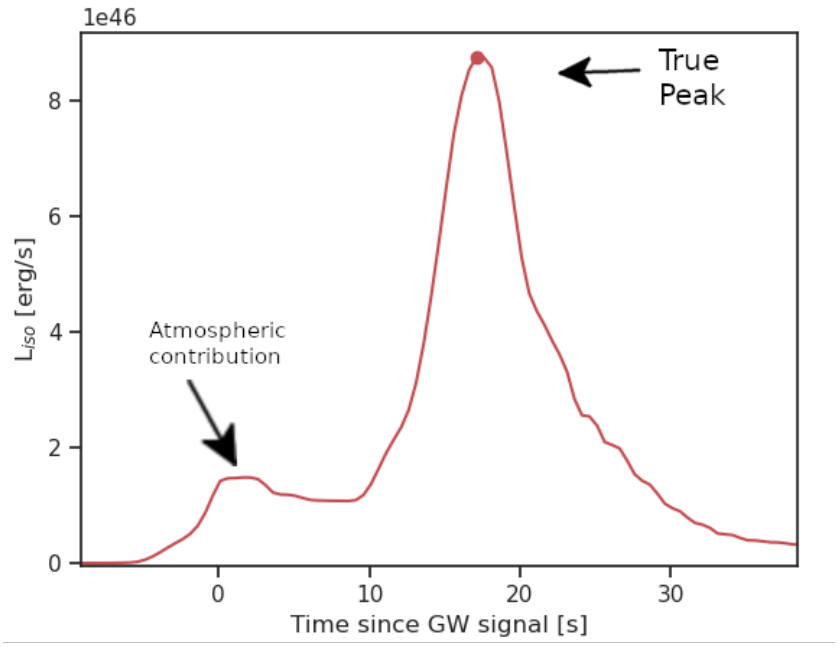

Figure 6.3: Isotropic-equivalent luminosity for our fiducial model. The profile is characterised by a well defined peak and by a small but non-negligible bump around time zero due to spurious effects raised by the artificial atmospheric contribution to the system's energetics.

where t_{det} is the time, from the merger, at which the radiative flux crosses r_{det}.

For a chosen opacity coefficient and viewing angle, we have implemented this procedure by varying all parameters relevant for the radiation treatment until converging results would confirm their reliability.

For our *fiducial* model we set a direction 15° away from the jet propagation axis and an opacity of $\kappa = 1$ cm^2/g (the total opacity coefficient being $\chi = \kappa$ with $\sigma = 0$; see Chapter 3). By experimenting with t_{1D}, t_{rad}, the resolution, and the atmospheric floor level, we found converging results (see next Section and Table 6.1) and the final outcome is given in Fig. 6.3.

In particular, such a model was obtained by first extracting the 1D profile from the data taken at $t_{1D} = 6.5$ s of the 3D evolution, after which it has been further evolved in a pure RHD setting for another $t_{rad} = 80$ s. At this point, we were able to safely insert the radiation so we performed explorative runs (also varying the spatial resolution) up to when the photosphere coincided with the flux peak at $r_{phot} = 1.6 \times 10^8$ km $\sim 10^{13}$ cm (which is in agreement with the upper boundaries of the photospheric positions estimated in literature; see Chapter 2). From that moment we performed a further evolution in order to allow the flux of free photons to cross the detector position, being collected and yielding the profile shown in Fig. 6.3, the outputs were saved each half seconds.

The result given in Fig. 6.3 shows the distinct presence of a peak at about 17 s with respect to the GW signal arrival time, reaching up to 8.7×10^{46} erg/s. The presence of contributions to the luminosity at times before $\Delta t = 0$ is a symptom of superluminar effects, which can be attributed to the atmospheric floor. Indeed, when evolving the jet for very long times (over 500 s in this case), floor effects appear. This type of effect is well known in literature and it is generally referred to as the *snowplow effect*. In our work we identify it as the source of spurious contributions to the luminosity profile which however remain well distinct from the central peak (and can thus be isolated and neglected).

6.2.1 Parameters convergence

In order to obtain the result reported in Fig. 6.3 we first had to perform a series of radiative simulations varying t_{1D}, the atmospheric floor level (in particular the α exponent), the resolution, and t_{rad}. The results are reported in Figs. [6.4-6.7].

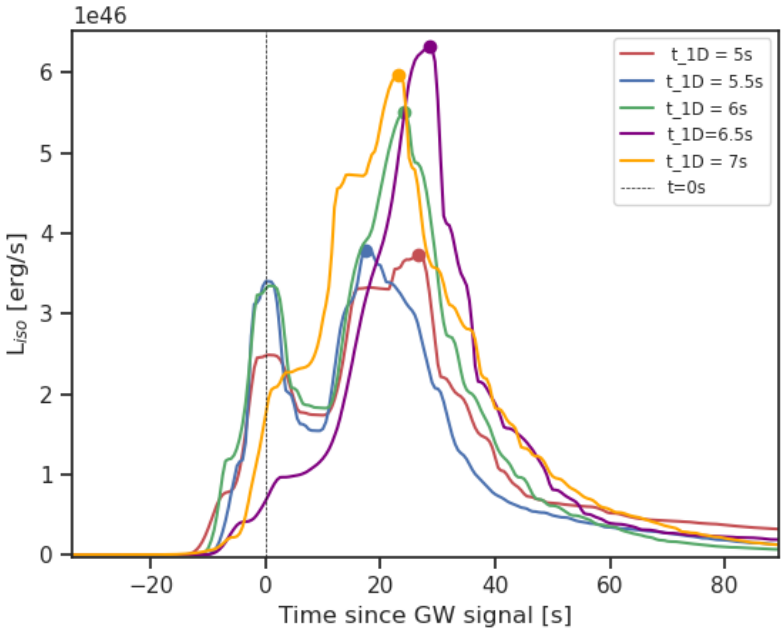

Figure 6.4: Isotropic-equivalent luminosity profiles obtained for the fiducial model by varying the time t_{1D} of the switch from 3D to 1D. Convergent behaviour is found for $t_{1D} = 6$ s or more.

In Fig. 6.4, we see convergent profiles for t_{1D} between 6 and 7 s. While in principle the higher t_{1D} the more realistic would be the adopted model, we have found that spurious effect were generated by the jet arrival close to the domain boundary (see Fig. 5.8) already in the 7 s case. Hence, we selected $t_{1D} = 6.5s$ for our fiducial setting.

To produce Fig. 6.5 we compared the data with all the fiducial parameters but varying the atmospheric profile index α. From this result it is clear that the superluminar contribution which peaks in $\Delta t = 0$ s is due to the stack of artificial atmospheric material collected above the jet front. In particular, for $\alpha \leq 5$ the atmospheric contributions get to dominate over the "physical" peak occuring later, spoiling the luminosity profile. While in this case we cannot claim a convergence yet, the situation clearly improves by lowering the floor with $\alpha = 5.5$, which is the value we adopt as fiducial. This should be enough to justify further efforts in this direction and in particular running with $\alpha > 5.5$ (i.e. even lower floor) to see if the result further changes or not.

Next, we consider the resolution. We find that an adequate resolution was provided by fixing at least $N = 3000$ radial points for the grid discretisation in the final RAD-RHD part of the simulation (Fig. 6.6). Even higher resolution, does not seem to furhter change the results.

Lastly, in Fig. 6.7 we investigated the best time to switch from the pure hydrodynamical evolution to the RAD-RHD. As discussed in the previous Section, we were constrained by technical module limitations below $t_{rad} \sim 50s$. However, we find out that at least up to ~ 60 s the computation was still spoiled by unpredictable numerical effects, which disapper at larger t_{rad}. We fixed as fiducial value $t_{rad} = 80$ s.

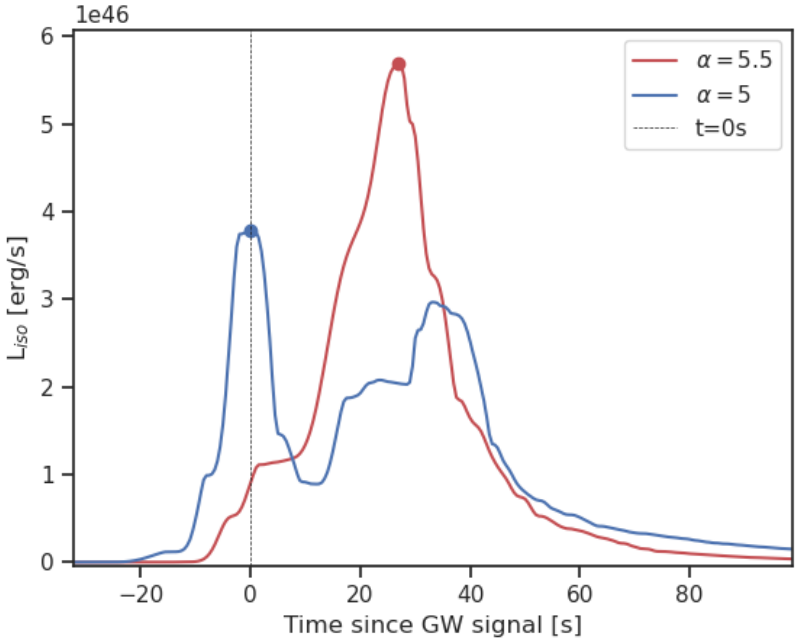

Figure 6.5: Isotropic-equivalent luminosity profiles obtained by varying the atmospheric floor. As expected, the atmospheric peak is quite incremented in the models evolved with a lower (and more realistic) artificial floor. At the same time, the artificial peak at time zero is strongly reduced.

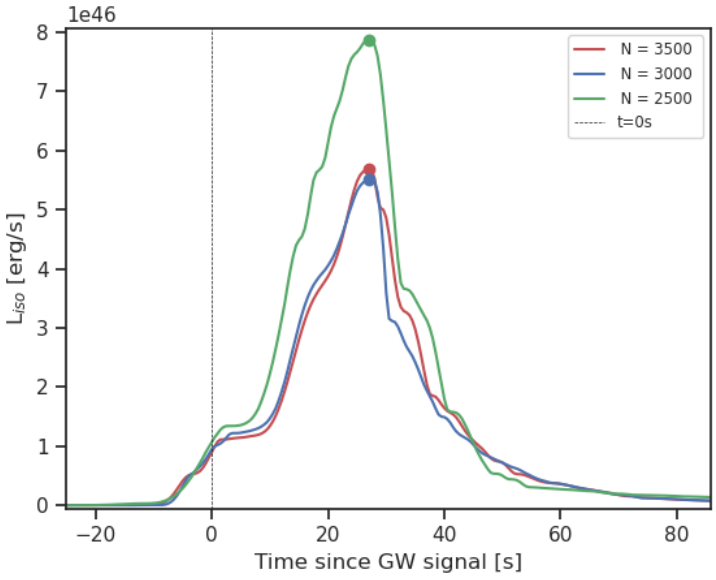

Figure 6.6: Isotropic-equivalent luminosity profiles obtained by fixing the fiducial parameters and varying the radial resolution coverage in the final RAD-RHD part of the simulation. We found that at $N = 3000$ radial points the resolution is already in the convergence regime.

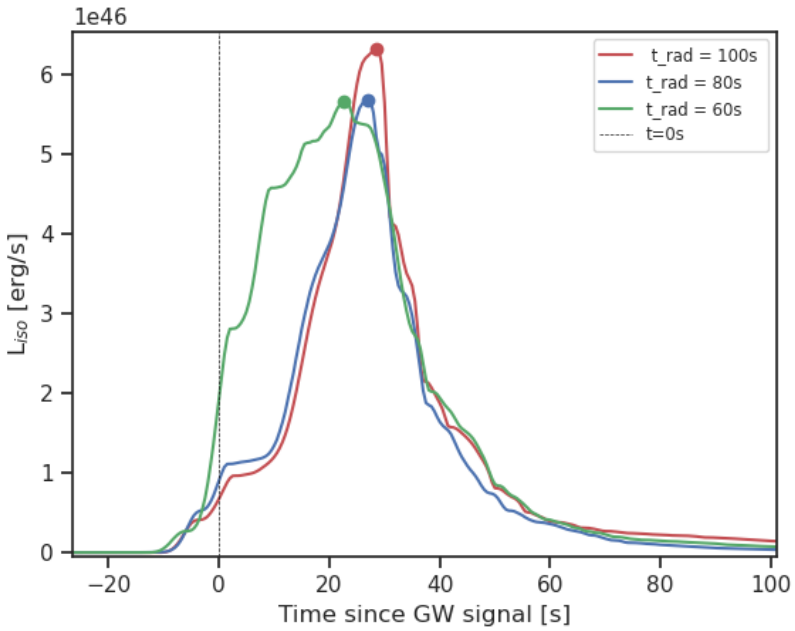

Figure 6.7: Isotropic-equivalent luminosity profiles obtained by fixing $t_{1D} = 6.5s$ and exploring different times for the activation of the radiative module. We found that the peak luminosity converged between $60 - 80$ s, with the latter yielding the cleanest profile (60 s is still affected by limitations of the radiative module, being the optical depths still too large).

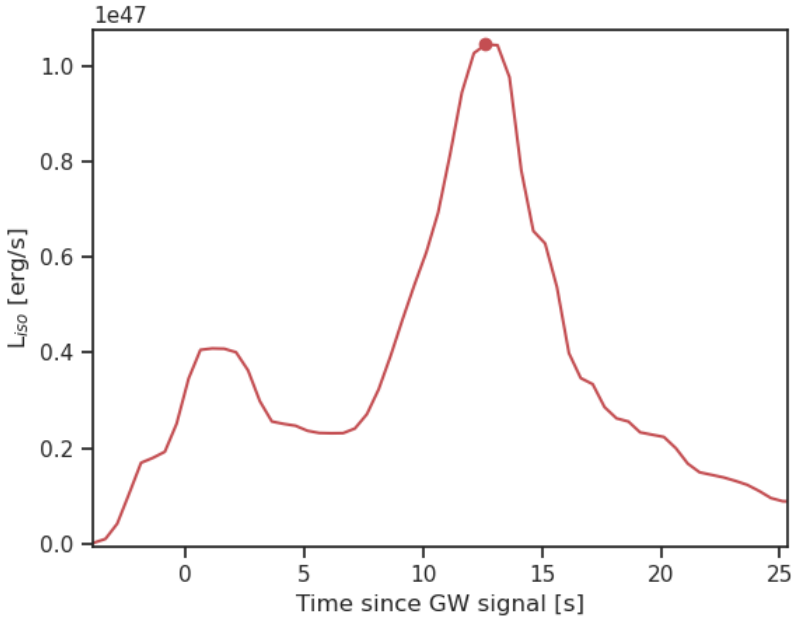

(a)

Figure 6.8: Isotropic-equivalent luminosity for $\kappa = 0.2$ cm^2/g case. The profile shows a peak similar to the fiducial model, but with a higher peak, $\sim 1.04 \times 10^{47}$ erg/s, emerging much earlier, $\Delta t \sim 12.6$ s.

6.3 Alternative Models

This work focuses on procedure development rather than in-depth parameter exploration. However, we have exploited the obtained results to perform an investigation in two more interesting physical cases. In particular, we have repeated the entire procedure starting from the fiducial model and varying, one at the time, the absorption opacity and the viewing angle.

6.3.1 κ=0.2 cm^2/g

This model was obtained by analysing the profile along the same angle of the fiducial case, $\phi = 15°$, but considering a reduced absorption opacity of $\kappa = 0.2$ cm^2/g. We started the exploration by testing all the same parameters of the fiducial case. While we had to maintain the data at $t_{1D} = 6.5$ s, as this was the more realistic 3D frame achievable along the 15° direction before incurring in boundaries spurious effects, we found out that we had room for improvement in reducing the t_{rad} thanks to the lower opacity implemented. Eventually we understood that, despite a further RHD extrapolation was still required, now the radiation could be already inserted at $t_{rad} = 40$ s, where the profiles start to converge (see also Fig. 6.9).

As expected, in this case the jet head reaches the photosphere in a shorter time and at a closer distance, around $r_{phot} \sim 9.6 \times 10^{12}$ cm, hence yielding a slightly more powerful and peaked profile with respect to the fiducial case, Fig. 6.8. However, when comparing the two profiles (see Fig. 6.10) they appear qualitatively similar.

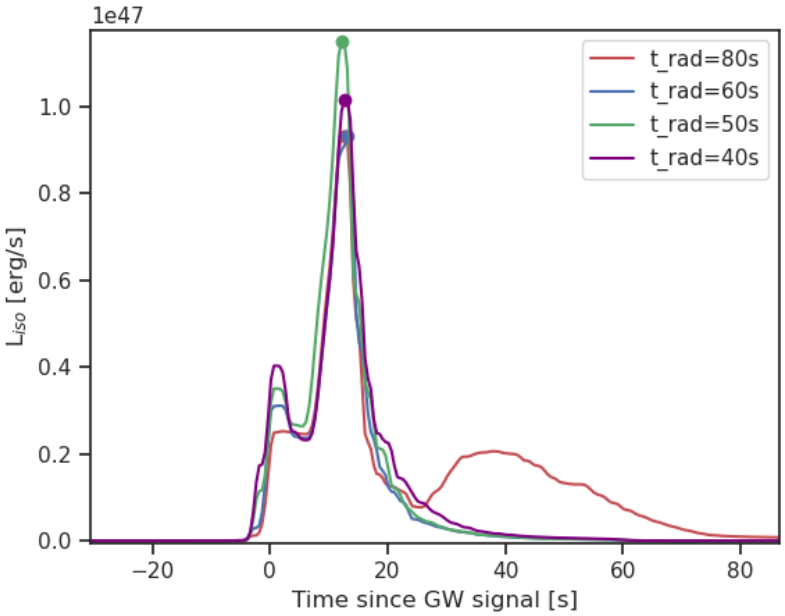

Figure 6.9: Isotropic-equivalent luminosity profiles for the case $\kappa = 0.2$ cm^2/g obtained by varying the t_{rad} parameter. In this case, the model with $t_{rad} = 80$ s shows a smaller bump at later Δt which turned to be of numerical origins, due to the small value of the pressure too close to machine precision.

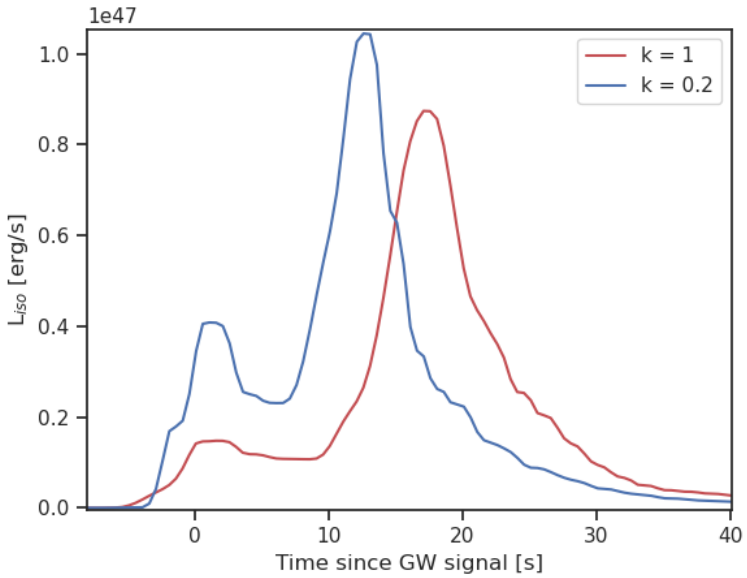

Figure 6.10: Comparison between the isotropic-equivalent luminosities for the case $\kappa = 1$ cm^2/g (red line) and $\kappa = 0.2$ cm^2/g (blue line).

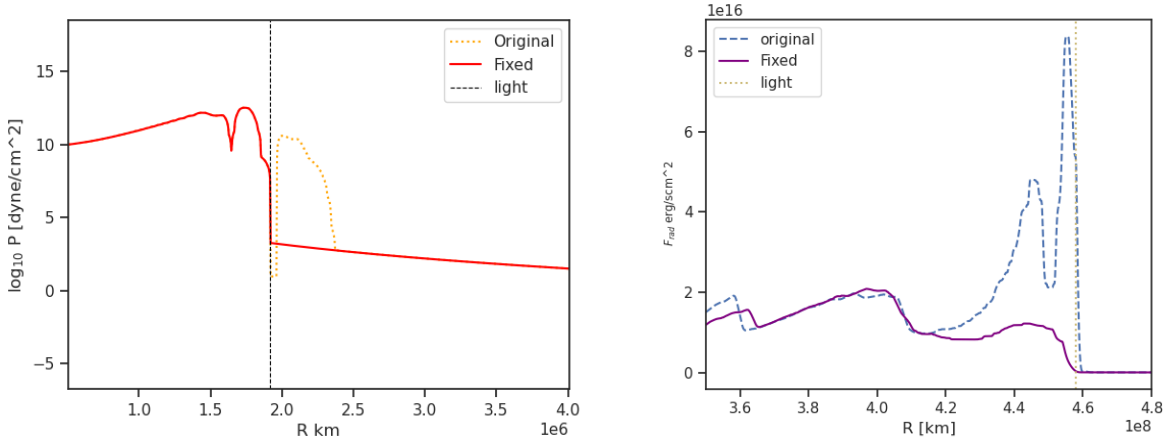

(a) Initial pressures at 6.5 s

(b) Emitted fluxes at $\sim$ 1530 s

Figure 6.11: *Left:* Comparison between the original data (yellow dotted line) as extracted from the 3D frame at 6.5 s and the data implemented in the radiative evolution after the correction at the photon radius (red solid line). *Right:* Comparison between the radiative fluxes obtained by evolving the original data without correction (blue dotted line) and those with the adopted fix (purple solid line). Due to numerical instabilities the original data wrongly partitioned the system's energy during the evolution, ending up in associating most of the radiative flux to the atmospheric bulk.

6.3.2 Angle 25°

In the last model, in order to investigate the outer part of the range within which GRB 170817A has been likely seen, we consider a larger viewing angle of 25° from the jet axis.

Due to the 3D jet anisotropies, the new profile presents rather different features with respect to the one at 15°. First of all, as we can see in Fig. 5.8, the jet profile extracted along wider angles is more and more receded and detached from the domain edge. Moreover, the pressure distribution breaks a certain uniformity (which instead persists in the density profile) in favour of a more complex structure composed by wells and clumps of energy. In this case, it might be more difficult to separate the real physical features from the ones raised by the racked up atmosphere, which could eventually lead to the wrong energy partition during the radiative evolution. This, in turn, could translate into a fictious profile in which most of the luminosity seems to come from the artificial atmosphere (dotted line in Fig. 6.11b). This is worsened by the fact that we are working rather close to the machine precision, hence the solution can be easily affected by the numerical floor reconstruction. In order to extract a reliable profile for this case, we had to apply a fix to the initial conditions exploiting the the causality limitations. Indeed, any superluminar profiles, above the photon radius at a given time from the merger, is generated by artificial effects and can be in principle cut out. While in the $\phi = 15°$ case the physical profile and the atmospheric contribution were rather mixed up, so that it wasn't clear where we could have intervened to correct the solution, we have noticed that for the new angle the pressure profile was distinctly detached from the above atmosphere. This allows us to safely fix the initial 1D data eliminating the atmosphere contribution (or most of it), yielding the profile shown in Fig. 6.11a. Despite the data fixing, the radiative evolution itself accumulated a new atmospheric bulk which however was better handled in terms of system's energy distribution.

After employing the new and fixed initial data we carried the evolution according to the developed procedure, fixing all the other parameters as those of the fiducial case. In particular, we set again the absorption opacity as $\kappa = 1$ cm^2/g. Since the jet head was rather receded with respect to the domain boundary, in this case we had the possibility to start from a more evolved (hence more realistic) 3D frame. We have studied the luminosity profiles obtained by varying

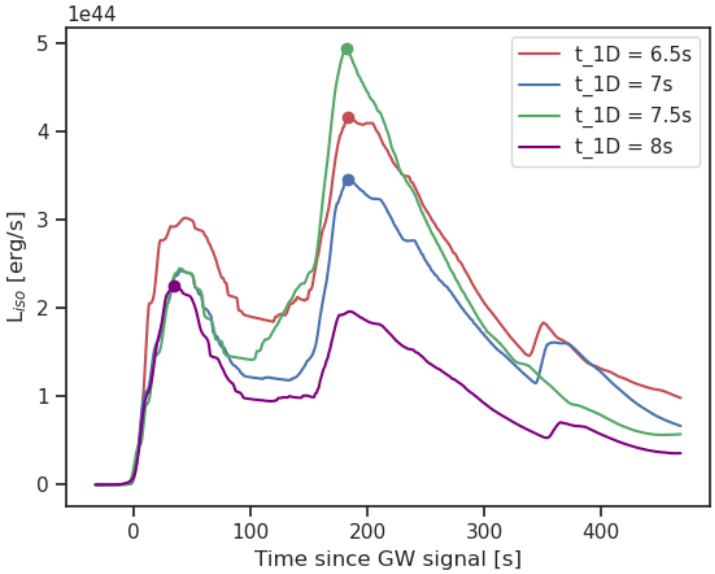

Figure 6.12: Isotropic-equivalent luminosity profiles for the model $\phi = 25°$ at varying t_{1D} values.

t_{1D} (see Fig. 6.12) and we decided to adopt the data extrapolated up to 7.5 s, by noticing that the data at 8 s was again spoiled by outer boundary interference.

With this setup we finally obtained the isotropic-equivalent luminosity represented in Fig. 6.13. This profile is evidently different with respect to the previous two (i.e. the fiducial and $\kappa = 0.2$ cm^2/g cases): the peak is ~ 200 lower and the delay time is at least one order of magnitude larger with respect to what obtained with $\phi = 15°$.

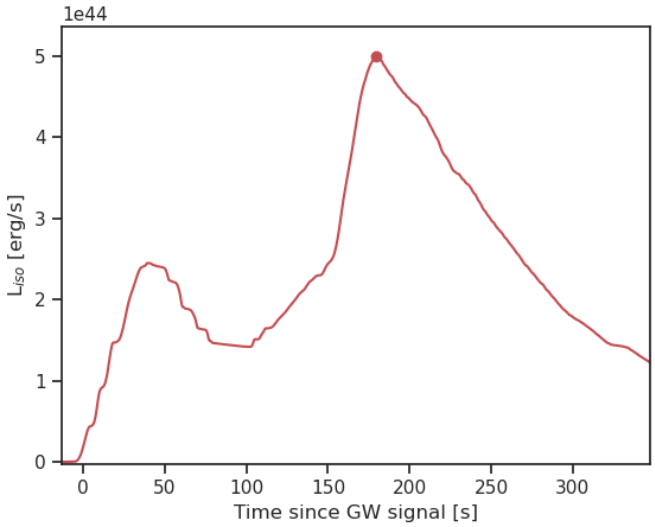

Figure 6.13: Isotropic-equivalent luminosity for the $\phi = 25°$ case. The profile peaks at $\sim 5 \times 10^{44}$ erg/s and accumulates an important delay of $\Delta t \sim 180$ s.

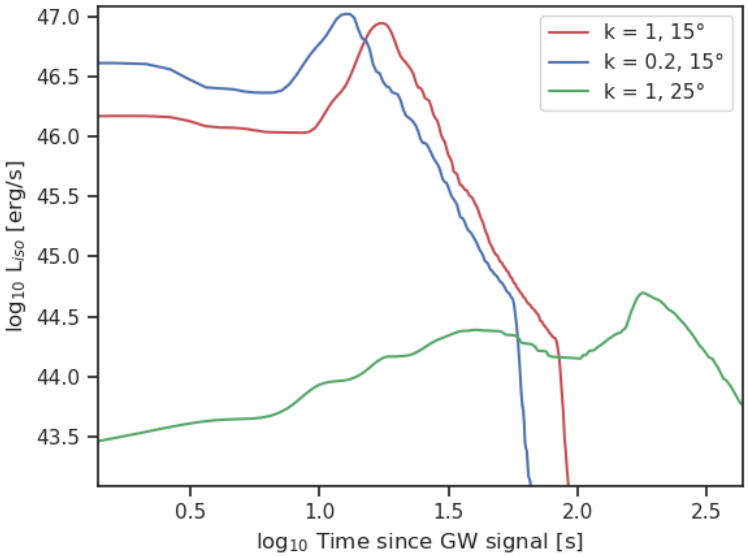

Figure 6.14: Logarithmic isotropic-equivalent luminosities for the three different cases studied in this work.

6.3.3 Model Comparisons

Having employed the same procedure to derive all the three models, we can now proceed by comparing and commenting them. In Fig. 6.14 we have reported all the isotropic-equivalent luminosity profiles in a log-log plane. The opacity seems not to majorly affect the final result, with only a significant difference in the time at which the jet head reaches the photosphere. However, changing the direction of observation has a profound impact. Wider angles of view correspond to much more delayed profiles (in which the physical component is rather receded with respect to the photon radius, accumulating a greater delay). Moreover, the latter case is much less energetic and with a wider peak duration with respect to the former models.

Cases	t_{1D}	t_{rad}	r_{phot}	Δt	L_{iso}
$\kappa = 0.2, 15$	6.5 s	40 s	9.6×10^{12}cm	12.6s	1.04×10^{47}erg/s
$\kappa = 1, 15$	6.5 s	80 s	1.6×10^{13} cm	17s	8.7×10^{46} erg/s
$\kappa = 1, 25$	7.5 s	50 s	3.4×10^{13} cm	180s	5×10^{44} erg/s

Table 6.1: Fundamental parameters and results obtained for the three models considered in this work (varying the opacity κ and the viewing angle with respect to the jet axis). t_{1D} and t_{rad} are the times (after merger) at which we moved from 3D to 1D evolution and we introduced the radiative component, respectively. r_{phot} is computed as the distance where the photosphere ($\tau = 2/3$) is exactly superimposed to the radiative flux peak. Lastly, Δt and L_{iso} are respectively the peak time (after merger) and the value for the isotropic-equivalent peak luminosity.

The comparison with GRB 170817A allows us to draw a few more conclusions. For the event of August 2017 we used the data reported in Chapter 2, namely: $\Delta t = 1.7$ s and $L_{iso} = 1.6 \pm 0.6 \times 10^{47}$ erg/s. In Fig. 6.15 we show in a log-linear plot how these numbers compare with our results. As we can see, while the outcome obtained for a viewing angle of 25° is rather distant from the August 2017 gamma-ray observation, the models derived along a direction 15° away from the jet axis have a peak luminosity consistent with the error bar of GRB 170817A, although the time delay between between EM and GW signals is larger by about 1 order of magnitude.

Besides the fact that we are only accounting for thermal emission, here we only consider a single BNS merger plus hydrodynamic jet evolution model, so the comparison cannot be consid-

ered conclusive. Nonetheless, under the (purely hypothetical) assumption that the underlying physical model was the correct one, the results obtained would suggest that:

- an opacity κ between 0.2 and 1 (in cgs) is consistent with the August 2017 event;
- the GRB 170817A jet was pointing less than 15° away from us;
- the bolometric isotropic-equivalent luminosity obtained assuming purely thermal emission gives the right order of magnitude.

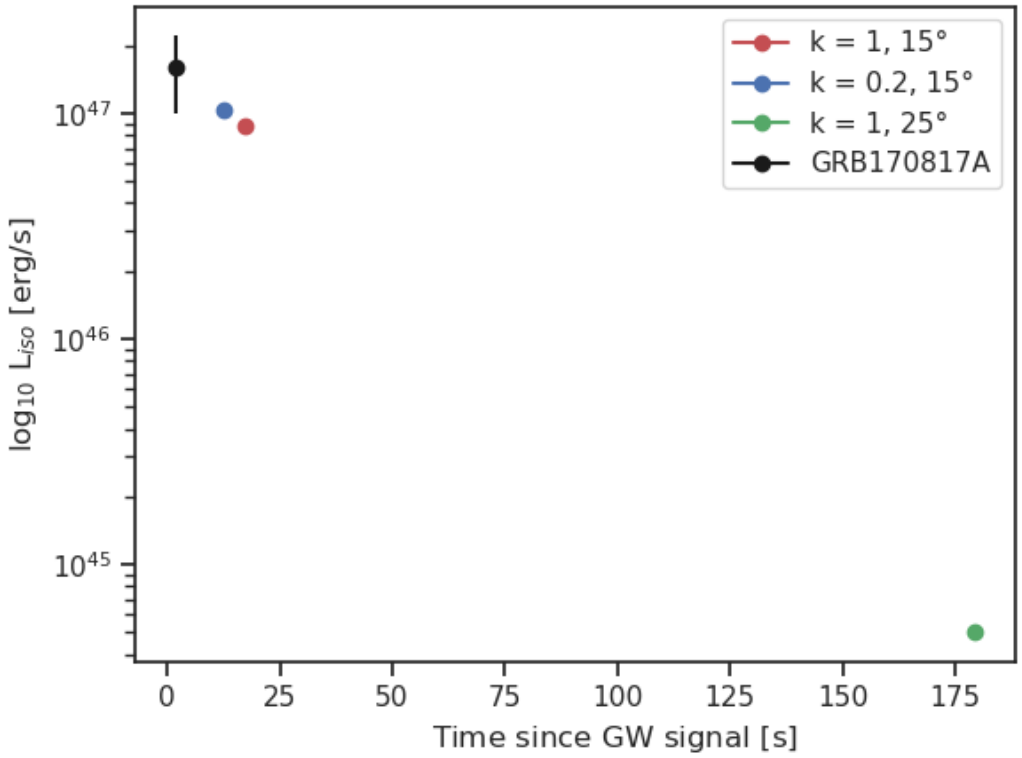

Figure 6.15: Peak isotropic-equivalent luminosity comparison between our models and GRB 170817A (black dot with error bar).

Chapter 7

Summary and Outlook

The aim of this Thesis was to contribute to the theoretical study and modeling of the short-gamma ray burst emission, with a particular focus on the wide-angle high energy signal powered by the jet breaking out from the surrounding BNS merger environment, where the corresponding radiation is eventually liberated when the outflow front becomes optically thin. This work enters in the development of an integrated scenario which exploits state-of-the-art simulations to reproduce the entire phenomenon: from the accurate general relativistic simulation of a BNS merger, through the injection of a relativistic jet into the realistic post-merger environment and its breakout and further propagation, towards the final release of radiation. The strongest motivation behind this approach and the corresponding efforts comes from the observation of GW170817/GRB 170817A, which is the first EM-GW multimessanger event ever detected and that, if appropriately modeled, can provide constraints on a variety of fundamental properties of the system and answers to different key astrophysical questions.

Here we present the very first application in the context of short gamma-ray burst jets of a newly released PLUTO module for including (2-moment) radiation transport in the relativistic hydrodynamic evolution, where the latter exploits the unique capabilities of the Padova group in consistently combining BNS merger and jet simulations. The main result we obtained was the development of a consistent procedure which, under a few approximations (such as pure thermal radiation), allows for the extraction of the radiative content of the jet along any fixed observer direction, finally predicting the isotropic-equivalent luminosity that would be seen. The application of this new procedure to three selected models also allowed for a very first tentative comparison with the high-energy prompt burst of GRB 170817A.

7.1 Procedure

In order to study the thermal radiation emitted from the ultra-relativistic jet we first had to find a sustainable and reliable way to continue the jet evolution up to very large time and spatial scales, very much beyond the 1 s after merger typically covered in the PLUTO jet simulations of the group. This follows from the consideration that, at early times, the high density of the outflow material enforces a LTE regime, keeping the photons trapped and thus causing the radiation content to be simply advected within the jet material.

The extension is first performed maintaining the 3D framework, but excising out the slower and inner parts, allowing us to focus only on the relevant (more energetic) regions of the jet. In this way, we may slightly reduce the degree of realism of the model, but we save enough computational resources to evolve the jet head up to almost 8 seconds after merger. The second part of the simulation extension should be performed once having fixed an arbitrary direction, so that we can turn to a 1D evolution. In fact, to further reduce the opacity of the system and to get closer to the photosphere we have to evolve the jet head for very long times, up to order

~ 100 s, and maintaining a 3D evolution for so long is simply not sustainable with our current resources. Therefore, we have to perform an extraction of the jet profile along a specific radial direction by fixing the angular coordinates. This is another approximation as we are going to ignore further transversal interactions. The time to switch to the uni-dimensional framework, namely t_{1D}, is treated as a free parameter.

The second part of the procedure entails the actual inclusion of the radiation. When the photosphere starts to recede upon the jet front we can activate the radiative module and the time at which this happens, t_{rad}, has to be carefully chosen in agreement with the good functioning of the module.

When inserting the radiation, the LTE is broken and photons start to be decoupled from the matter. A first RAD-RHD evolution is performed up to the moment in which the photosphere exactly coincides with the peak of the radiative flux. Once the jet becomes finally optically thin to light, the latter can start to freely stream away. Then, we re-evolve the system a second time around the above critical time with increased resolution, in order to finally collect the emitted radiation at a fictitious detector placed in an arbitrarily position, a little farther out than the photosphere. In this way we are able to get the information about the emitted isotropic-equivalent luminosity and, by comparison with the distance covered by a free signal emitted at merger, we can further estimate the time delay of the luminosity peak with respect to the transit of the merger GW signal.

7.2 Results

We tested the procedure by applying it to three different physical cases. Simulations which employ numerical scheme for radiation transport have to deal with low values of density and pressure that may get rather close to the machine precision. For this reason, obtaining the pursued results we often had to search for the optimal working parameters (including, e.g., the density scale of the PLUTO simulation), finally looking for convergence, consistency, and reliability of the adopted outcome.

The most explored model, which is also our fiducial case, is the one we obtained by fixing the observation direction at 15° from the jet's propagation axis, and by selecting the absorption opacity coefficient to be $\kappa = 1$ cm^2/g. In this case, we converged to an optimal setup with a resolution of $N = 3500$ radial grid points in the last RAD-RHD part of the evolution, $t_{1D} = 6.5$ s, and $t_{rad} = 80$ s. The final isotropic-equivalent luminosity profile shows a clean peak at 8.7×10^{46} erg/s which crosses the detector with a delay of $\Delta t = 17$ s with respect to the GW signal. Moreover, the luminosity shows a further, partly superluminar contribution associated to the snowplow effect raised above the jet front and due to the accumulated artificial atmosphere, affecting the system's energetics. We demonstrated the atmospheric origin of this additional peak by trying two different atmospheric floor values, finally adopting the lower one as the most realistic.

We further considered two extra models by varying, one at the time, the most relevant physical parameters, namely the viewing angle of the observer and the mater opacity. In this way we obtained:

- a luminosity profile for a lower opacity of $\kappa = 0.2$ cm^2/g. The outcome is very similar to the fiducial one, presenting, as expected, a slightly higher luminosity peak of $\sim 1.04 \times 10^{47}$ erg/s and a slightly smaller delay of $\Delta t = 12.6$ s;

- a luminosity profile for a different viewing angle, but keeping the same fiducial opacity coefficient ($\kappa = 0.2$ cm^2/g). In order to investigate the range of angles which most likely contains the direction along which GRB 170817A was observed, we decided to evolve the

profile taken at 25° from the jet's propagation axis. In this case, the initial data required further manipulations to yield a consistent result and, in the end, we found a very different luminosity profile which peaks at $\sim 5 \times 10^{44}$ erg/s with an important delay of $\Delta t \sim 150$ s with respect to the GW signal.

By comparing the models among each other we concluded that while the choice of the opacity coefficient does not seem to really affect the outcome, varying the viewing angle may lead to very different results. The comparison with GRB 170817A data suggests that, at least for the model at hand, angles of 15° or smaller are favored, while the opacity range we covered appears consistent with the August 2017 event.

7.3 Future work

This work was mostly focused on the development and testing of a systematic procedure able to predict the wide-angle radiation powered by an ultra-relativistic jet braking out of the surrounding post-merger environment, under the assumption of purely thermal emission. Current initial results bode well toward the viability of an extensive application of this kind of framework to broaden our understanding of the extremely vast and rich field of short gamma-ray bursts. Immediate application of the developed procedure can, for example, get to cover a wider range of observation directions (providing a global insight on the overall radiation angular distribution) but also exploit the luminosity information to extract clues on the temperature profile and hence on the radiation spectral distribution (at least within the purely thermal radiation assumption).

Furthermore, in this framework there is plenty of room for improvement and refining. Its upgrading can be tackled in two general directions:

Direct improvements: To obtain the current results we had to perform a number of approximations due to the limited computational resources, as the transition to 1D for the jet evolution after 5-8 s (after merger), or due to limitations of the radiation transport module, implying the introduction of radiation only at late times (40-80 s after merger). Thus, efforts should be dedicated to mitigating the above limitations. Moreover, the artificial atmosphere should also be further reduced to minimize its interference with the system's energetic profile.

Indirect and long-term improvements: Being inserted in an integrated framework, this work is strongly dependent on the provided initial conditions. Improvement on the input data can concern the increase of the degree of realism on the description of both the BNS merger event and the relativistic jet injection. Works are already underway to enhance the GRMHD simulations with newly developed codes [130, 131] including, among other things, the neutrino radiation transport [132] and to evolve even more accurate magnetized jet models (see for example Fig. 7.1). Furthermore, a complementary approach should be pursued for the description of non-thermal radiation, which will be tackled with another PLUTO module for the description of Lagrangian particles [133]. Combining the latter with the radiation transport employed in this work will finally provide complete lightcurves and spectra.

All of these routes require certainly effort and dedication, supported by the access to copious computational resources on competitive HPC facilities.

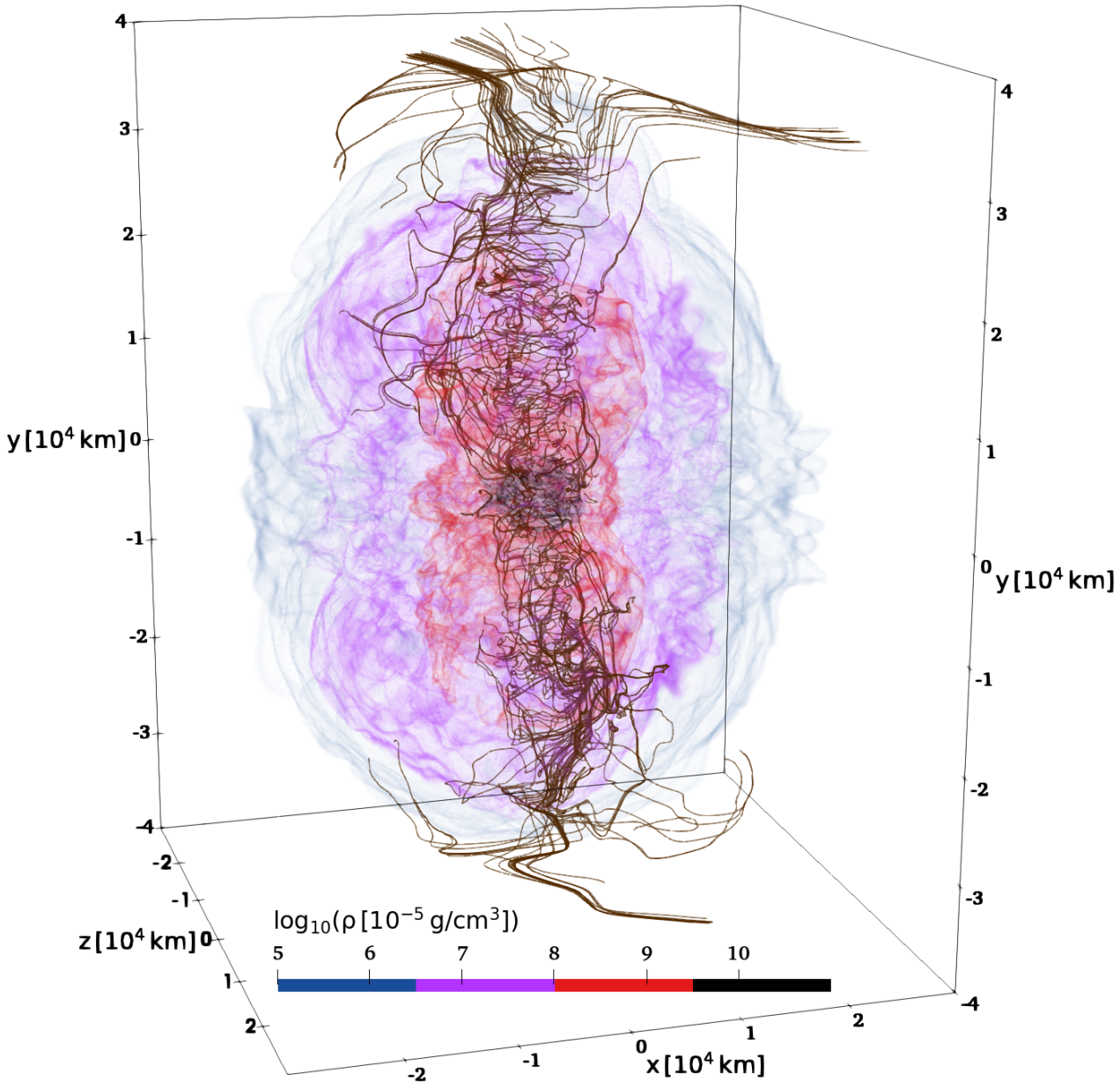

Figure 7.1: Magnetized 3-dimensional jet-cocoon structure at the breakout (from Pavan et al., in preparation). The color scheme indicates the density distribution while the lines are the magnetic field lines in the intensity range between $[10^{11} - 10^{13}$ G]. Courtesy of A.Pavan (DFA, Padova University).

.

Bibliography

[1] André da Silva Schneider, Evan O'Connor, Elvira Granqvist, Aurore Betranhandy, and Sean M. Couch. Equation of state and progenitor dependence of stellar-mass black hole formation. *The Astrophysical Journal*, 894(1):4, apr 2020. doi: 10.3847/1538-4357/ab8308. URL https://doi.org/10.3847/1538-4357/ab8308.

[2] Nicola Giacobbo and Michela Mapelli. Revising Natal Kick Prescriptions in Population Synthesis Simulations. , 891(2):141, March 2020. doi: 10.3847/1538-4357/ab7335.

[3] Eric Burns. Neutron star mergers and how to study them. *Living Reviews in Relativity*, 23(1):1–177, 2020.

[4] Jarrod R Hurley, Christopher A Tout, and Onno R Pols. Evolution of binary stars and the effect of tides on binary populations. *Monthly Notices of the Royal Astronomical Society*, 329(4):897–928, 2002.

[5] Krzysztof Belczynski, Vassiliki Kalogera, and Tomasz Bulik. A comprehensive study of binary compact objects as gravitational wave sources: evolutionary channels, rates, and physical properties. *The Astrophysical Journal*, 572(1):407, 2002.

[6] Aleksander Sadowski, Krzysztof Belczynski, Tomasz Bulik, Natalia Ivanova, Frederic A. Rasio, and Richard O'Shaughnessy. The Total Merger Rate of Compact Object Binaries in the Local Universe. , 676(2):1162–1169, April 2008. doi: 10.1086/528932.

[7] Joshua A Faber and Frederic A Rasio. Binary neutron star mergers. *Living Reviews in Relativity*, 15(1):1–83, 2012.

[8] Matthias U. Kruckow, Thomas M. Tauris, Norbert Langer, Michael Kramer, and Robert G. Izzard. Progenitors of gravitational wave mergers: binary evolution with the stellar grid-based code COMBINE. , 481(2):1908–1949, December 2018. doi: 10.1093/mnras/sty2190.

[9] Nicola Giacobbo and Michela Mapelli. The progenitors of compact-object binaries: impact of metallicity, common envelope and natal kicks. , 480(2):2011–2030, October 2018. doi: 10.1093/mnras/sty1999.

[10] Michael S. Hjellming and Ronald F. Webbink. Thresholds for Rapid Mass Transfer in Binary System. I. Polytropic Models. , 318:794, July 1987. doi: 10.1086/165412.

[11] Andreas AC Sander, JS Vink, and WR Hamann. Driving classical wolf–rayet winds: a γ-and z-dependent mass-loss. *Monthly Notices of the Royal Astronomical Society*, 491(3): 4406–4425, 2020.

[12] Vink, Jorick S. and de Koter, A. On the metallicity dependence of wolf-rayet winds. *A&A*, 442(2):587–596, 2005. doi: 10.1051/0004-6361:20052862. URL https://doi.org/10.1051/0004-6361:20052862.

[13] Pablo Marchant, Kaliroë M. W. Pappas, Monica Gallegos-Garcia, Christopher P. L. Berry, Ronald E. Taam, Vicky Kalogera, and Philipp Podsiadlowski. The role of mass transfer and common envelope evolution in the formation of merging binary black holes. , 650: A107, June 2021. doi: 10.1051/0004-6361/202039992.

[14] Jakub Klencki, Gijs Nelemans, Alina G. Istrate, and Martyna Chruslinska. It has to be cool: Supergiant progenitors of binary black hole mergers from common-envelope evolution. , 645:A54, January 2021. doi: 10.1051/0004-6361/202038707.

[15] Roger A. Chevalier. Neutron Star Accretion in a Stellar Envelope. , 411:L33, July 1993. doi: 10.1086/186905.

[16] GE Brown, JC Weingartner, and Ralph AMJ Wijers. On the formation of low-mass black holes in massive binary stars. *arXiv preprint astro-ph/9505092*, 1995.

[17] Hans A Bethe, Gerald E Brown, and Chang-Hwan Lee. Evolution and merging of binaries with compact objects. *Physics reports*, 442(1-6):5–22, 2007.

[18] Alejandro Vigna-Gómez, Coenraad J Neijssel, Simon Stevenson, Jim W Barrett, Krzysztof Belczynski, Stephen Justham, Selma E de Mink, Bernhard Müller, Philipp Podsiadlowski, Mathieu Renzo, et al. On the formation history of galactic double neutron stars. *Monthly Notices of the Royal Astronomical Society*, 481(3):4009–4029, 2018.

[19] Edward P. J. van den Heuvel and Jan van Paradijs. X-ray binaries. *Scientific American*, 269(5):64–71, 1993. ISSN 00368733, 19467087. URL http://www.jstor.org/stable/24941685.

[20] D. Bhattacharya and E. P. J. van den Heuvel. Formation and evolution of binary and millisecond radio pulsars. , 203(1-2):1–124, January 1991. doi: 10.1016/0370-1573(91)90064-S.

[21] Chris L Fryer, SE Woosley, and Dieter H Hartmann. Formation rates of black hole accretion disk gamma-ray bursts. *The Astrophysical Journal*, 526(1):152, 1999.

[22] Floor S. Broekgaarden, Edo Berger, Coenraad J. Neijssel, Alejandro Vigna-Gómez, Debatri Chattopadhyay, Simon Stevenson, Martyna Chruslinska, Stephen Justham, Selma E. de Mink, and Ilya Mandel. Impact of massive binary star and cosmic evolution on gravitational wave observations I: black hole-neutron star mergers. , 508(4):5028–5063, December 2021. doi: 10.1093/mnras/stab2716.

[23] Javier Antelis and Claudia Moreno. Obtaining gravitational waves from inspiral binary systems using ligo data. *The European Physical Journal Plus*, 132, 01 2017. doi: 10.1140/epjp/i2017-11283-5.

[24] C W Misner, K.S. Thorne, and Wheeler J A. *Gravitation*. Academic Press, San Francisco, 1973.

[25] L Rezzolla and O Zanotti. *Relativistic hydrodynamics*. Oxford University Press, 2013.

[26] Luciano Rezzolla, Luca Baiotti, Bruno Giacomazzo, David Link, and José A Font. Accurate evolutions of unequal-mass neutron-star binaries: properties of the torus and short grb engines. *Classical and Quantum Gravity*, 27(11):114105, 2010.

[27] Luca Baiotti, Bruno Giacomazzo, and Luciano Rezzolla. Accurate evolutions of inspiralling neutron-star binaries: Prompt and delayed collapse to a black hole. *Phys. Rev. D*, 78: 084033, Oct 2008. doi: 10.1103/PhysRevD.78.084033. URL https://link.aps.org/doi/10.1103/PhysRevD.78.084033.

[28] Olindo Zanotti, José A. Font, Luciano Rezzolla, and Pedro J. Montero. Dynamics of oscillating relativistic tori around Kerr black holes. *Monthly Notices of the Royal Astronomical Society*, 356(4):1371–1382, 02 2005. ISSN 0035-8711. doi: 10.1111/j.1365-2966.2004.08567.x. URL https://doi.org/10.1111/j.1365-2966.2004.08567.x.

[29] Riccardo Ciolfi. Binary neutron star mergers after gw170817. *Frontiers in Astronomy and Space Sciences*, 7:27, 2020.

[30] Riccardo Ciolfi. Collimated outflows from long-lived binary neutron star merger remnants. *Monthly Notices of the Royal Astronomical Society Letters*, 495(1):L66–L70, June 2020. doi: 10.1093/mnrasl/slaa062.

[31] Riccardo Ciolfi, Wolfgang Kastaun, Bruno Giacomazzo, Andrea Endrizzi, Daniel M Siegel, and Rosalba Perna. General relativistic magnetohydrodynamic simulations of binary neutron star mergers forming a long-lived neutron star. *Physical Review D*, 95(6):063016, 2017.

[32] Kenta Kiuchi, Koutarou Kyutoku, Yuichiro Sekiguchi, Masaru Shibata, and Tomohide Wada. High resolution numerical relativity simulations for the merger of binary magnetized neutron stars. *Phys. Rev. D*, 90:041502, Aug 2014. doi: 10.1103/PhysRevD.90.041502. URL https://link.aps.org/doi/10.1103/PhysRevD.90.041502.

[33] Luciano Rezzolla, Bruno Giacomazzo, Luca Baiotti, Jonathan Granot, Chryssa Kouveliotou, and Miguel A Aloy. The missing link: merging neutron stars naturally produce jet-like structures and can power short gamma-ray bursts. *The Astrophysical Journal Letters*, 732(1):L6, 2011.

[34] Kenta Kiuchi, Pablo Cerdá-Durán, Koutarou Kyutoku, Yuichiro Sekiguchi, and Masaru Shibata. Efficient magnetic-field amplification due to the kelvin-helmholtz instability in binary neutron star mergers. *Physical Review D*, 92(12):124034, 2015.

[35] S Chandrasekhar. *Hydrodynamic and Hydromagnetic Stability*. 1981.

[36] G. Bodo, S. Massaglia, Attilio Ferrari, and E. Trussoni. Kelvin-helmholtz instability of hydrodynamic supersonic jets. *Astronomy and Astrophysics*, 283:655–676, 02 1994.

[37] Matthew D. Duez, Yuk Tung Liu, Stuart L. Shapiro, Masaru Shibata, and Branson C. Stephens. Collapse of magnetized hypermassive neutron stars in general relativity. *Phys. Rev. Lett.*, 96:031101, Jan 2006. doi: 10.1103/PhysRevLett.96.031101. URL https://link.aps.org/doi/10.1103/PhysRevLett.96.031101.

[38] Riccardo Ciolfi. The key role of magnetic fields in binary neutron star mergers. *General Relativity and Gravitation*, 52(6):1–29, 2020.

[39] Riccardo Ciolfi, Wolfgang Kastaun, Jay Vijay Kalinani, and Bruno Giacomazzo. First 100 ms of a long-lived magnetized neutron star formed in a binary neutron star merger. *Physical Review D*, 100(2):023005, 2019.

[40] Wolfgang Kastaun and Filippo Galeazzi. Properties of hypermassive neutron stars formed in mergers of spinning binaries. *Physical Review D*, 91(6):064027, 2015.

[41] Brian D Metzger. Kilonovae. *Living Reviews in Relativity*, 23(1):1–89, 2020.

[42] Luke Bovard, Dirk Martin, Federico Guercilena, Almudena Arcones, Luciano Rezzolla, and Oleg Korobkin. r-process nucleosynthesis from matter ejected in binary neutron star mergers. *Physical Review D*, 96(12):124005, 2017.

[43] Albino Perego, David Radice, and Sebastiano Bernuzzi. At 2017gfo: an anisotropic and three-component kilonova counterpart of gw170817. *The Astrophysical Journal Letters*, 850(2):L37, 2017.

[44] Riccardo Ciolfi and Jay Vijay Kalinani. Magnetically driven baryon winds from binary neutron star merger remnants and the blue kilonova of 2017 august. *The Astrophysical Journal Letters*, 900(2):L35, 2020.

[45] Daniel Kasen, Brian Metzger, Jennifer Barnes, Eliot Quataert, and Enrico Ramirez-Ruiz. Origin of the heavy elements in binary neutron-star mergers from a gravitational-wave event. *Nature*, 551(7678):80–84, 2017.

[46] Y. Z. Qian. Supernovae versus Neutron Star Mergers as the Major R-Process Sources. , 534(1):L67–L70, May 2000. doi: 10.1086/312659.

[47] Elisabeth Vangioni, Stéphane Goriely, Frédéric Daigne, Patrick François, and Krzysztof Belczynski. Cosmic neutron-star merger rate and gravitational waves constrained by the r-process nucleosynthesis. *Monthly Notices of the Royal Astronomical Society*, 455(1):17–34, 10 2015. ISSN 0035-8711. doi: 10.1093/mnras/stv2296. URL https://doi.org/10.1093/mnras/stv2296.

[48] Bing Zhang. *The Physics of Gamma-Ray Bursts*. 2018. doi: 10.1017/9781139226530.

[49] P. D'Avanzo. Short gamma-ray bursts: A review. *Journal of High Energy Astrophysics*, 7:73–80, 2015. ISSN 2214-4048. doi: https://doi.org/10.1016/j.jheap.2015.07.002. URL https://www.sciencedirect.com/science/article/pii/S2214404815000415. Swift 10 Years of Discovery, a novel approach to Time Domain Astronomy.

[50] G. Ghirlanda, G. Ghisellini, and L. Nava. Short and long gamma-ray bursts: same emission mechanism? *Monthly Notices of the Royal Astronomical Society: Letters*, 418(1):L109–L113, 11 2011. ISSN 1745-3925. doi: 10.1111/j.1745-3933.2011.01154.x. URL https://doi.org/10.1111/j.1745-3933.2011.01154.x.

[51] BA Harmon, CA Wilson, GJ Fishman, V Connaughton, W Henze, WS Paciesas, MH Finger, ML McCollough, M Sahi, B Peterson, et al. The burst and transient source experiment (batse) earth occultation catalog of low-energy gamma-ray sources. *The Astrophysical Journal Supplement Series*, 154(2):585, 2004.

[52] G. Boella, R. C. Butler, G. C. Perola, L. Piro, L. Scarsi, and J. A. M. Bleeker. BeppoSAX, the wide band mission for X-ray astronomy. , 122:299–307, April 1997. doi: 10.1051/aas:1997136.

[53] G. Ricker, Jean-Luc Atteia, Geoffrey Crew, J. Doty, E. Fenimore, M. Galassi, Carlo Graziani, Killian Hurley, J. Jernigan, Noriyasu Kawai, Don Lamb, Masaru Matsuoka, G. Pizzichini, Yuji Shirasaki, T. Tamagawa, Roland Vanderspek, G. Vedrenne, J. Villasenor, S. Woosley, and Atsumasa Yoshida. The high energy transient explorer (hete): Mission and science overview. *AIP Conference Proceedings*, 662:3–16, 04 2003. doi: 10.1063/1.1579291.

[54] M. R. Metzger, S. G. Djorgovski, S. R. Kulkarni, C. C. Steidel, K. L. Adelberger, D. A. Frail, E. Costa, and F. Frontera. Spectral constraints on the redshift of the optical counterpart to the γ-ray burst of 8 May 1997. , 387(6636):878–880, June 1997. doi: 10.1038/43132.

[55] Neil Gehrels, Guido Chincarini, P ea Giommi, KO Mason, JA Nousek, AA Wells, NE White, SD Barthelmy, DN Burrows, LR Cominsky, et al. The swift gamma-ray burst mission. *The Astrophysical Journal*, 611(2):1005, 2004.

[56] WB Atwood, Aous A Abdo, Markus Ackermann, W Althouse, B Anderson, M Axelsson, Luca Baldini, J Ballet, DL Band, Guido Barbiellini, et al. The large area telescope on the fermi gamma-ray space telescope mission. *The Astrophysical Journal*, 697(2):1071, 2009.

[57] Abbott, B. P. et al. Gwtc-1: A gravitational-wave transient catalog of compact binary mergers observed by ligo and virgo during the first and second observing runs. *Phys. Rev. X*, 9:031040, Sep 2019. doi: 10.1103/PhysRevX.9.031040. URL https://link.aps.org/doi/10.1103/PhysRevX.9.031040.

[58] Enwei Liang and Bing Zhang. Identification of Two Categories of Optically Bright Gamma-Ray Bursts. , 638(2):L67–L70, February 2006. doi: 10.1086/501049.

[59] Eleonora Troja, Stephan Rosswog, and Neil Gehrels. Precursors of short gamma-ray bursts. *The Astrophysical Journal*, 723(2):1711, 2010.

[60] D. Band, J. Matteson, L. Ford, B. Schaefer, D. Palmer, B. Teegarden, T. Cline, M. Briggs, W. Paciesas, G. Pendleton, G. Fishman, C. Kouveliotou, C. Meegan, R. Wilson, and P. Lestrade. BATSE Observations of Gamma-Ray Burst Spectra. I. Spectral Diversity. , 413:281, August 1993. doi: 10.1086/172995.

[61] Bin-Bin Zhang, Bing Zhang, En-Wei Liang, Yi-Zhong Fan, Xue-Feng Wu, Asaf Pe'er, Amanda Maxham, He Gao, and Yun-Ming Dong. A Comprehensive Analysis of Fermi Gamma-ray Burst Data. I. Spectral Components and the Possible Physical Origins of LAT/GBM GRBs. , 730(2):141, April 2011. doi: 10.1088/0004-637X/730/2/141.

[62] Pawan Kumar and Bing Zhang. The physics of gamma-ray bursts & relativistic jets. *Physics Reports*, 561:1–109, 2015.

[63] AM Beloborodov and P Mészáros. Photospheric emission of gamma-ray bursts. *Space Science Reviews*, 207(1):87–110, 2017.

[64] Edo Berger. Short-duration gamma-ray bursts. *Annual review of Astronomy and Astrophysics*, 52:43–105, 2014.

[65] Charles D Dermer. Curvature effects in gamma-ray burst colliding shells. *The Astrophysical Journal*, 614(1):284, 2004.

[66] Bin-Bin Zhang, Yi-Zhong Fan, Rong-Feng Shen, Dong Xu, Fu-Wen Zhang, Da-Ming Wei, David N. Burrows, Bing Zhang, and Neil Gehrels. GRB 120422A: A Low-luminosity Gamma-Ray Burst Driven by a Central Engine. , 756(2):190, September 2012. doi: 10.1088/0004-637X/756/2/190.

[67] Hou-Jun Lü, Bing Zhang, Wei-Hua Lei, Ye Li, and Paul D Lasky. The millisecond magnetar central engine in short grbs. *The Astrophysical Journal*, 805(2):89, 2015.

[68] Davide Lazzati and Rosalba Perna. X-ray flares and the duration of engine activity in gamma-ray bursts. *Monthly Notices of the Royal Astronomical Society: Letters*, 375(1): L46–L50, 2007.

[69] Bin-Bin Zhang, Bing Zhang, En-Wei Liang, Yi-Zhong Fan, Xue-Feng Wu, Asaf Pe'er, Amanda Maxham, He Gao, and Yun-Ming Dong. A Comprehensive Analysis of Fermi Gamma-ray Burst Data. I. Spectral Components and the Possible Physical Origins of LAT/GBM GRBs. , 730(2):141, April 2011. doi: 10.1088/0004-637X/730/2/141.

[70] Ivan Zalamea and Andrei M. Beloborodov. Neutrino heating near hyper-accreting black holes. *Monthly Notices of the Royal Astronomical Society*, 410(4):2302–2308, 01 2011. ISSN 0035-8711. doi: 10.1111/j.1365-2966.2010.17600.x. URL https://doi.org/10.1111/j.1365-2966.2010.17600.x.

[71] O. Just, M. Obergaulinger, H.-T. Janka, A. Bauswein, and N. Schwarz. NEUTRON-STAR MERGER EJECTA AS OBSTACLES TO NEUTRINO-POWERED JETS OF GAMMA-RAY BURSTS. *The Astrophysical Journal*, 816(2):L30, jan 2016. doi: 10.3847/2041-8205/816/2/l30. URL https://doi.org/10.3847/2041-8205/816/2/l30.

[72] R. D. Blandford and R. L. Znajek. Electromagnetic extraction of energy from Kerr black holes. *Monthly Notices of the Royal Astronomical Society*, 179(3):433–456, 07 1977. ISSN 0035-8711. doi: 10.1093/mnras/179.3.433. URL https://doi.org/10.1093/mnras/179.3.433.

[73] Alexander Tchekhovskoy, Ramesh Narayan, and Jonathan C McKinney. Efficient generation of jets from magnetically arrested accretion on a rapidly spinning black hole. *Monthly Notices of the Royal Astronomical Society: Letters*, 418(1):L79–L83, 2011.

[74] Milton Ruiz, Ryan N Lang, Vasileios Paschalidis, and Stuart L Shapiro. Binary neutron star mergers: a jet engine for short gamma-ray bursts. *The Astrophysical Journal Letters*, 824(1):L6, 2016.

[75] Luciano Rezzolla, Bruno Giacomazzo, Luca Baiotti, Jonathan Granot, Chryssa Kouveliotou, and Miguel A Aloy. The missing link: merging neutron stars naturally produce jet-like structures and can power short gamma-ray bursts. *The Astrophysical Journal Letters*, 732(1):L6, 2011.

[76] Christopher Thompson and Robert Duncan. The soft gamma repeaters as very strongly magnetized neutron stars. ii. quiescent neutrino, x-ray, and alfvén wave emission. *The Astrophysical Journal*, 473:322, 01 2009. doi: 10.1086/178147.

[77] SL Shapiro and SA Teukolsky. *Black Holes, White Dwarfs, and Neutron Stars: The Physics of Compact Objects*. Jonn Wiley and Sons, New York, 1983.

[78] Riccardo Ciolfi and Daniel M Siegel. Short gamma-ray bursts in the "time-reversal" scenario. *The Astrophysical Journal Letters*, 798(2):L36, 2014.

[79] OS Salafia, C Barbieri, S Ascenzi, and M Toffano. Gamma-ray burst jet propagation, development of angular structure, and the luminosity function. *Astronomy & Astrophysics*, 636:A105, 2020.

[80] Davide Lazzati, Rosalba Perna, Brian J Morsony, Diego Lopez-Camara, Matteo Cantiello, Riccardo Ciolfi, Bruno Giacomazzo, and Jared C Workman. Late time afterglow observations reveal a collimated relativistic jet in the ejecta of the binary neutron star merger gw170817. *Physical Review Letters*, 120(24):241103, 2018.

[81] Davide Lazzati. Short duration gamma-ray bursts and their outflows in light of gw170817. *Frontiers in Astronomy and Space Sciences*, 7, 2020. ISSN 2296-987X. doi: 10.3389/fspas.2020.578849. URL https://www.frontiersin.org/article/10.3389/fspas.2020.578849.

[82] Andrea Pavan, Riccardo Ciolfi, Jay V Kalinani, and Andrea Mignone. Short gamma-ray burst jet propagation in binary neutron star merger environments. *Monthly Notices of the Royal Astronomical Society*, 506(3):3483–3498, 2021.

[83] Xiaoyi Xie, Jonathan Zrake, and Andrew MacFadyen. Numerical simulations of the jet dynamics and synchrotron radiation of binary neutron star merger event GW170817/GRB 170817a. *The Astrophysical Journal*, 863(1):58, aug 2018. doi: 10.3847/1538-4357/aacf9c. URL https://doi.org/10.3847/1538-4357/aacf9c.

[84] Adithan Kathirgamaraju, Alexander Tchekhovskoy, Dimitrios Giannios, and Rodolfo Barniol Duran. EM counterparts of structured jets from 3D GRMHD simulations. , 484 (1):L98–L103, March 2019. doi: 10.1093/mnrasl/slz012.

[85] Jin-Jun Geng, Bing Zhang, Anders Kölligan, Rolf Kuiper, and Yong-Feng Huang. Propagation of a short GRB jet in the ejecta: Jet launching delay time, jet structure, and GW170817/GRB 170817a. *The Astrophysical Journal*, 877(2):L40, jun 2019. doi: 10.3847/2041-8213/ab224b. URL https://doi.org/10.3847/2041-8213/ab224b.

[86] W. Fong, E. Berger, R. Margutti, and B. A. Zauderer. A DECADE OF SHORT-DURATION GAMMA-RAY BURST BROADBAND AFTERGLOWS: ENERGETICS, CIRCUMBURST DENSITIES, AND JET OPENING ANGLES. *The Astrophysical Journal*, 815(2):102, dec 2015. doi: 10.1088/0004-637x/815/2/102. URL https://doi.org/10.1088/0004-637x/815/2/102.

[87] G. Ghirlanda, O. S. Salafia, Z. Paragi, M. Giroletti, J. Yang, B. Marcote, J. Blanchard, I. Agudo, T. An, M. G. Bernardini, R. Beswick, M. Branchesi, S. Campana, C. Casadio, E. Chassande-Mottin, M. Colpi, S. Covino, P. D'Avanzo, V. D'Elia, S. Frey, M. Gawronski, G. Ghisellini, L. I. Gurvits, P. G. Jonker, H. J. van Langevelde, A. Melandri, J. Moldon, L. Nava, A. Perego, M. A. Perez-Torres, C. Reynolds, R. Salvaterra, G. Tagliaferri, T. Venturi, S. D. Vergani, and M. Zhang. Compact radio emission indicates a structured jet was produced by a binary neutron star merger. *Science*, 363(6430):968–971, March 2019. doi: 10.1126/science.aau8815.

[88] Davide Lazzati and Mitchell C. Begelman. Universal GRB Jets from Jet-Cocoon Interaction in Massive Stars. , 629(2):903–907, August 2005. doi: 10.1086/430877.

[89] Abbott, B. P. et al. Gw170817: Observation of gravitational waves from a binary neutron star inspiral. *Phys. Rev. Lett.*, 119:161101, Oct 2017. doi: 10.1103/PhysRevLett.119.161101. URL https://link.aps.org/doi/10.1103/PhysRevLett.119.161101.

[90] Benjamin P Abbott, S Bloemen, P Canizares, H Falcke, RP Fender, S Ghosh, P Groot, T Hinderer, JR Hörandel, PG Jonker, et al. Multi-messenger observations of a binary neutron star merger. 2017.

[91] A. Goldstein, P. Veres, E. Burns, M. S. Briggs, R. Hamburg, D. Kocevski, C. A. Wilson-Hodge, R. D. Preece, S. Poolakkil, O. J. Roberts, C. M. Hui, V. Connaughton, J. Racusin, A. von Kienlin, T. Dal Canton, N. Christensen, T. Littenberg, K. Siellez, L. Blackburn, J. Broida, E. Bissaldi, W. H. Cleveland, M. H. Gibby, M. M. Giles, R. M. Kippen, S. McBreen, J. McEnery, C. A. Meegan, W. S. Paciesas, and M. Stanbro. An ordinary short gamma-ray burst with extraordinary implications: ifermi/i -GBM detection of GRB 170817a. *The Astrophysical Journal*, 848(2):L14, oct 2017. doi: 10.3847/2041-8213/aa8f41. URL https://doi.org/10.3847/2041-8213/aa8f41.

[92] Ore Gottlieb, Ehud Nakar, Tsvi Piran, and Kenta Hotokezaka. A cocoon shock breakout as the origin of the -ray emission in GW170817. *Monthly Notices of the Royal Astronomical Society*, 479(1):588–600, 05 2018. ISSN 0035-8711. doi: 10.1093/mnras/sty1462. URL https://doi.org/10.1093/mnras/sty1462.

[93] Elenora Troja, LUIGI Piro, H Van Eerten, RT Wollaeger, M Im, OD Fox, NR Butler, SB Cenko, T Sakamoto, CL Fryer, et al. The x-ray counterpart to the gravitational-wave event gw170817. *Nature*, 551(7678):71–74, 2017.

[94] Paolo D'Avanzo, Sergio Campana, Om Sharan Salafia, Giancarlo Ghirlanda, Gabriele Ghisellini, Andrea Melandri, Maria Grazia Bernardini, M Branchesi, E Chassande-Mottin, Stefano Covino, et al. The evolution of the x-ray afterglow emission of gw 170817/grb 170817a in xmm-newton observations. *Astronomy & Astrophysics*, 613:L1, 2018.

[95] KD Alexander, E Berger, W Fong, PKG Williams, C Guidorzi, R Margutti, BD Metzger, J Annis, PK Blanchard, D Brout, et al. The electromagnetic counterpart of the binary neutron star merger ligo/virgo gw170817. vi. radio constraints on a relativistic jet and predictions for late-time emission from the kilonova ejecta. *The Astrophysical Journal Letters*, 848(2):L21, 2017.

[96] KP Mooley, AT Deller, O Gottlieb, E Nakar, G Hallinan, S Bourke, DA Frail, A Horesh, A Corsi, and K Hotokezaka. Superluminal motion of a relativistic jet in the neutron-star merger gw170817. *Nature*, 561(7723):355–359, 2018.

[97] Om S Salafia, Gabriele Ghisellini, Giancarlo Ghirlanda, and Monica Colpi. Interpreting grb170817a as a giant flare from a jet-less double neutron star merger. *Astronomy & Astrophysics*, 619:A18, 2018.

[98] Iair Arcavi, Griffin Hosseinzadeh, D Andrew Howell, Curtis McCully, Dovi Poznanski, Daniel Kasen, Jennifer Barnes, Michael Zaltzman, Sergiy Vasylyev, Dan Maoz, et al. Optical emission from a kilonova following a gravitational-wave-detected neutron-star merger. *Nature*, 551(7678):64–66, 2017.

[99] Stefano Valenti, J David, Sheng Yang, Enrico Cappellaro, Leonardo Tartaglia, Alessandra Corsi, Saurabh W Jha, Daniel E Reichart, Joshua Haislip, and Vladimir Kouprianov. The discovery of the electromagnetic counterpart of gw170817: kilonova at 2017gfo/dlt17ck. *The Astrophysical Journal Letters*, 848(2):L24, 2017.

[100] Houri Ziaeepour. Binary neutron star (bns) merger: What we learned from relativistic ejecta of gw/grb 170817a. *Physics*, 1(2):194–228, 2019.

[101] M. M. Kasliwal and E. Nakar and L. P. Singer et al. Illuminating gravitational waves: A concordant picture of photons from a neutron star merger. *Science*, 358(6370):1559–1565, 2017. doi: 10.1126/science.aap9455. URL https://www.science.org/doi/abs/10.1126/science.aap9455.

[102] Ehud Nakar, Ore Gottlieb, Tsvi Piran, Mansi. M. Kasliwal, and Gregg Hallinan. From i/i to radio: The electromagnetic counterpart of GW170817. *The Astrophysical Journal*, 867(1):18, oct 2018. doi: 10.3847/1538-4357/aae205. URL https://doi.org/10.3847/1538-4357/aae205.

[103] D. Mihalas and B. W. Mihalas. *Foundations of radiation hydrodynamics*. 1984.

[104] Carlo Cercignani and Gilberto Medeiros Kremer. *Relativistic Boltzmann Equation*, pages 31–63. Birkhäuser Basel, Basel, 2002. ISBN 978-3-0348-8165-4. doi: 10.1007/978-3-0348-8165-4_2. URL https://doi.org/10.1007/978-3-0348-8165-4_2.

[105] A. M. Anile. *Relativistic Fluids and Magneto-fluids*. 2005.

[106] Oscar A. Reula. Hyperbolic methods for einstein's equations. *Living Reviews in Relativity [electronic only]*, 1:Article No. 1998–3, 1998. URL http://eudml.org/doc/223442.

[107] Lev Davidovich Landau and E. M. Lifshitz. *Fluid mechanics*. 1959.

[108] Julio David Melon Fuksman and Andrea Mignone. A radiative transfer module for relativistic magnetohydrodynamics in the pluto code. *The Astrophysical Journal Supplement Series*, 242(2):20, 2019.

[109] Gerald C. Pomraning. *The equations of radiation hydrodynamics / by G. C. Pomraning.* Oxford : Pergamon press, 1973. ISBN 0080168930.

[110] Gabriele Ghisellini. *Radiative processes in high energy astrophysics*, volume 873. Springer, 2013.

[111] Jonathan C. McKinney, Alexander Tchekhovskoy, Aleksander Sadowski, and Ramesh Narayan. Three-dimensional general relativistic radiation magnetohydrodynamical simulation of super-Eddington accretion, using a new code harmrad with M1 closure. *Monthly Notices of the Royal Astronomical Society*, 441(4):3177–3208, 05 2014. ISSN 0035-8711. doi: 10.1093/mnras/stu762. URL https://doi.org/10.1093/mnras/stu762.

[112] C.D. Levermore. Relating eddington factors to flux limiters. *Journal of Quantitative Spectroscopy and Radiative Transfer*, 31(2):149–160, 1984. ISSN 0022-4073. doi: https://doi.org/10.1016/0022-4073(84)90112-2. URL https://www.sciencedirect.com/science/article/pii/0022407384901122.

[113] J. J. Monaghan and J. C. Lattanzio. A refined particle method for astrophysical problems. , 149(1):135–143, August 1985.

[114] R.J. LeVeque. *Numerical Methods for Conservation Laws*. Birkhäuser Basel, 1990. doi: https://doi.org/10.1007/978-3-0348-5116-9.

[115] SAEG Falle. Rarefaction shocks, shock errors and low order of accuracy in zeus. *arXiv preprint astro-ph/0207419*, 2002.

[116] Sergei Godunov and I Bohachevsky. Finite difference method for numerical computation of discontinuous solutions of the equations of fluid dynamics. *Matematičeskij sbornik*, 47 (3):271–306, 1959.

[117] Andrea Mignone, G Bodo, S Massaglia, Titos Matsakos, O ea Tesileanu, C Zanni, and Anthony Ferrari. Pluto: a numerical code for computational astrophysics. *The Astrophysical Journal Supplement Series*, 170(1):228, 2007.

[118] E. F. Toro, M. Spruce, and W. Speares. Restoration of the contact surface in the HLL-Riemann solver. *Shock Waves*, 4(1):25–34, July 1994. doi: 10.1007/BF01414629.

[119] A Mignone and G Bodo. An hllc riemann solver for relativistic flows—i. hydrodynamics. *Monthly Notices of the Royal Astronomical Society*, 364(1):126–136, 2005.

[120] Sigal Gottlieb and Chi-Wang Shu. Total variation diminishing runge-kutta schemes. *Mathematics of Computation*, 67, 08 1996. doi: 10.1090/S0025-5718-98-00913-2.

[121] Lorenzo Pareschi and Giovanni Russo. Implicit-explicit runge-kutta schemes and applications to hyperbolic systems with relaxation. *arXiv preprint arXiv:1009.2757*, 2010.

[122] Carlos Palenzuela, Luis Lehner, Oscar Reula, and Luciano Rezzolla. Beyond ideal mhd: towards a more realistic modelling of relativistic astrophysical plasmas. *Monthly Notices of the Royal Astronomical Society*, 394(4):1727–1740, 2009.

[123] Aleksander Sądowski, Ramesh Narayan, Alexander Tchekhovskoy, and Yucong Zhu. Semi-implicit scheme for treating radiation under M1 closure in general relativistic conservative fluid dynamics codes. *Monthly Notices of the Royal Astronomical Society*, 429(4):3533–3550, 01 2013. ISSN 0035-8711. doi: 10.1093/mnras/sts632. URL https://doi.org/10.1093/mnras/sts632.

[124] Jonathan C. McKinney, Alexander Tchekhovskoy, Aleksander Sadowski, and Ramesh Narayan. Three-dimensional general relativistic radiation magnetohydrodynamical simulation of super-Eddington accretion, using a new code harmrad with M1 closure. *Monthly Notices of the Royal Astronomical Society*, 441(4):3177–3208, 05 2014. ISSN 0035-8711. doi: 10.1093/mnras/stu762. URL https://doi.org/10.1093/mnras/stu762.

[125] A. Mignone and Jonathan C. McKinney. Equation of state in relativistic magnetohydrodynamics: variable versus constant adiabatic index. *Monthly Notices of the Royal Astronomical Society*, 378(3):1118–1130, 06 2007. ISSN 0035-8711. doi: 10.1111/j.1365-2966.2007.11849.x. URL https://doi.org/10.1111/j.1365-2966.2007.11849.x.

[126] A. Mignone, T. Plewa, and G. Bodo. The Piecewise Parabolic Method for Multidimensional Relativistic Fluid Dynamics. , 160(1):199–219, September 2005. doi: 10.1086/430905.

[127] A. H. Taub. Relativistic rankine-hugoniot equations. *Physical Review*, 74:328–334, 1948.

[128] Dirk Martin, Albino Perego, Almudena Arcones, F-K Thielemann, Oleg Korobkin, and Stephan Rosswog. Neutrino-driven winds in the aftermath of a neutron star merger: nucleosynthesis and electromagnetic transients. *The Astrophysical Journal*, 813(1):2, 2015.

[129] A. S. Householder. *The numerical treatment of a single nonlinear equation*. McGraw-Hill, 1970.

[130] Federico Cipolletta, Jay Vijay Kalinani, Bruno Giacomazzo, and Riccardo Ciolfi. Spritz: a new fully general-relativistic magnetohydrodynamic code. *Classical and Quantum Gravity*, 37(13):135010, 2020.

[131] Jay V. Kalinani, Riccardo Ciolfi, Wolfgang Kastaun, Bruno Giacomazzo, Federico Cipolletta, and Lorenzo Ennoggi. Implementing a new recovery scheme for primitive variables in the general relativistic magnetohydrodynamic code spritz. *Phys. Rev. D*, 105:103031, May 2022. doi: 10.1103/PhysRevD.105.103031. URL https://link.aps.org/doi/10.1103/PhysRevD.105.103031.

[132] Federico Cipolletta, Jay Vijay Kalinani, Edoardo Giangrandi, Bruno Giacomazzo, Riccardo Ciolfi, Lorenzo Sala, and Beatrice Giudici. Spritz: general relativistic magnetohydrodynamics with neutrinos. *Classical and Quantum Gravity*, 38(8):085021, 2021.

[133] A Mignone, Gianluigi Bodo, B Vaidya, and G Mattia. A particle module for the pluto code. i. an implementation of the mhd–pic equations. *The Astrophysical Journal*, 859(1):13, 2018.